Micrometeoroid, Orbital Debris, and Shielding Analysis for the Soft X-ray Camera (SXC) of the High Energy Transient Explorer (HETE-2) Spacecraft

by

Sangwoo Pak

B.S. Physics, Math, Integrated Science Program
Northwestern University, 1997

Submitted to the Department of Aeronautics and Astronautics in Partial
Fulfillment of the Requirements for the Degree of

MASTER OF SCIENCE IN AERONAUTICS AND ASTRONAUTICS
AT THE
MASSACHUSETTS INSTITUTE OF TECHNOLOGY

JUNE 1999

Signature of Author: ______________________________
Department of Aeronautics and Astronautics
May 18, 1999

Certified by: ______________________________
Manuel Martinez-Sanchez
Professor of Aeronautics and Astronautics
Thesis Supervisor

Certified by: ______________________________
George Ricker
Senior Research Scientist
Research Supervisor

Accepted by: ______________________________
Jaime Peraire
Professor of Aeronautics and Astronautics
Chairman, Committee for Graduate Students

Micrometeoroid, Orbital Debris, and Shielding Analysis for the Soft X-ray Camera (SXC) of the High Energy Transient Explorer (HETE-2) Spacecraft

by

Sangwoo Pak

Submitted to the Department of Aeronautics and Astronautics
on May 7, 1999 in Partial Fulfillment of the
Requirements for the Degree of Master of Science in
Aeronautics and Astronautics

ABSTRACT

The High Energy Transient Explorer (HETE-2) is a scientific spacecraft that will carry out a multi-wavelength study to determine the origin and nature of cosmic gamma-ray bursts (GRBs). The Soft X-ray Camera (SXC) is the new science instrument on board the HETE-2 spacecraft and uses a pair of Charge Coupled Devices (CCDs) to detect incoming X-ray in the 0.5-14 keV energy range.

Once in Earth orbit, HETE-2 will encounter micrometeoroids and orbital debris. Micrometeoroids are the smallest natural particles in space and orbital debris are any inoperative, manmade objects remaining in Earth orbit. The major concern for CCDs in the SXC is that they are exposed to the micrometeoroids and orbital debris environment. A single impact from these particles may cause the entire failure of the CCD due to an electrical short.

The Optical Blocking Filter (OBF) and the Beryllium (Be) shield are two shielding structures that will protect CCDs against particle impacts. The Optical Blocking Filter (OBF) can act as a Whipple shield, which vaporizes or fragments impacting particles. The Be shield is added on the top of only one CCD for additional protection to ensure that at least one CCD is operational.

In this thesis, I analyze the micrometeoroids and orbital debris flux environment in order to estimate the number of particles that CCDs will encounter. Then, I calculate the size of particles that cause impact craters which are deep enough to cause a failure of the CCD. In the shielding chapter of this thesis, I discuss how each shield works and analyze its effectiveness in decreasing the significant impact rate on the CCDs. Although HETE-2 will be launched after the November 1999 Leonid meteoroid storm, I analyze the hypothetical impact of such a storm on the SXC.

Thesis Supervisor: Manuel Martinez-Sanchez
Title: Professor of Aeronautics and Astronautics

Acknowledgment

I would like to thank following people who helped me to get this far,

- Dr. George Ricker for giving me the opportunity to participate in HETE-2 project and assigning me to work on very interesting area of space mission.
- Prof. Manuel Martinez-Sanchez for being my thesis supervisor and giving me a guidance for writing my thesis.
- Dr. Joel Villasenor for being my advisor who helped me so much for my research and participation in HETE-2 project.
- All other members of HETE-2 team.
- My mother, sister, and Esther.

Table of Contents

Chapter 1

INTRODUCTION

1.1 Micrometeoroids and Orbital Debris Hazard

A spacecraft will encounter meteoroids and orbital debris once it is orbiting the Earth. The meteoroids refer to the particles of natural origin that are present in interplanetary space. The smallest meteoroids are called *micrometeoroids,* defined as particles smaller in mass than 10^{-6} g [Fechtig et al., 1979]. The potential hazards from micrometeoroid impacts have historically been a design consideration for spacecraft. The scientific community has also recognized the fact that man's space activities over the past 35 years have dramatically altered the near earth environment. The term *orbital debris* refers to any inoperative manmade object remaining in Earth orbit. Unlike the population of micrometeoroids which stays nearly constant, the population of orbital debris increases every year due to additional launches and breakup of existing satellites. As a result, the orbital debris environment has now become more hazardous than the micrometeoroid environment. Since both micrometeoroid and orbital debris have very high velocities, the obvious concern for spacecraft is mechanical damage caused by hypersonic impacts. For example, NASA routinely replaces space shuttle windows because of damage from small particle impacts. Recent space shuttle flights use evasive maneuvers to avoid larger particles. Catastrophic collision with large objects is a much smaller concern than a long term material degradation from repeated small impacts and damage of critical elements vulnerable to a single impact.

The High Energy Transient Explorer (HETE-2) is a scientific spacecraft for gamma ray burst (GRB) research, carrying a pair of Soft X-ray Cameras (SXC) as part of the science instruments on board. The SXC uses a pair of Charge Coupled Devices (CCD) to detect incoming X-rays. The HETE-2 science team realized in 1997 that if there is a micrometeoroid or orbital debris impact deep enough to cause electrical shorts on a CCD, the entire device could be subject to a failure. Therefore, the purpose of this thesis is to quantify the micrometeoroid and orbital debris hazard for the HETE-2 SXC and to analyze the proposed shielding mechanism, including its effectiveness against micrometeoroid and orbital debris impacts.

1.2 The High Energy Transient Explorer (HETE-2)

The High Energy Transient Explorer (HETE-2) is a scientific spacecraft that will carry out a multi-wavelength study to determine the origin and nature of cosmic gamma-ray bursts (GRBs). The previous attempt at this mission, the High Energy Transient Explorer (HETE), was lost during the launch on November 4, 1996 due to a failure of the Pegasus XL rocket. Although the Pegasus XL rocket which carried the HETE and another spacecraft, SAC-B, reached its planned low earth orbit, the third stage of the rocket failed to release the satellite. As a result, HETE was trapped and expired inside the can supporting SAC-B [Ricker, 1997]. Now using the previous experience and knowledge gained from building the first HETE, the HETE-2 satellite is being rebuilt at Massachusetts Institute of Technology (MIT) Center for Space Research (CSR). The HETE-2 is scheduled to be launched on January 23, 2000 using a so-called Pegasus hybrid rocket. The HETE-2 will fly in a low earth orbit at 0° inclination and 600 km altitude. The HETE-2 weighs about 280 lbs. and is small enough to fit within a cylinder with 89 cm x 66 cm diameter. The following figure shows the basic shape of the HETE-2.

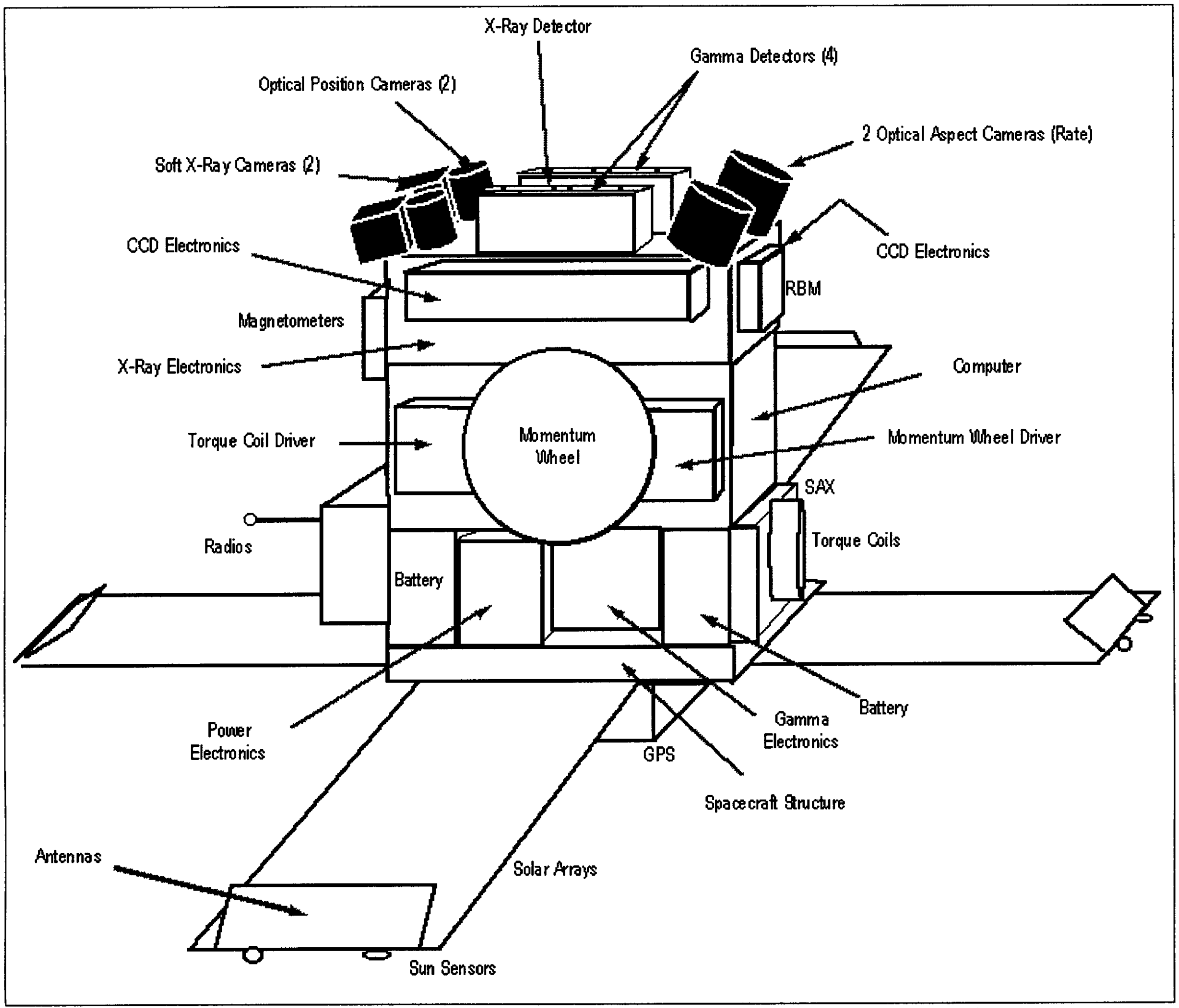

Figure 1-1. The HETE-2 Spacecraft. (Drawing courtesy of HETE-2 Team)

The objectives of the HETE-2 mission include the simultaneous multi-wavelength band observation of energetic, transient astrophysical sources in the soft X-ray, medium X-ray, and gamma-ray energy ranges; and the precise localization and identification of cosmic gamma-ray burst sources using science instruments mounted on the spacecraft. These objectives are summarized in Program-Level Requirements Documents [Ricker, 1999].

1. Identify the occurrence of a GRB.
2. Approximately locate the GRB (~10 arcmin. accuracy) utilizing its medium energy X-ray emission.

3. Precisely locate the GRB (~10 arcsec. accuracy) utilizing its soft X-ray emission.
4. Rapidly transmit (~10 second delay) the location and intensity data directly to ground-based optical, IR, and radio observers.

The unique feature of HETE-2 mission is its capability to localize GRBs with several arcsecond accuracy. The collected data is transmitted to the ground, picked up by a global network of primary and secondary ground stations, and distributed to ground-based observers who will be able to focus their telescopes onto the GRB while it is in outburst. As a result, the HETE-2 mission may solve the mystery of GRBs.

Three kinds of science instruments are mounted on board of HETE-2 spacecraft. They are the French Gamma-ray Telescopes (FREGATE), the Wide-field X-ray Monitor (WXM), and the Soft X-ray Camera (SXC). Their relative locations are shown in the following figure.

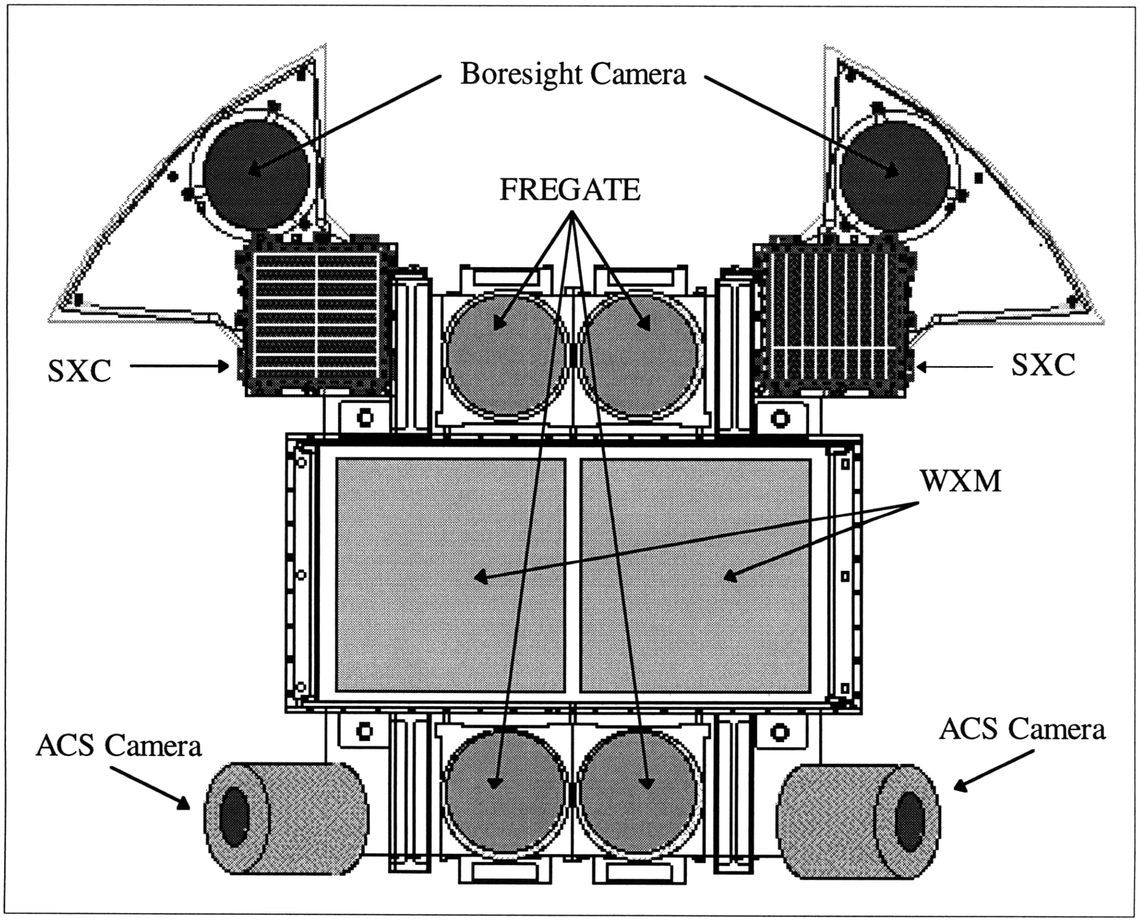

Figure 1-2. Top View of HETE-2 Science Instruments. (Drawing courtesy of HETE-2 Team)

All these science instruments shown in the above diagram will be always pointed anti-sunward. The FREGATE is a set of omnidirectional gamma-ray spectrometers provided by CESR in France. The FREGATE will detect photons in the 6-1000 keV energy range, providing accurate burst triggers and moderate resolution spectra. The purpose of WXM is to gather information about incoming X-ray in the 2-25 keV energy range and it is provided by RIKEN in Japan [Ricker, 1999]. The SXCs are the new science instruments that were not a part of the original HETE mission and will be placed in the location previously occupied by the UV cameras in the original HETE. The SXCs, designed and built at the MIT CSR, will detect photons in the 0.5-14 keV energy range.

1.3 The Soft X-ray Camera (SXC)

In 1997, the Beppo-Sax mission established that a GRB localized precisely by means of X-ray radiation can lead to identification of optical counterparts by ground based observations. GRB spectra showed that many GRBs have a substantial X-ray flux below 5 keV. These two findings led to calculations that a pair of SXCs, each consisting of a large-area Charge Coupled Device (CCD) behind a coded aperture, could be used to improve the localization of a large fraction of the GRBs that HETE-2 will detect. At the same time, the role of the UV camera that was part of the original HETE-2 mission diminished because the predicted UV flux was very small compared to the on-board detection capability of HETE-2. The SXC will rapidly process the signal from a suspected GRB and send its localization data to ground based observers, so that optical and radio observations can be made while the GRB is still happening [Vanderspek and Villasenor, 1997].

The SXC is composed of the mask and its supporting frame, the body walls, the Optical Blocking Filter, the Beryllium shield, and the focal plane CCDs. The SXC is roughly cubic in shape with dimensions of 10 cm x 10 cm x 10 cm. The geometry of the SXC box provides the CCD with the field of view of greater than 1 steradian. The SXC is shown in the following picture.

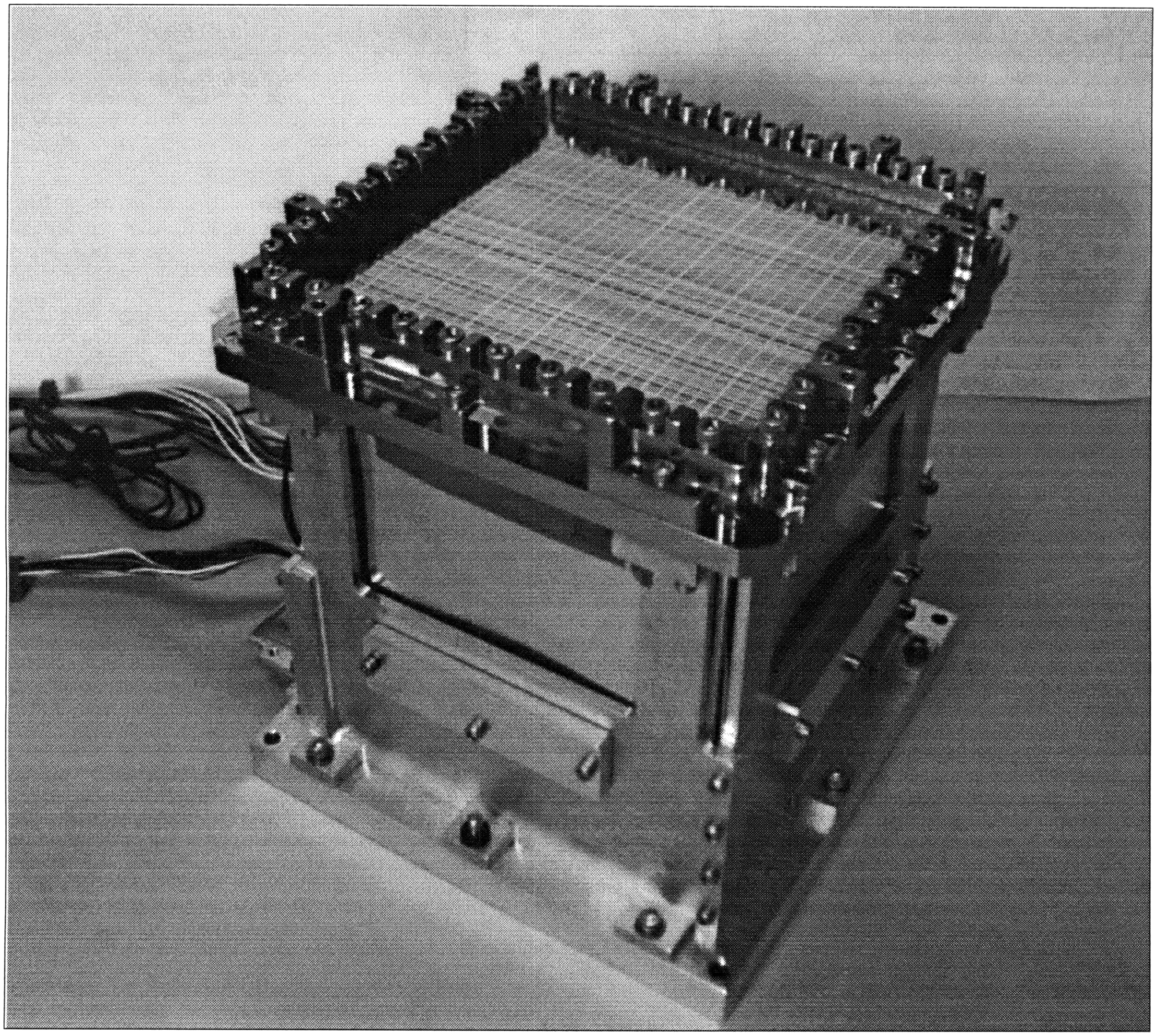

Figure 1-3. The Soft X-Ray Camera (SXC)

Shadows cast from a coded aperture on CCDs determine the angle of incidence of the incoming X-rays and hence their direction. A finely spaced mask and the small pixel size of the CCDs lead to arcsecond resolution. The main elements of the SXC are the mask and the CCD, but the housing structure supporting and surrounding these are crucial to the performance of the instrument. The separation between the mask and the CCD is 9.5 cm. The coded mask consists of a thin, 10 cm x 10 cm, sheet of electroformed gold. The thickness of the mask is about 33 μm. It has a series of slits of varying width, which constitute the coded aperture. The width of the smallest slit is 45 μm. The slit pattern is pseudo-random and the mask open fraction due to these slits is 20%. The following picture shows the top view of the coded mask.

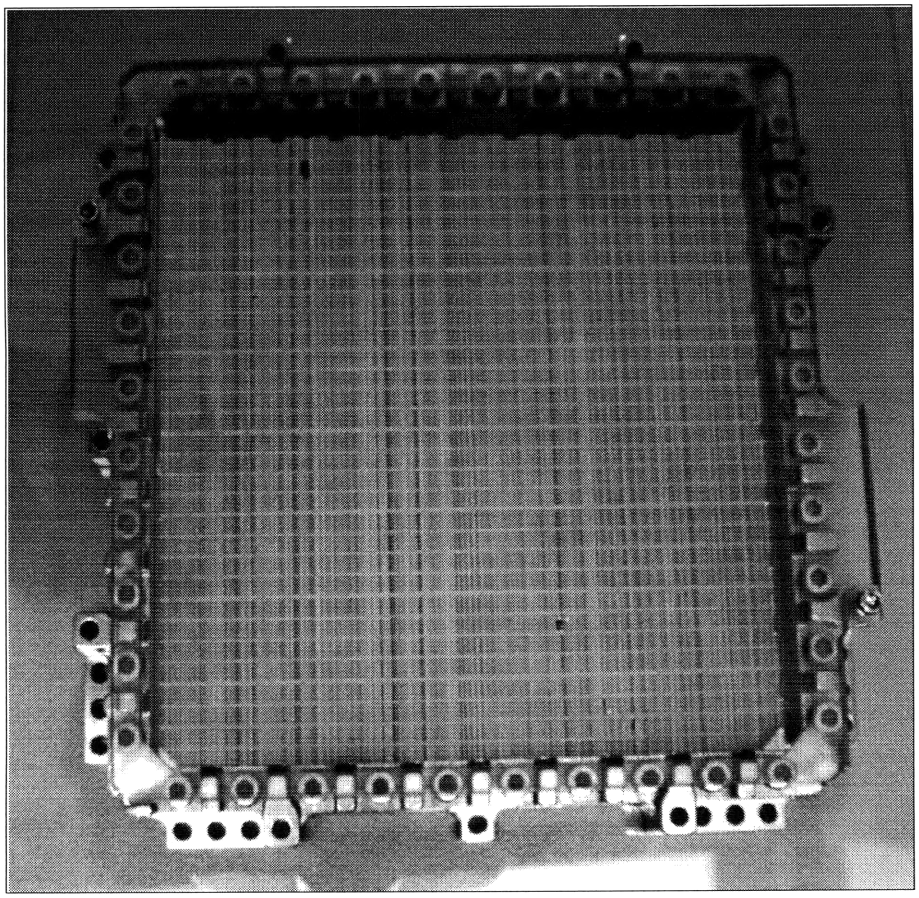

Figure 1-4. Top View of the Mask

The above picture shows the Mask with a series of slits of varying width. Although these open slits are covered by a thin layer of Optical Blocking Filter (OBF), the hypervelocity micrometeoroid and orbital debris may puncture the OBF and travel downward to cause damage to the CCD.

The OBF is a thin membrane, consisting of 0.5 μm thick polyimide and 0.15 μm thick aluminum. The original purpose of this membrane was to block the light from entering inside the SXC. This membrane can also act as a 'Whipple shield' [Christiansen, 1993] against micrometeoroid and orbital debris impacts. This concept of Whipple shield and its effectiveness against particle impacts are discussed in detail in later sections of this thesis.

1.4 The Charge Coupled Device (CCD)

The Charge Coupled Device (CCD) that will be used for SXC is the CCID-20 manufactured by MIT Lincoln Laboratory. The CCID-20 has an array of 2048 x 4096 pixels. One pixel size is 15 μm x 15 μm, and the dimension of one CCID-20 is 3.1 cm x 6.1 cm. Each SXC uses two CCID-20s, giving a geometric area of 37.82 cm^2. The top view of the two CCID-20s is shown in Figure 1-5 and the cross section view of one pixel is shown in Figure 1-6.

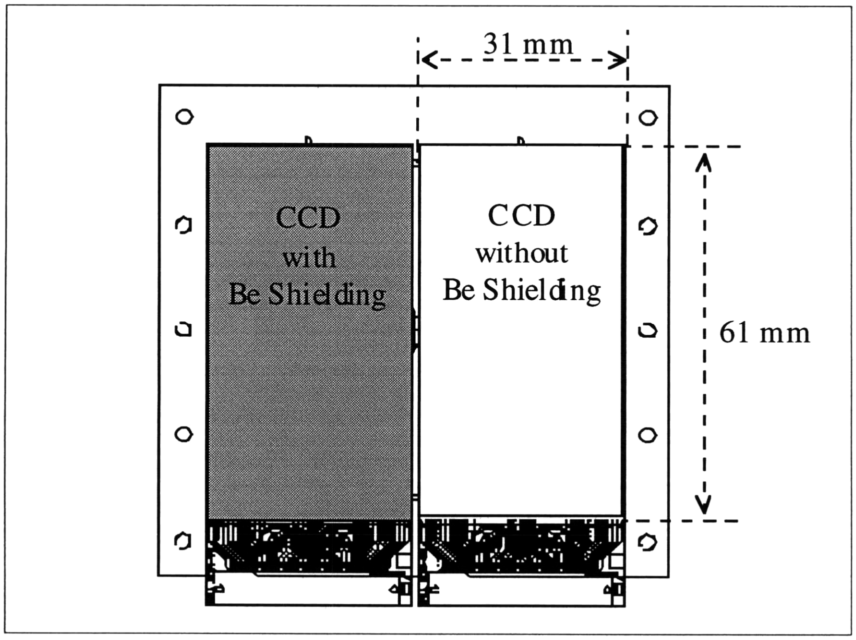

Figure 1-5. Dimensions of the CCID-20. (Drawing courtesy of Villasenor)

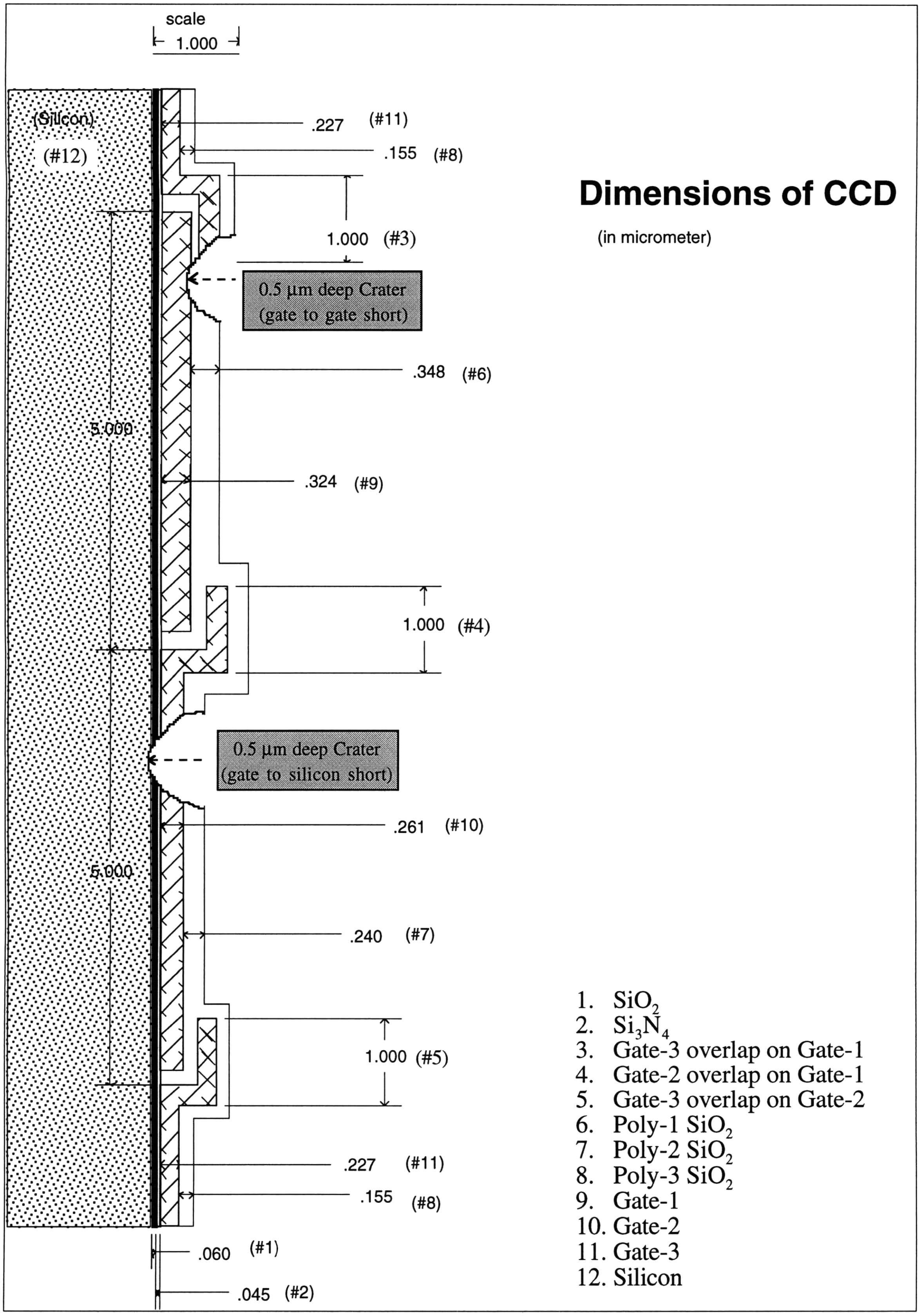

Figure 1-6. Cross Section of one CCD Pixel [Prigozhin, G].

As shown in Figure 1-5, a Beryllium (Be) shield is added on the top of only one CCD. Later sections will explain the reason for having only one Be shield and its effectiveness in protecting the CCD. In Figure 1-6, three gates each with a width of 5 μm constitute one pixel of CCD. When an incoming X-ray photon hits the CCD, the energy is converted into electrons in the potential well that is generated underneath the gate. These electrons are collected and yield information about the position and the magnitude of the incoming X-ray. If there is a gate to gate short or a gate to silicon short as shown in Figure 1-6, then there will be a pixel failure, or possibly a failure of the entire CCD. Since all pixels are interconnected, when a phase of one pixel fails, then all the phases of the other pixels will not hold a voltage needed to transfer charge from any part of the CCD to the collection amplifier. Therefore, it is concluded that a crater of about 0.5 micron depth caused by micrometeoroid or orbital debris impact could result in a failure of the CCD.

Chapter 2

METEOROIDS

2.1 Background

In this section, definitions are provided first. A *meteoroid* is a natural object in space before it enters the Earth's atmosphere. A *meteor* is the flash of light one sees in the sky when a meteoroid enters the atmosphere at high speed and burns up. A *meteorite* is any piece of a meteor which survives the trip through the atmosphere and hits the ground. The smallest meteoroid is called a *micrometeoroid*, which is a particle smaller than about 10^{-6} g. Most of meteoroids originate from comets or asteroids [Fechtig et al., 1979]. A comet is a solid body composed primarily of a combination of ice and cosmic dust. They are thought to have formed very far out in the solar nebula early in the formation of the solar system. There are those with close-in orbits, the Kuiper objects which orbit out near Uranus, and the Oort Cloud objects, which orbit at very large distances out from the Sun. Occasionally, these orbits are perturbed which cause the comets to come into the inner solar system. Asteroids are pieces of rock, iron, and dust which are thought to be the remnants of the early solar system formation. Most asteroids are inner solar system objects that orbit the Sun between the orbits of Mars and Jupiter. The orbits are occasionally perturbed by Jupiter or asteroid-asteroid collisions which cause them to cross the Earth's orbit. Asteroids are the primary source of the sporadic meteors, and certainly the major source of meteorites. Some meteoroids appear to come from impacts of asteroids on Mars and the Moon [Ailor et al., 1998]. Meteoroids that retain their parent body orbit and create periods of high flux are called streams. Random fluxes with no apparent pattern are called sporadic. The average total meteoroid environment present is comprised of the average sporadic meteoroids and a yearly average of stream meteoroids.

2.2 Meteoroid Velocity

Because of the precession of a satellite's orbit and the tilt of the Earth's equatorial plane with respect to the ecliptic plane, the meteoroid environment can be assumed to be isotropic relative to Earth for design applications. The encounter velocities range from 11.1 km/sec to about 72.2 km/sec at an altitude of 600 km. In interplanetary space, velocities range down to zero, and the average is about 12-13 km/sec [Hodgson and Cupples, 1992]. The higher velocity near earth is due to the gravity of Earth providing kinetic energy to the particles. Anderson et al. provide the velocity distribution with respect to Earth in low earth orbit. The velocity distribution, *n(v),* is given by the following equations [Anderson and Smith, 1994].

$$\begin{aligned} n(v) &= 0.112 && \text{for } 11.1 \le v < 16.3\ km/s, \\ n(v) &= 3.328 \times 10^{5}\ v^{-5\ 34} && 16.3 \le v < 55\ km/s, \\ n(v) &= 1.695 \times 10^{-4} && 55 \le v \le 72.2\ km/s \end{aligned} \qquad \textit{Equation 2-1}$$

The velocity distribution, *n(v),* has units of a number per km/s. Using the above relationship, the average velocity of micrometeoroids with respect to Earth in low earth orbit is estimated to be about 17 km/sec. The normalized meteoroid velocity distribution is shown in the following figure.

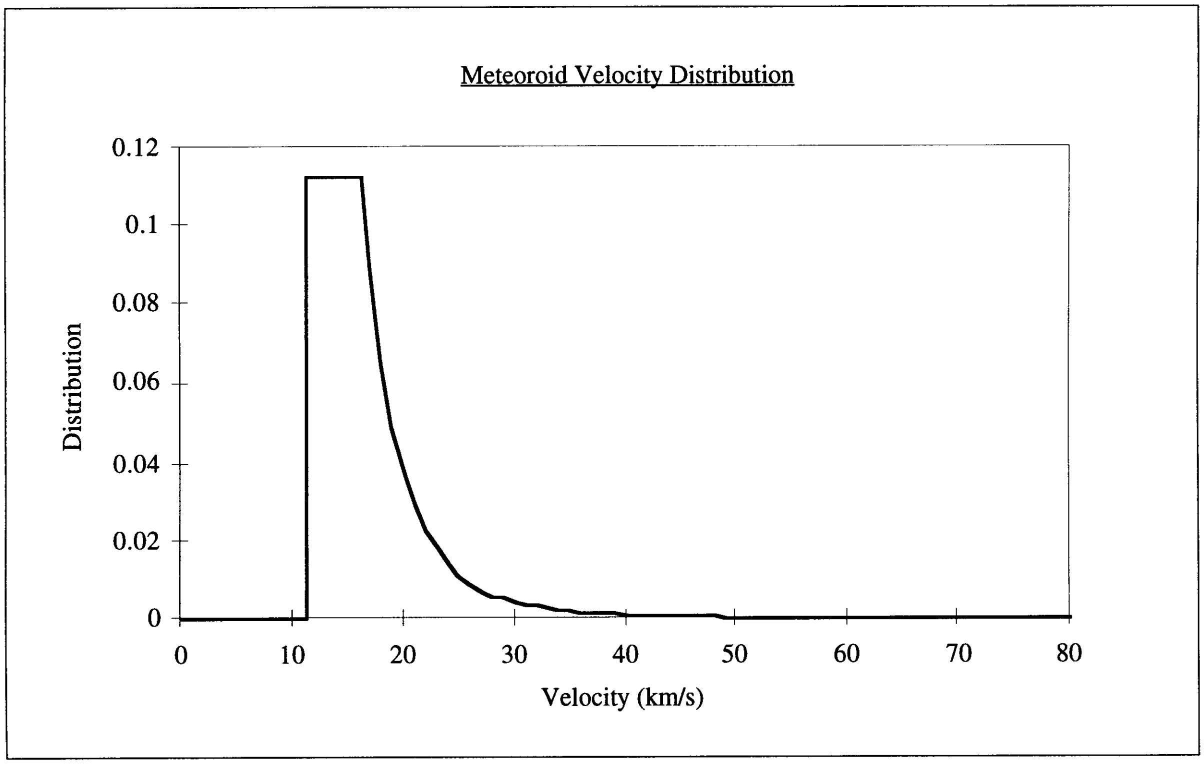

Figure 2-1. Normalized Meteoroid Velocity Distribution.

The HETE-2 will be orbiting the Earth in a such way that the SXCs are always pointing away from the Sun. The orbital velocity of HETE-2 is about 7.56 km/s. As a result, during one half of its orbit, the encounter velocity of meteoroids with respect to SXC will be higher than the average velocity of meteoroids with respect to the Earth. During the other half of its orbit, the encounter velocity of meteoroids with respect to SXC will be less than the average velocity of meteoroids with respect to Earth. Since these two factors average out, it is assumed that the average encounter velocity of meteoroids with respect to SXC is about 17 km/s.

2.3 Meteoroid Flux

The meteoroid flux is given in terms of the cumulative flux, which is the number of particles per m^2 per year for a mass greater than or equal to that mass, against a randomly tumbling surface. The interplanetary flux at 1 AU is described in the following equation for mass less than about 10 g [Anderson and Smith, 1994].

Equation 2-2

$$F_r(m) = c_0[(c_1 m^{0.306} + c_2)^{-4.38} + c_3(m + c_4 m^2 + c_5 m^4)^{-0.36} + c_6(m + c_7 m^2)^{-0.85}]$$

where

$c_0 = 3.156 \times 10^7$

$c_1 = 2.2 \times 10^3$

$c_2 = 15$

$c_3 = 1.3 \times 10^{-9}$

$c_4 = 10^{11}$

$c_5 = 10^{27}$

$c_6 = 1.3 \times 10^{-16}$

$c_7 = 10^6$

The above interplanetary meteoroid flux must be converted to the meteoroid flux at 600 km above the Earth to estimate the meteoroid flux that HETE will encounter. Because of the Earth's presence, two factors must be applied to the interplanetary meteoroid flux. One is the Earth shielding factor and the other is the focusing factor due to the Earth's gravity.

$$\text{Shielding Factor } = \frac{(1+\cos\eta)}{2}$$

where

$$\eta = \sin^{-1}\left(\frac{R_E}{R_E + H}\right)$$ *Equation 2-3*

R_E: Earth radius + 100 km atmosphere (6578 km)

H: height above Earth's atmosphere

The shielding factor varies from 0.5 at just above the atmosphere to 1.0 in deep space. The following equation shows the focusing factor.

$$\text{Focusing Factor } = 1 + \frac{R_E}{r}$$

R_E: Earth radius + 100 km atmosphere (6578 km) *Equation 2-4*

r: orbital radius

The above focusing factor increases the meteoroid flux as the orbit of the spacecraft approaches the Earth.

The meteoroid flux for SXC must consider the field of view of the CCD, mask open fraction, and the total area of CCD, as well as the focusing and shielding factor at 600 km altitude. As discussed in section 1.3, the two CCDs in one SXC have field of view of 1 steradian and have an effective area of 37.82 cm^2. The open slits of the coded mask make up the total open fraction of 0.2. Therefore, the unit of meteoroid flux for a SXC becomes the number of particles or impacts per 37.82 cm^2 per year per 1 steradian per 0.2 open fraction. The cumulative meteoroid flux in a 600 km orbit is plotted in the following figure. The mass of meteoroids is converted into a diameter in microns.

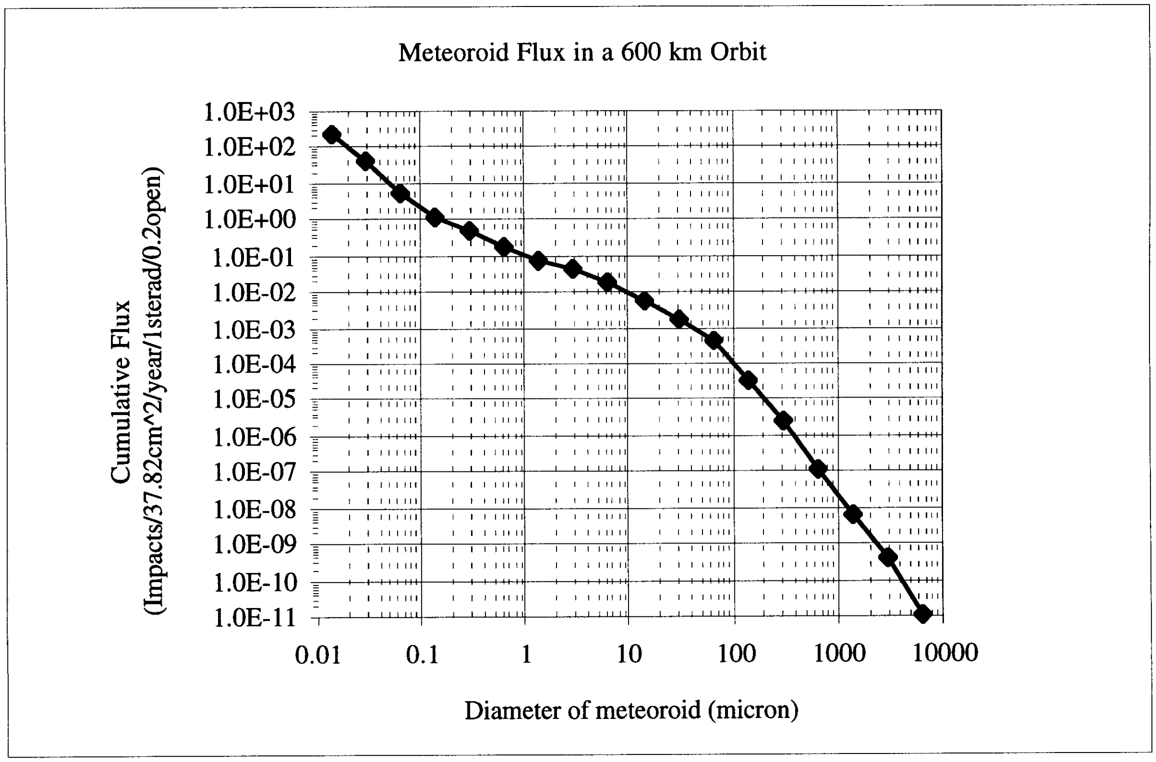

Figure 2-2. Cumulative Meteoroid Flux in 600 km orbit.

2.4 Composition of Micrometeoroids

The study by Smith et al. suggest that the composition of micrometeoroids is strongly dependent on the region of the mass spectrum being considered. They studied a total of 71 natural microcraters which occur on glassy lunar spherules collected by Apollo 15. These were compared with the craters produced on tektite and soda lime glass and quartz crystals by the impact of hypervelocity solid microparticles from an electrostatic particle accelerator. A scanning electron microscope and an optical microscope were used to measure the depth and diameter of the craters. The crater diameter distribution indicates that the smallest craters are most abundant with a gradual reduction in occurrence with increasing size. They discovered interesting result when χ, the ratio of depth to diameter of the craters, versus the number of craters, ϕ is considered. The following histogram shows the relationship between χ and ϕ and indicates the craters can be divided into three distinct groups:

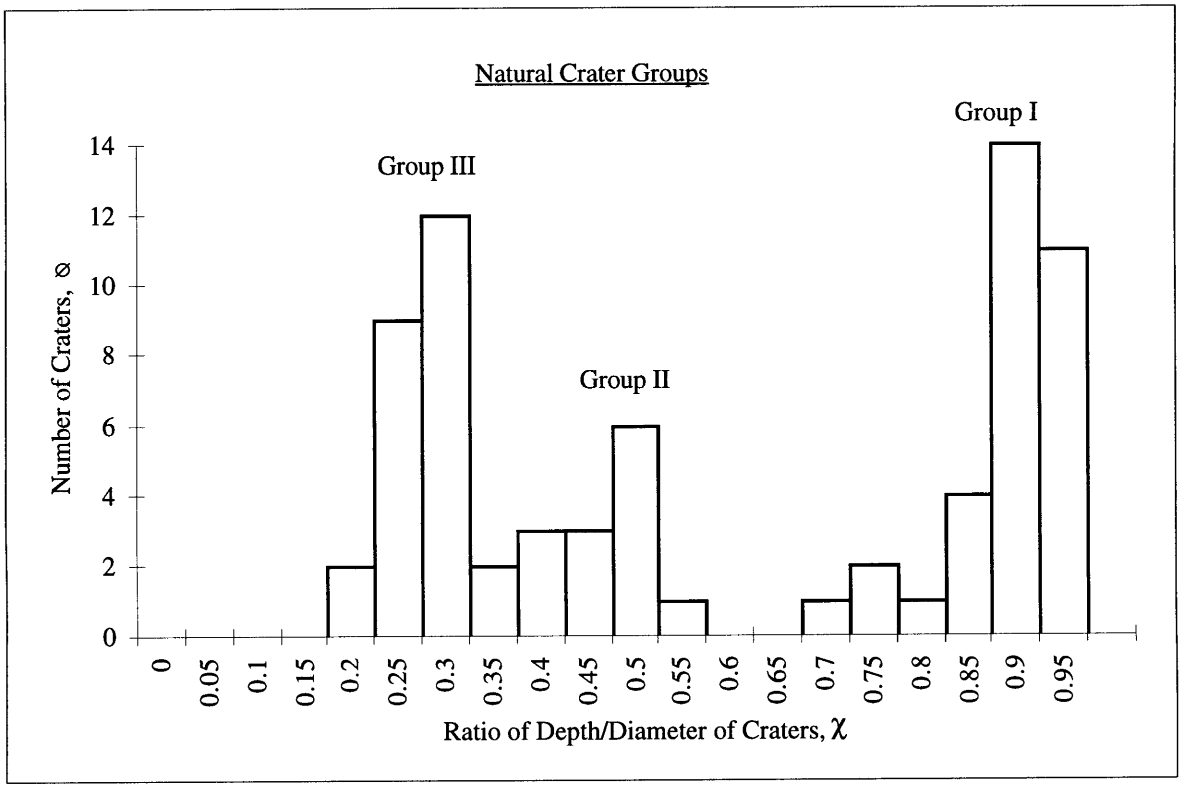

Figure 2-3. Histogram of Natural Crater Groups.

Based on the above observation, it can be speculated that the three groups either result from three groups of micrometeoroids with different physical properties, or from three different velocity groups of micrometeoroids. To understand the above result, Smith et. all produced craters in soda lime glasses which have similar physical properties to the lunar glasses. The craters were produced by impact from iron and aluminum microparticles from 0.5 micron to 6 micron in diameter, which are accelerated electrostatically to impact velocities of 1-7 km/s by using a Van de Graaff Generator. Iron projectiles (density of 7.9 g/cm^3) were chosen because these have physical properties similar to iron meteoroids. Likewise, aluminum was also used because its density (2.7 g/cm^3) and melting point are similar to those of the stony or chondritic meteoroids. Approximately 60 laboratory created craters were studied and the results are plotted in the same kind of histogram in the following figure.

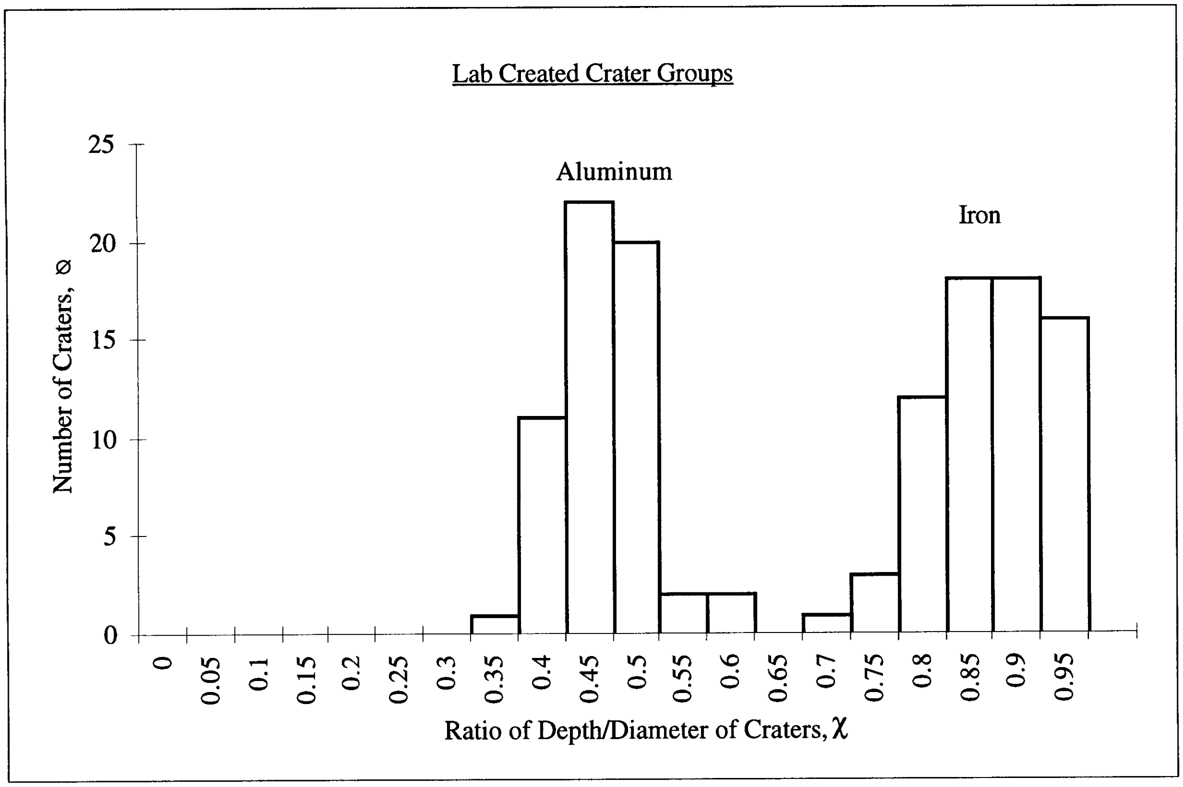

Figure 2-4. Histogram of Laboratory Created Crater Groups.

Figure 2-4 shows groupings of craters created by iron and aluminum projectiles on soda lime glass. By comparing Figure 2-3 and Figure 2-4, the iron projectile peaks match with the Group I craters and the aluminum projectile peaks match with the Group II craters [Smith and Adams, 1974]. At the same time, studies by Nagel et al. suggest that χ is only weakly dependent on the impact velocity [Nagel et al., 1976]. Based on the above correspondence of experimental craters with natural craters, and the relatively weak dependence of χ with impact velocity, it was suggested that the three natural crater groups result from the impacts of micrometeoroids of distinctly different physical properties. Therefore, particles that caused Group I craters with the high χ values are most likely iron micrometeoroids, and the particles that caused Group II and III craters with low χ values are most likely low density microparticles such as stony and carbonaceous chondrite materials, or ice crystals.

The next figure shows the histogram of the number of craters, ϕ, versus the crater diameter from each group.

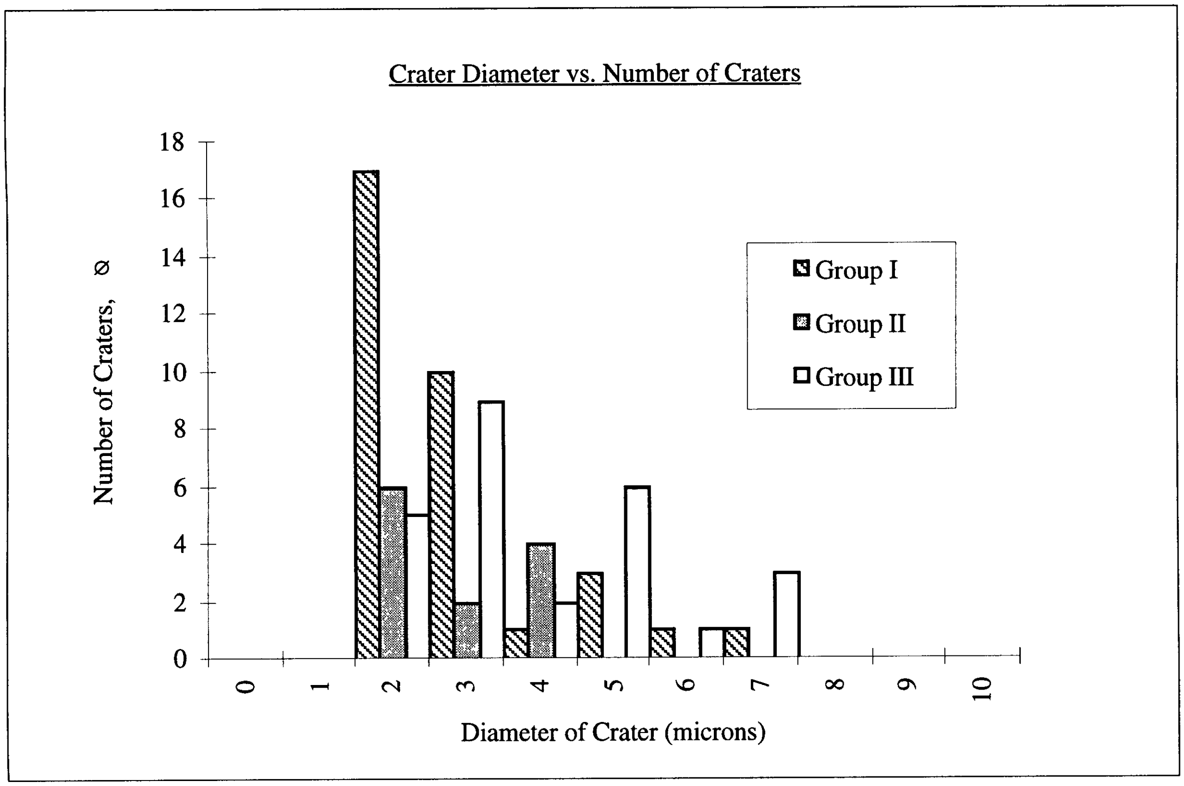

Figure 2-5. Number of Craters vs. Diameter of Crater for Each Group.

The Figure 2-5 shows a very rapid increase in number of craters for Group I iron micrometeoroids and a much slower increase for Group II and III as the crater diameter decreases. Therefore, this observation suggests that the iron type micrometeoroid has an increasing contribution to the total micrometeoroid flux in the 0-10 micron size region. Figure 2-5 can be converted into Figure 2-6 which is a plot of the differential flux versus the size of micrometeoroids.

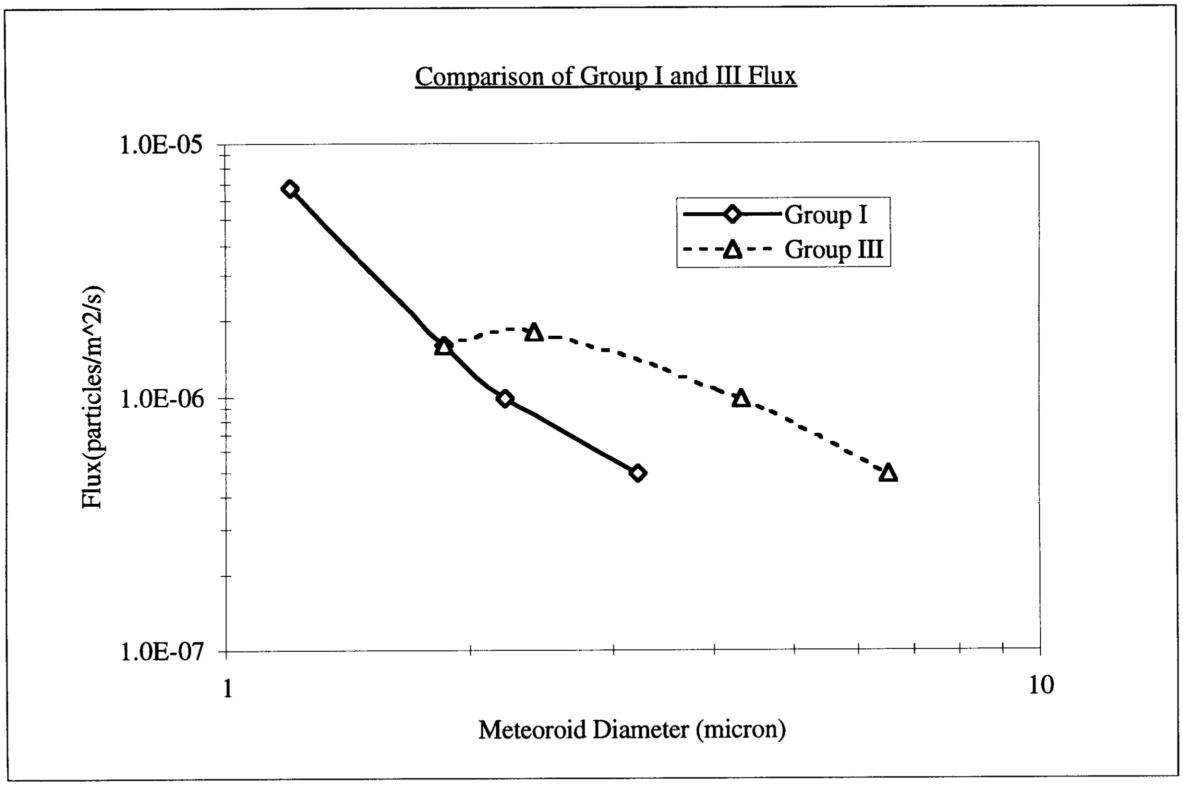

Figure 2-6. Comparison of Group I and III Flux.

The differential flux in Figure 2-6 is obtained by summing the total number of craters observed in the intervals of crater diameter. This plot indicates that for a particle diameter larger than about 2 microns, the major fraction of micrometeoroids is made up of low density material. On the other hand, as the particle diameter gets smaller than about 2 microns, the high density micrometeoroids start to dominate. This phenomenon can be explained by the effects of solar radiation pressure, which acts against solar gravity to exclude very small particles from the Solar system. This pressure is differential because it affects more severely on the low density materials and is thus expected to influence the flux of the Group III micrometeoroids to a greater extent than those of Group I. The negative slope of the Group III curve in Figure 2-6 reflects the increasing effects of the solar pressure with decreasing size of particles. Therefore, these studies show that the differential flux of iron type micrometeoroids increases rapidly as their size decreases to diameters below about 2 micron. For micrometeoroids with diameters larger than 2 microns, low density micrometeoroids increasingly contribute to the total flux. According to Anderson et al., the recommended mean values are 2 g/cm3 for meteoroids smaller than 10^{-6} g and 1g/cm3 for meteoroids between 10^{-6} and 0.01g and 0.5g/cm3 for masses above 0.01g [Anderson and Smith, 1994]. This recommendation supports the accepted view that iron type meteoroids represent only a very small fraction of the total mass of meteoroids. However, the observation by Smith et. all suggests that a large fraction of the total flux of micrometeoroids must be the high density iron type in the particle diameter range of 0.1 - 2 micron.

2.5 Uncertainty in the Meteoroid Environment

Except for small cosmic dust grains directly collected from the stratosphere, the physical properties of meteoroids must be determined by relatively indirect means, examination of impact craters, optical scattering, etc. Since they are known to originate from comets and asteroids, there is considerable uncertainty in their properties. In particular, the uncertainty in mass tends to dominate the uncertainties in the flux measurement. For meteoroids less than 10^{-6} g, the mass is uncertain to within a factor from about 0.2 to 5 times the estimated value, which implies the flux is uncertain to within a factor of 0.33 to 3 at a given mass. For meteoroids above this size, the flux is well defined but the associated mass is even more uncertain [Anderson and Smith, 1994].

Chapter 3

ORBITAL DEBRIS

3.1 Background

The natural meteoroid flux discussed in chapter 2 represents, at any instant, a total of about 200 kg of mass within 2000 km of the Earth's surface, most of it concentrated in the 0.1 mm meteoroids. Within this same 2000 km, there is an estimated 1.5 to 3 million kg of manmade orbiting objects. Most of these are in high inclination orbits where they pass each other at an average speed of 10 km/s. Most of this mass is concentrated in about 3000 spent rocket stages, inactive payloads, and a few active payloads. These objects are currently tracked by the USAF Space Command radars. Other 4000 objects, the result of over 100 on-orbit satellite fragmentations, are also being tracked by US Space Command radars. These 4000 objects from on-orbit satellite fragmentation represent only a smaller amount of mass, about 40000 kg [Kessler, 1994]. Recent ground telescope measurements of orbiting debris combined with analysis of hypervelocity impact pits on the returned surfaces of Solar Max indicate that there is a total mass of about 1000 kg for orbital debris sizes of 1 cm or smaller, and about 300 kg for orbital debris smaller than 1 mm. This distribution of mass and relative velocity is sufficient to cause the orbital debris environment to be more hazardous than the meteoroid environment to most spacecraft operating in Earth orbit below 2000 km altitude [Kessler, 1988].

3.2 The Orbital Debris Environment Model (ORDEM)

A semi-empirical computer based orbital debris model, ORDEM, has been developed by Kessler et al in 1996 which combines direct measurements of the orbital debris environment with a theoretical model [Kessler et al., 1996]. First, a curve fit to the debris environment was developed based on the best experimental data available. This was then coupled with additional terms which represent a projection of the expected environment changes in the future. In the past, the most easily used orbital debris models were semi-empirical sets of equations which described the orbital debris flux as a function of debris diameter and spacecraft orbital altitude, inclination, and time of interest. These equations were derived based on the small amount of available data. However, as a result of measurements by the Haystack radar and the LDEF satellite, it has been discovered that small pieces of debris are present in certain inclinations in larger quantities than in others. Also, the LDEF measurement demonstrated that small debris was more likely to be found in highly elliptical orbits than large debris. The computer based ORDEM model has been written in order to accurately reflect these findings. The input parameters are the calendar year, the solar activity in the year, the altitude and the inclination of the orbit of a spacecraft or the latitude of the fixed point. The ORDEM can be downloaded from NASA's web page (http://see.msfc.nasa.gov/see/mod/models.html) and requires less than 1 second to calculate the results. The output parameters are the cumulative flux, average velocity, velocity and angular distribution. The ORDEM has been recommended for most NASA engineering applications since mid-1990 and is still recognized as the best available, and valid within stated uncertainties. No improvements or updates are expected in the near future.

3.3 Composition of Orbital Debris

The major source of orbital debris can be divided into six different groups based on the size. They are intact objects, large fragments, small fragments, sodium/potassium particles, paint flakes, and Al_2O_3 particles. The size ranges for these groups are shown in the following table [Kessler et al., 1996].

Composition	Range of size
Intact objects	$d > 50$ cm
Large fragments	1 cm $< d <$ 50 cm
Small fragments	200 μm $< d <$ 1 cm
Na /K particles	200 μm $< d <$ 1 cm
Paint flakes	20 μm $< d <$ 200 μm
Al_2O_3 particles	$d <$ 20 μm

Table 3-1. Composition of Orbital Debris and the Range of Size.

Intact Objects:

The intact objects represent spent satellites, rocket bodies and operational debris. The intact objects are tracked and catalogued by the US Space Command.

Large Fragments:

Fragmentation from collisions and low or high intensity explosions produces large fragments. About 15% of these collisions and explosions were related to propulsion system malfunctions and over 40% were deliberate. The remaining 45 % of the breakups have no known cause [Larson & Wertz 1992]. The number of large fragments has been obtained based on the US Space Command catalogue and the output of NASA's Orbital Debris Evolutionary Model, EVOLVE.

Small Fragments:

Collisions and high intensity explosions can also produce small fragments. Aluminum or aluminum oxide slag particles produced by solid rocket motors are other sources of small fragments. Chemical analysis of LDEF craters suggests that either fragmentations or slag particles from solid rocket motors were the origin of these small particles. In ORDEM, the number of small fragments has been determined in such a way that the flux at 1 cm and larger, combined with large fragments, is consistent with Haystack radar measurements. The flux in the size range from 100 μm to 1 mm, combined with paint flakes, is consistent with LDEF data.

Sodium/Potassium Particles:

The sodium/potassium particles are assumed to originate from leaks of nuclear reactor coolant used in certain satellites. Haystack radar measured a concentration of debris less than 2 cm in size between 850 km and 1000 km altitude, with an inclination near 65°. The most likely sources are identified as Russian RORSATS. It is believed that they may be leaking their liquid metal sodium/potassium coolant.

Paint Flakes:

Paint flakes come from degradation of satellite surfaces. The chemical analysis of craters on satellite surfaces returned from space have shown that the paint flakes are an important source of orbital debris. The number of paint flakes is proportional to the number of large structures in orbit, and the density of atomic oxygen which the structures encounter at various altitudes in Earth's exosphere.

Aluminum Oxide Particles:

Finally, aluminum oxide (Al_2O_3) particles are generated by the result of solid rocket motor burns. Although the SXC is concerned about particles of all sizes, later section will show that the particles smaller than 20 μm are the major threat to the SXC due to their high flux. As a result, most particles that will affect the CCD are these Al_2O_3 particles.

3.4 Orbital Debris Flux

The cumulative flux of orbital debris with diameter, d, and larger on a randomly tumbling spacecraft orbiting at altitude, h, inclination, i, the calendar year, t, when a solar activity was S, is given by the following equation [Anderson and Smith, 1994]:

$$F_r(d,h,i,t,S) = H(d)\phi(h,S)\psi(i)[F_1(d)g_1(t) + F_2(d)g_1(t)] \qquad \textit{Equation } 3-1$$

where

F_r = *Cumulative orbital debris flux, impacts per square meter per year*

d = *orbital debris diameter in cm,* $(10^{-4} \le d \le 500)$

t = *calendar year (example: year 2000)*

h = *altitude in km*

S = *solar radio flux* $(10^4\ Jy)$

i = *inclination in degrees*

$$H(d) = [10^{exp^{(-(log_{10} d - 0.78)^2 / 0.637^2)}}]^{1/2}$$

$$\phi(h,S) = \phi_1(h,S)/((\phi_1(h,S)+1)$$

$$\phi_1(h,S) = 10^{(h/200 - S/140 - 1.5)}$$

$$F_1(d) = 1.22 \times 10^{-5} d^{-2.5}$$

$$F_2(d) = 8.1 \times 10^{10} (d+700)^{-6}$$

$$g_1(t) = (1+q)^{(t-1988)} \qquad for\ t < 2011$$

$$g_1(t) = (1+q)^{23}(1+q')^{(t-2011)} \qquad for\ t > 2011$$

$$g_2(t) = 1 + p(t-1988)$$

p = *assumed annual growth rate of mass in orbit* = 0.05

$q = 0.02$, *estimated growth rate of fragment mass for* $t < 2011$

$q' = 0.04$, *estimated growth rate of fragment mass for* $t > 2011$

$\psi(i)$ = *Inclination dependent constant*

Using ORDEM, which incorporates the above flux equations, the flux of orbital debris for HETE-2 SXC can be estimated. After running the ORDEM with parameters for the HETE-2 orbit and launch year, which are 600 km altitude, 0° inclination, and the launch year of 2000, the program generates an output file that includes the cumulative flux expressed as number of particles or impacts per m^2 per year. Since the ORDEM calculates the flux for a randomly tumbling surface, the unit of flux includes 2π steradian which is equal to the field of view of a flat surface. The walls of SXC only allow the CCDs with 1 steradian field of view. The total area of two CCDs in one SXC is 37.82 cm^2. In addition, the 20% open fraction of the mask must be accounted for. Thus, the unit is converted into 'impacts/37.82 cm^2/year/1sterad/0.2 open'. The following plot shows the cumulative flux of orbital debris in HETE-2 orbit.

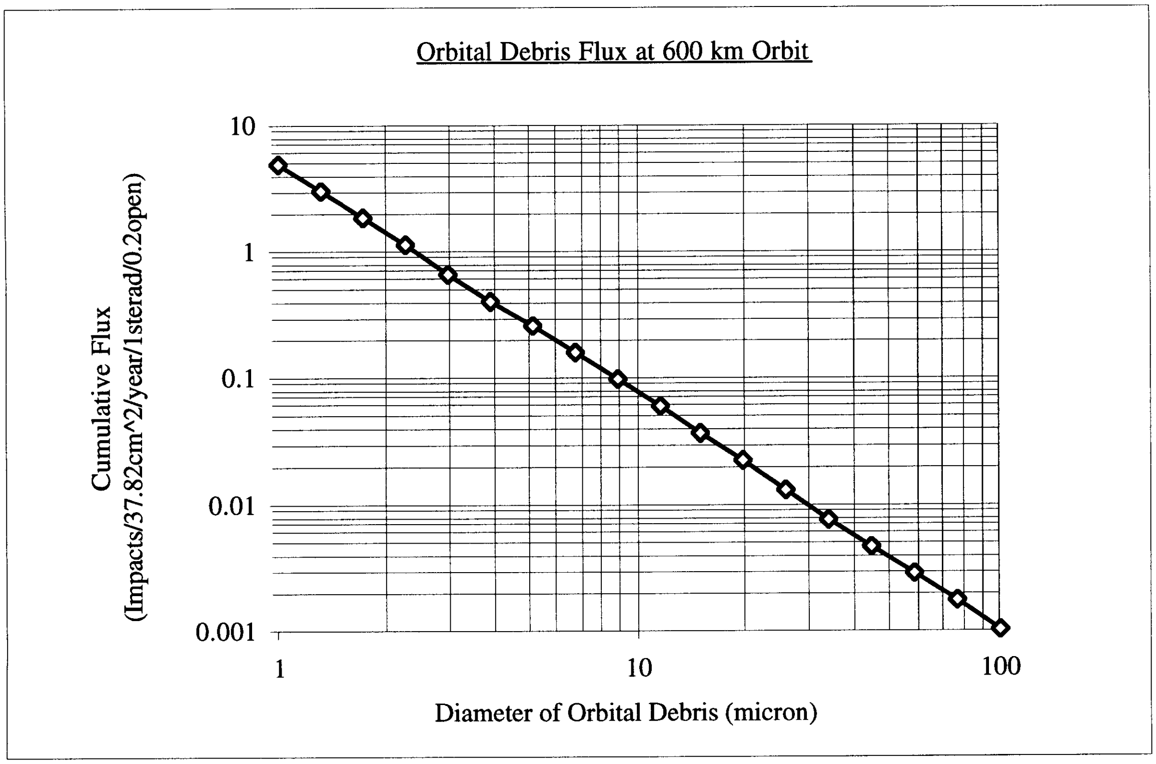

Figure 3-1. Cumulative Orbital Debris Flux In HETE-2's Orbit.

The above plot shows that if there were no shielding, orbital debris larger than or equal to 1 μm would impact the CCDs about 5 times a year. On the other hand, the flux for the same sized micrometeoroid was only about 0.1 impacts per year according to the micrometeoroid flux plot in Figure 2-2. Therefore, this comparison shows that there is considerably more threat from orbital debris than from micrometeoroids for the SXC. The following figure shows the flux comparison between orbital debris and micrometeoroids in the diameter range from 1 to 100 μm:

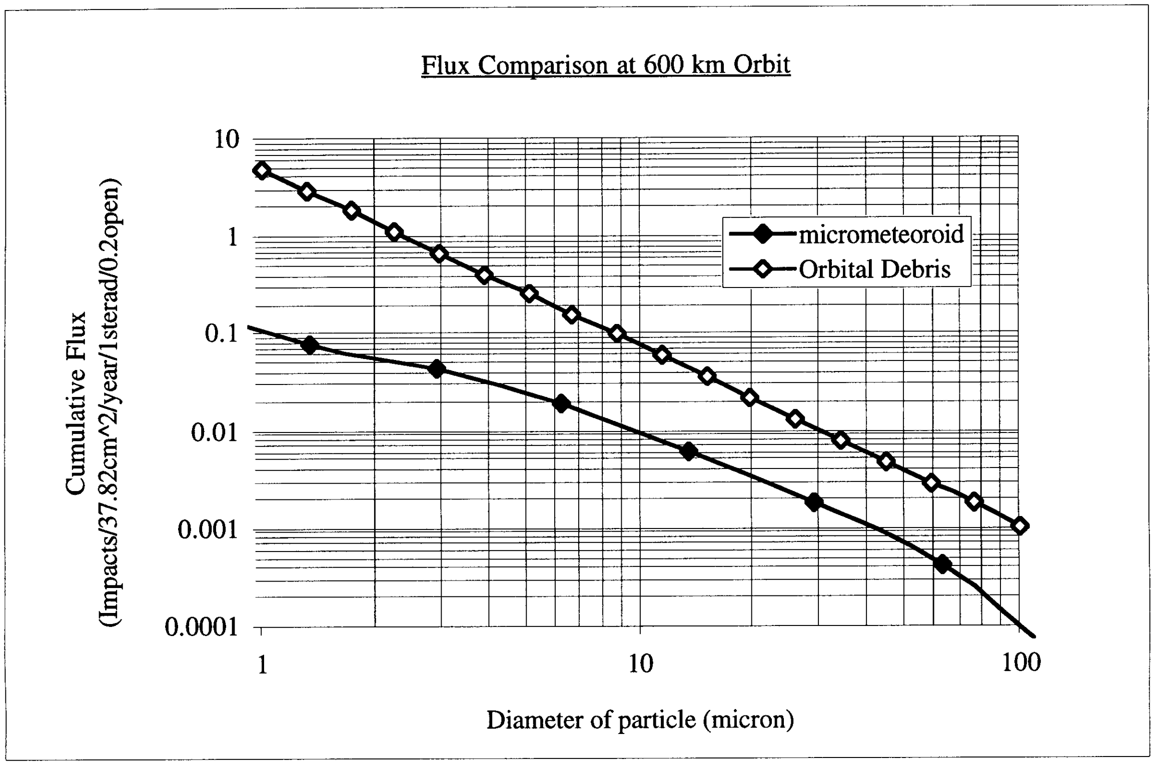

Figure 3-2. Comparison of Micrometeoroid and Orbital Debris Flux in HETE-2 Orbit.

3.5 Velocity of Orbital Debris

The following equation 3-2 shows the velocity distribution of orbital debris. The output from this equation is the number of impacts for different velocity ranges [Anderson and Smith, 1994]. This velocity distribution is averaged over all altitudes.

Equation 3-2

$$f(v) = (2v\,v_0 - v^2)\,\left[G\,e^{-\left(\frac{(v - A\,v_0)}{(B\,v_0)}\right)^2} + F\,e^{-\left(\frac{(v - D\,v_0)}{(E\,v_0)}\right)^2}\right] + H\,C\,(4\,v\,v_0 - v^2)$$

where

$f(v)$: *the number of impacts with velocities between* v *and* $v + dv$

v: *collision velocity* (km/s)

$$A = 2.5$$

$$B = \begin{cases} 0.5 & \text{for } i < 60 \\ 0.5 - 0.01(i - 60) & \text{for } 60 < i < 80 \\ 0.3 & \text{for } i > 80 \end{cases}$$

$$C = \begin{cases} 0.0125 & \text{for } i < 100 \\ 0.0125 + 0.00125(i - 100) & \text{for } i > 100 \end{cases}$$

$$D = 1.3 - 0.01(i - 30)$$

$$E = 0.55 + 0.005(i - 30)$$

$$F = \begin{cases} 0.3 + 0.0008(i - 50)^2 & \text{for } i < 50 \\ 0.3 - 0.01(i - 50) & \text{for } 50 < i < 80 \\ 0.0 & \text{for } i > 80 \end{cases}$$

$$G = \begin{cases} 18.7 & \text{for } i < 60 \\ 18.7 + 0.0289(i - 60)^3 & \text{for } 60 < i < 80 \\ 250.0 & \text{for } i > 80 \end{cases}$$

$$H = 1.0 - 0.0000757(i - 60)^2$$

$$v_0 = \begin{cases} 7.25 + 0.015(i - 30) & \text{for } i < 60 \\ 7.7 & \text{for } i > 60 \end{cases}$$

The above function can be normalized using the following equation:

$$f'(v) = \frac{f(v)}{\int_0^{\infty} f(v)\,dv}$$

Equation 3-3

Using Equation 3-3, the normalized velocity distribution for an orbit with 0 degree inclination is plotted in the following figure.

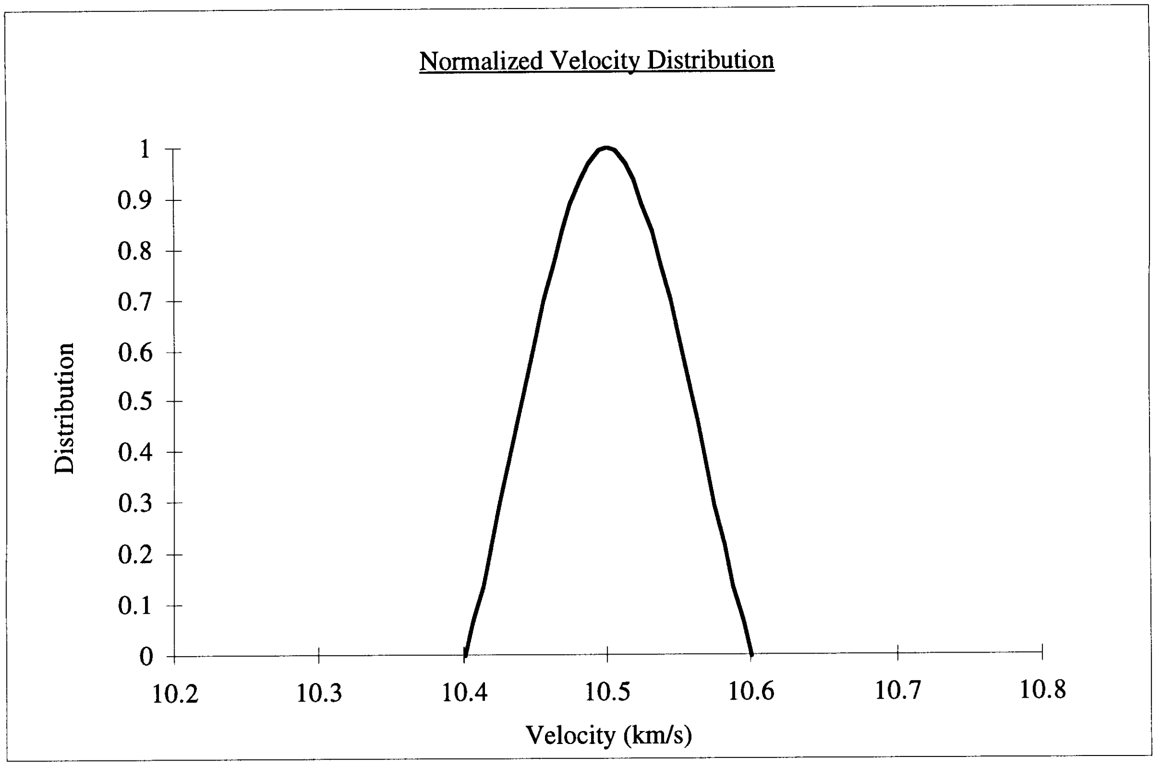

Figure 3-3. Orbital Debris Velocity Distribution for 0§ inclination

Above velocity distribution shows the orbital debris velocity sharply peaks at 10.5 km/s. The ORDEM program uses the above velocity distribution (Equations 3-2 and 3-3) to calculate the average velocity as well as the velocity distribution. The average velocity calculated by ORDEM agrees with the result in Figure 3-3.

3.6 Comparison of ORDEM with Measurement Data

Before the space age, knowledge of the space particle environment was based upon the Earth-bound study of the zodiacal light, meteors, comets, asteroids, and meteorites. Since then, several methods have been developed to collect particle data from space. The simplest of these methods is to expose a surface to the space environment, return it to Earth, and examine it for impacts. Micrometeoroid and orbital debris impacts at very high velocities produce characteristic craters in the samples. These craters can be analyzed to obtain information about the particles that caused them. The first microcraters found on experiments specifically designed for satellites were recovered from the Gemini and Skylab missions. Other recovered surfaces with microcraters were Apollo windows, the Surveyor III camera, and lunar rocks. These samples helped to establish the particle flux, or number of particles impacting a certain area over a given time. To update and refine models of micrometeoroid and orbital debris environment in low Earth orbit, some experiments were mounted on the NASA satellite Long Duration Exposure Facility (LDEF) and outside the Russian space station Mir.

The Mir space station has been in orbit at an altitude of 350-450 km with an inclination of 51.6 degree since February 1986. The French module Echantillons was placed outside the station during the Franco-Russian Aragatz mission. It was deployed on December of 1988 and recovered 13 months later. Its average altitude during this time was 387 km. The module consisted of various experiments intended to investigate the space environment.

The NASA LDEF was launched into LEO at 482 km altitude by the Space Shuttle Challenger in April 1984. It was retrieved by the Space Shuttle Columbia after 69 months. The satellite was a 14-sided, roughly cylindrical shaped polygon, with a 5 meter diameter and 10 meter long aluminum frame. The experiments were stored in trays fixed to the aluminum frame. These trays faced in 14 directions, 12 along the sides which are called rows and 2 on the ends. During its mission, LDEF was stabilized with the long axis continually pointed toward the center of the Earth so that the rows remained at fixed angles relative to the direction of orbital motion [Berthoud and Mandeville, 1997].

The following two plots compares the flux prediction by ORDEM with the flux measurement from Mir and LDEF.

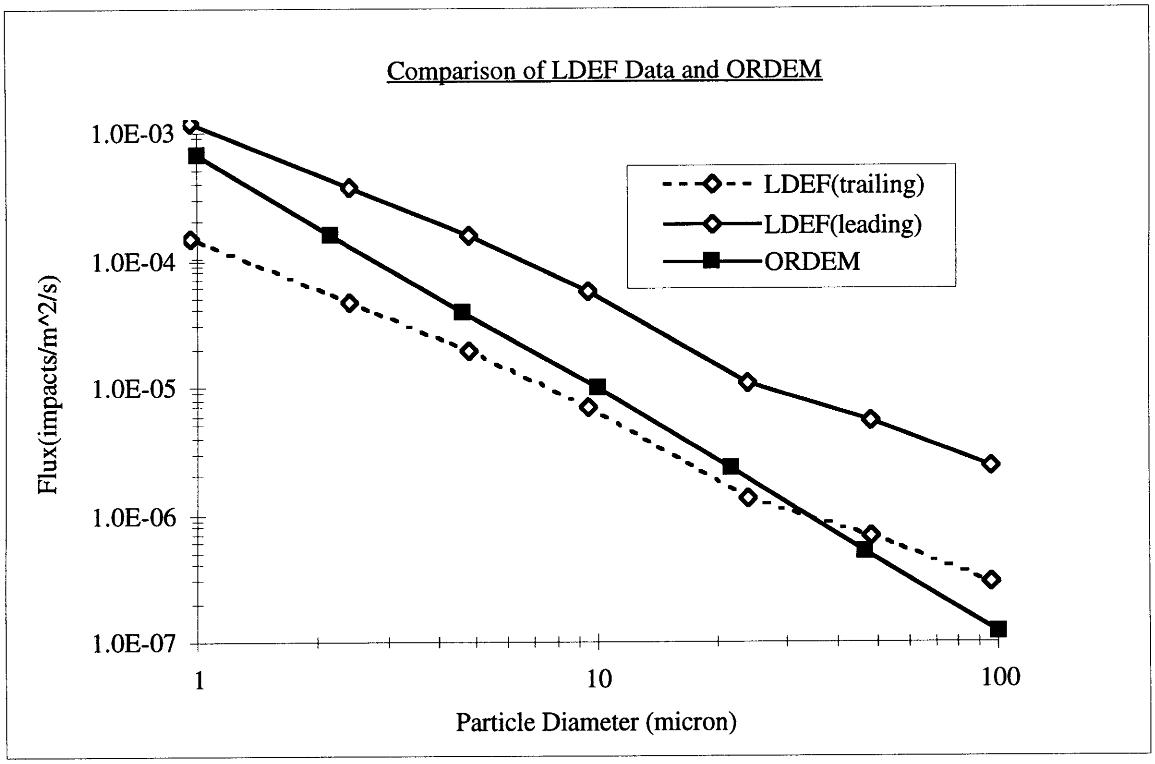

Figure 3-4. Comparison of ORDEM Prediction with LDEF Data.

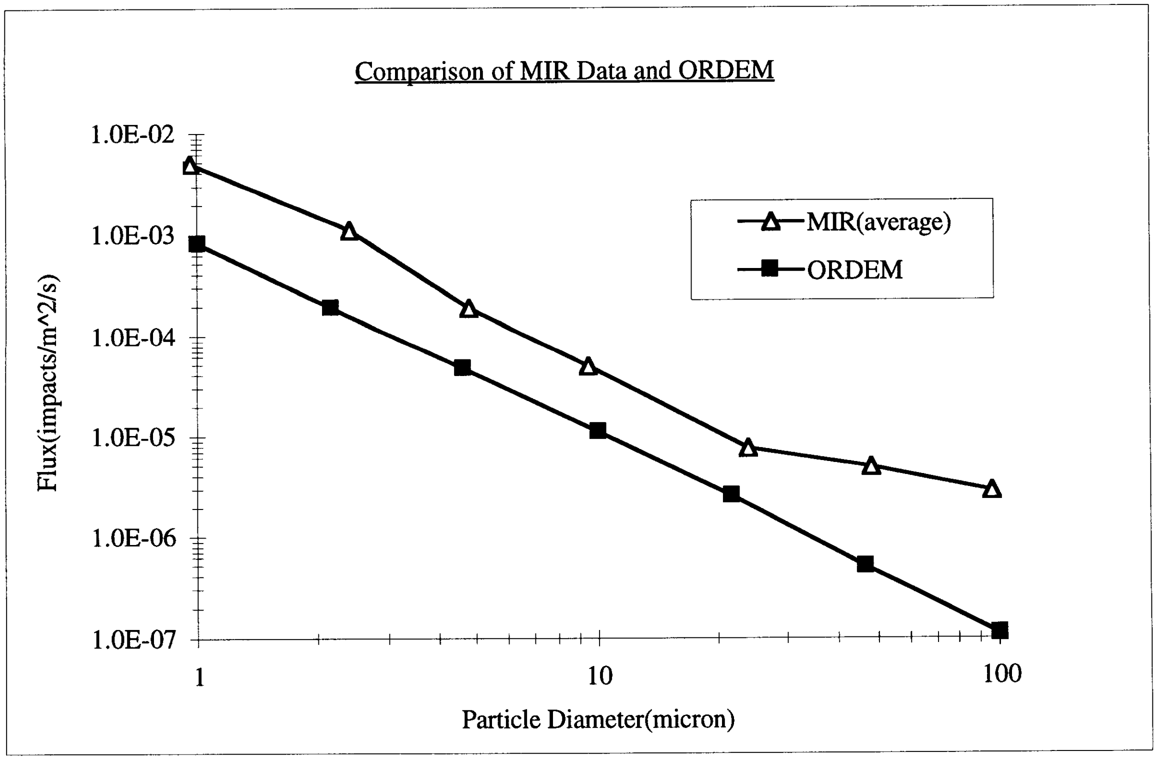

Figure 3-4. Comparison of ORDEM Prediction with MIR Data.

The above data from MIR and LDEF consider only orbital debris but not micrometeoroids. The collected materials from MIR and LDEF are chemically analyzed in order to distinguish craters due to the orbital debris and micrometeoroid impacts. The comparison in Figure 3-3 shows that the ORDEM prediction lies between the LDEF leading edge and the trailing edge flux measurement. Since ORDEM estimates flux for a randomly tumbling surface, it is reasonable that the randomly tumbling surface has a higher flux than the trailing edge of LDEF and a lower flux than the leading edge of LDEF. As the particle size gets larger than about 30μm, the ORDEM flux prediction becomes even less than the LDEF trailing edge flux. But for particles smaller than about 30μm, the ORDEM prediction agrees reasonably well with LDEF data. The comparison of MIR data and ORDEM prediction in Figure 3-4 shows that the MIR measurement is much higher than the ORDEM prediction. It was postulated that the extra particles are due to the dirty environment of a manned station. With the arrival, docking, and departure of several vehicles during the time of exposure, secondary particles were generated. Although these particles have relatively low velocity with respect to the station, the continual generation of secondary particles would produce more than the predicted amount of space debris.

The Space Shuttle provides a means of monitoring the environment over time. Shuttle windows are examined after each flight for damage by orbital debris and micrometeoroid impacts, and numerous windows have been replaced due to impact damage. The Shuttle usually flies at altitudes around 300 km, considerably lower than 460 km altitude of LDEF. Previous orbital debris models predicted a considerably lower orbital debris flux on the Shuttle at these lower altitudes than on LDEF. However, the orbital debris flux indicated by the Shuttle is comparable to the LDEF flux [Kessler et al., 1996]. The data obtained by Shuttle with 28.5 degree inclination and 300 km altitude in 1992 is compared to the predicted flux by ORDEM in the following figure.

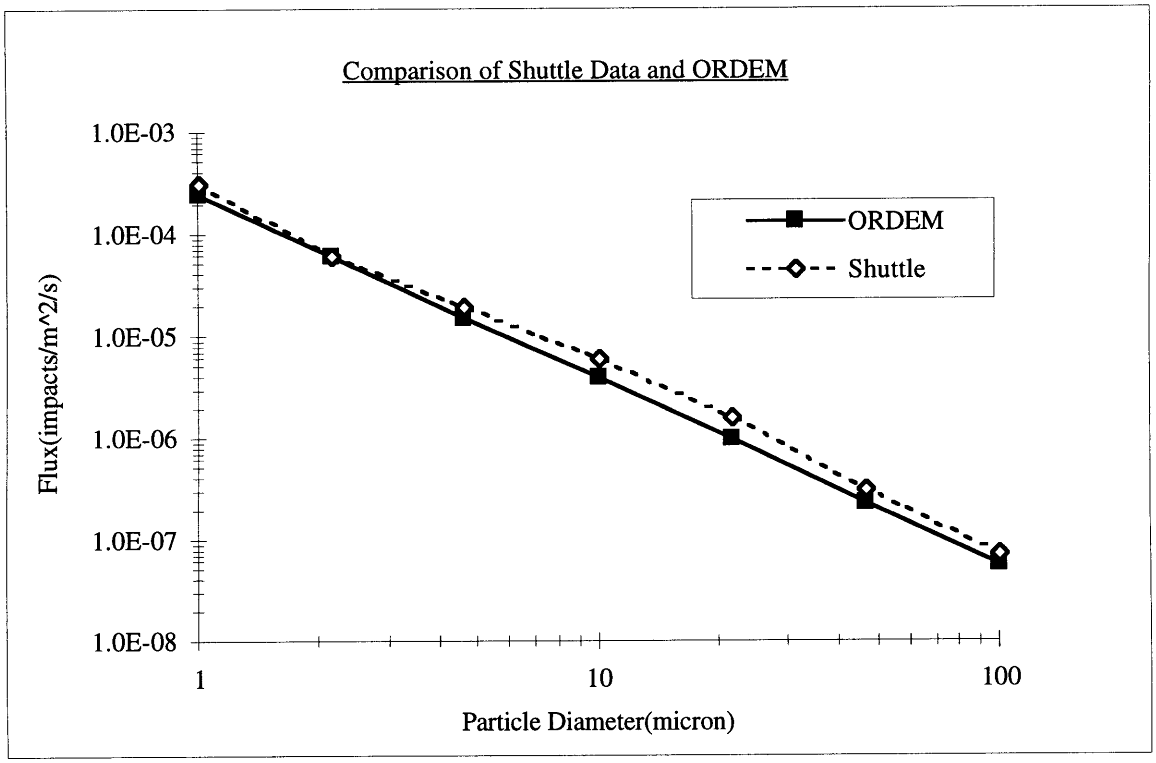

Figure 3-4. Comparison of ORDEM Prediction with Shuttle Data.

The above figure shows the flux for a typical Shuttle mission in comparison with the predicted flux by ORDEM. Indeed, the fluxes in the 1-100 micron region are of the same order, indicating the ORDEM is also consistent with the Shuttle data. This is no surprise because the ORDEM reflects the fact that the orbital debris flux indicated by the Shuttle is comparable to the LDEF flux although altitude of a typical Shuttle is lower than that of LDEF.

3.7 Uncertainties of ORDEM

The ORDEM program is valid for the vast majority of cases including collision risk assessment, shielding design, and the planning or evaluation of observations. However, ORDEM is not designed for any particular condition, and there are some uncertainties to this model. An orbital debris model with the prediction of future trends is difficult to develop and subject to substantial uncertainty. There are two kinds of uncertainties: uncertainties in the current environment and uncertainties related to the future trend prediction [Anderson and Smith, 1994].

3.7.1 Uncertainties in the Current Environment

The uncertainties in the current environment multiply the flux by a factor which is independent of time. They include uncertainties of measurement, statistical limitations of the data sets, and debris shape and density information. The data sets are also measured from limited parts of orbits from certain altitudes and inclinations. For orbital debris size larger than 10 cm in diameter, the environment is generally measured by ground radars. The most extensive measurements were made by the USAF Space Command, which also maintains a catalog of the debris population. While these data provide an adequate description of the distributions of large debris with respect to altitude and inclination, analysis of GEODSS optical telescope data has shown that the radars detects and the Space Command catalogs less than half of the population in this size range. This information has been incorporated in the ORDEM model, so the model represents the current environment in this size range accurately. Measurement of the debris flux for sizes smaller than 0.05 cm is made by analysis of impact craters on pieces of space hardware returned from orbit, such as MIR or LDEF experiments. The meteoroid impacts are distinguished from orbital debris impacts by analysis of the chemical elements retained in the crater. For sizes smaller than 0.05 cm, the flux has only been measured on hardware flown at about 500 km altitude. Until recently, the only measurements for orbital debris sizes between 0.05 cm and 10 cm were made by the MIT ETS telescopes. This provided measurements of the cumulative flux for objects believed to be 2 cm and larger. For intermediate sizes, the environment was estimated by a simple straight line interpolation. Later, this interpolation was confirmed by recent measurements by Arecibo and

Goldstone radars in the midrange between 0.2 and 2 cm. These measurements showed a flux rate that is consistent with the ORDEM model.

3.7.2 Uncertainties related to Future Trend Prediction

Unlike uncertainties in Section 3.7.1 which are independent of time, uncertainties related to future trend prediction alter the slope of flux versus time. These uncertainties are produced as a result of key assumptions that must remain valid in order for ORDEM to generate a valid flux prediction. These key assumptions are described in the following;

1. Over the past 10 years, the accumulation of total mass of manmade objects in space has increased at an average rate of 5% per year. Based on this trend, ORDEM model assumed that the rate of accumulation of mass in LEO is constant with 5% increasing rate. This is a key determinant of the expected debris growth rate. The combination of a decreasing launch rate for the United States with an increasing rate for the rest of the world has led to the relatively constant historical trend. However, it is not clear that this trend will continue. Expected launch rates are subject to the political and economical influences which can change unpredictably. Also, many new countries are starting to be involved in space launch activity. The annual growth rate of 5 % has been the case for the past decade and is expected to remain the same unless there is a substantial worldwide economic depression or similar events.
2. The model assumes that the relative use of certain preferred orbits will not change significantly and therefore will remain constant. For example, the history of launches by the USSR has been such that 80% of their payloads reenter within 2 years of launch. These do not contribute significantly to the debris environment. If this practice changed

with increased use of higher and longer life orbits, the population of objects in orbit would grow at a proportionally increased rate.

3. It is assumed that the efforts to minimize fragmentation of satellites in orbit will continue to generate the rate of one fragmentation event per year in LEO. Satellite breakups may be intentional or unintentional. In the past 10 years, intentional fragmentation of satellites accounted for about 70 percent of the known fragmentation events. Apparently, recent publicity and increased awareness of the hazards associated with orbital debris has generated policy shifts among the space-faring nations. As a result, no intentional fragmentation events above 300 km have been observed in the last 5 years. The ORDEM model assumes that the estimated growth rate of fragmented mass is 2% before the year 2011 and 5% after the year 2011. These rates are based on the assumption that there will be no intentional breakups, and an accidental breakup rate of 1 per year. The reason for a higher rate after the year 2011 is because the unintentional fragmentation rate caused by collisions is an exponential function of the population of satellites, although the unintentional fragmentation rate from satellite explosions remains in a linear relationship with the population of satellites.
4. It is assumed that the debris size distribution is independent of altitude. For circular orbits, it is known that the small debris decays faster than large debris. This may lead us to believe that there is an altitude-dependent relationship with the debris size, such that the population of small debris decreases as its altitude decreases. However, later studies show that there is the exact opposite altitude-dependence for elliptical orbits. So far, it has not been proven that there is a general dependent relationship between the debris size and altitude.

Chapter 4

IMPACT CRATERS

In Section 1.4, it was concluded that a crater about 0.5 μm deep on the CCD, caused by either orbital debris or micrometeoroid impacts, can lead to a failure of the CCD. The next step is to find out what kind of impact particles will cause craters that are deeper than or equal to 0.5 μm on the CCD. The size, density, and velocity of impact particles are the major parameters that change the depth of craters. This chapter will discuss the relationship between the impact particle and the crater caused by that particle.

4.1 Crater Depth Estimation

Several impact experiments have established empirical relationships which describe the depth of craters caused by hypervelocity impacts. These equations are developed using regression methods to approximate results of laboratory impact experiments. Assuming the impact particle is a sphere, the important variables for the impacting particle are its density, diameter, and velocity. For the target, its density and material properties are the major variables. The following figure shows a typical impact experiment.

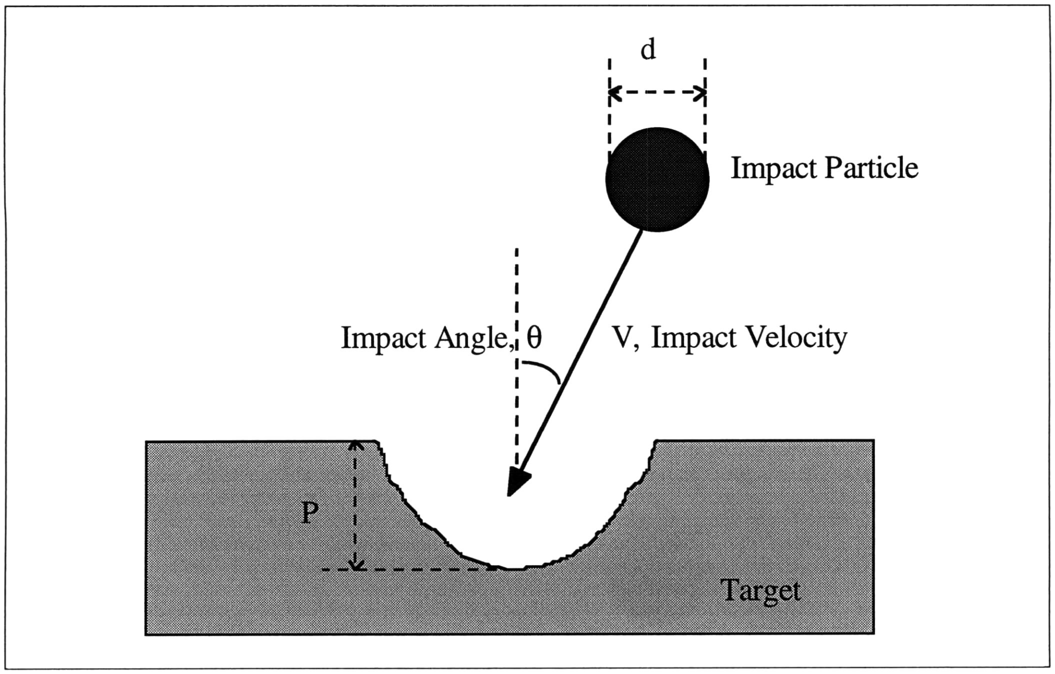

Figure 4-1. Impact Experiment.

Cour-Palais and Christiansen [Cour-Palais, 1987] performed impact experiments using projectile particles of size between 50 μm and 1.3 cm with velocity less than 12 km/s. They used aluminum as a target material. The following equation is generated to approximate their experimental data.

$$P = \frac{5.24 d^{1.056}}{H^{0.25}} \left(\frac{\rho_p}{\rho_t} \right)^{0.5} \left(\frac{V}{c_t} \right)^{0.667} \qquad \textit{Equation 4 - 1}$$

where

$P = crater\ depth(cm)$

$d = size\ of\ impact\ particle(cm)$

$H = Brinell\ hardness\ of\ target$

$\rho_p = density\ of\ particle(g/cm^3)$

$\rho_t = density\ of\ target(g/cm^3)$

$V = velocity\ of\ particle(km/s)$

$c_t = speed\ of\ sound\ in\ target(km/s)$

Frost [Frost, 1970], from NASA, ran a similar impact experiment. He used aluminum and stainless targets, and obtained the following equation.

$$P = K_{\infty} d^{1.056} \rho_p^{0.519} V^{0.667} \qquad \textit{Equation 4 - 2}$$

$where$
$P = crater\ depth(cm)$
$K_{\infty} = target\ material\ constant(0.42\ for\ aluminum\ and\ 0.25\ for\ steel)$
$d = size\ of\ impact\ particle(cm)$
$\rho_p = density\ of\ particle(g/cm^3)$
$V = velocity\ of\ particle(km/s)$

Grun [Grun and Pailer, 1979] from the Max-Planck Institute in Germany also performed impact experiment using various materials for projectile particles and targets. The projectiles used were micron-sized particles with velocities ranging from 1 to 20 km/s. The following equation is developed to approximate his experimental data.

$$P = \frac{0.772}{\varepsilon^{0.06} \rho_t^{0.5}} d^{1.2} \rho_p^{0.73} (V \cos\theta)^{0.88} \qquad \textit{Equation 4 - 3}$$

$where$
$P = crater\ depth(cm)$
$d = size\ of\ impact\ particle(cm)$
$\rho_p = density\ of\ particle(g/cm^3)$
$\rho_t = density\ of\ target(g/cm^3)$
$\varepsilon = ductility\ constant$
$V = velocity\ of\ particle(km/s)$
$\theta = impact\ angle$

From the above three crater equations generated by different impact experiments, the equation by Grun is the most relevant to the SXC. The experiment used micron-sized particles that are similar to the size of micrometeoroid and orbital debris with which the CCD is concerned. The projectile properties are summarized in the following table.

Projectile material	Density (g/cm3)	Mass range (g)	Diameter range (micron)	Speed range (km/s)
Iron	7.85	$2*10^{-10}$ - $5*10^{-13}$	3.65 - 0.50	1.4 - 13.3
Aluminum	2.7	$4*10^{-11}$ - $2*10^{-12}$	3.05 - 1.12	3.0 - 7.5
Glass	2.4	$2*10^{-10}$ - $6*10^{-12}$	5.42 - 1.68	1.5 - 4.2
Polyphenylene	1.25	$5*10^{-11}$ - $3*10^{-13}$	4.24 - 0.77	2.0 - 11.0

Table 4-1. Projectiles used in Grun's Experiment.

As discussed in the previous chapters, iron particles are similar to the micrometeoroids and aluminum particles are similar to the orbital debris. Since Grun's experiment uses both iron and aluminum as projectile material, his equation will be valid for estimating crater depth from both micrometeoroid and orbital debris. The following plots show the crater depth on the CCD due to the impacts from micrometeoroids and orbital debris using Equation 4-3.

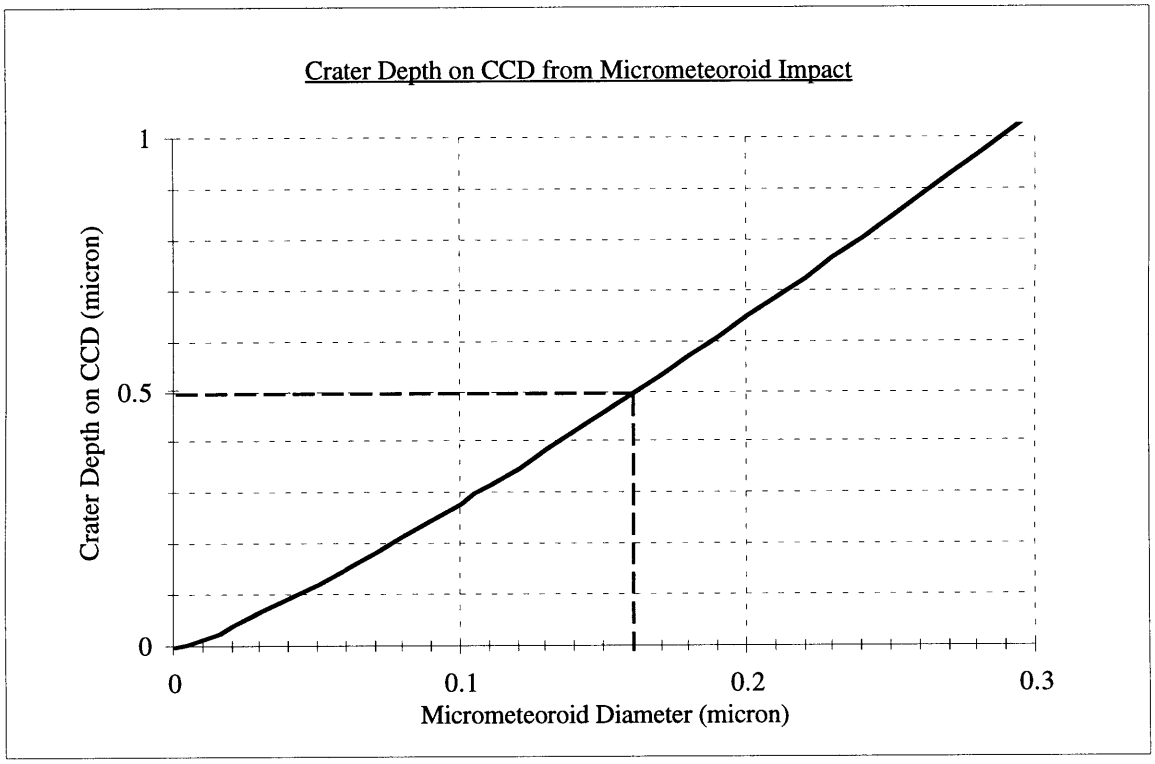

Figure 4-2. Crater Depth on CCD from Micrometeoroid Impact.

The micrometeoroid in the above plot is assumed to have an average velocity of 17 km/s and has the density of iron. The impact is assumed to be normal to the CCD surface. The above plot shows that micrometeoroids about 0.16 μm in diameter will cause about 0.5 μm deep craters on CCD. This indicates that a micrometeoroid with size equal to or larger than about 0.16 μm has a potential to destroy the CCD if there were no shielding. Although the CCDs in SXC are not fully exposed to the space environment because of the Optical Blocking Filter, it will be interesting to see what the failure rate will be if there were no shielding. Using the micrometeoroid flux plot in Figure 2-2, it is estimated that the cumulative flux of micrometeoroids with diameters larger than or equal to 0.16 μm is about 1 impact per year per SXC. Thus, the two CCDs in one SXC will get a crater about 0.5 μm deep from a micrometeoroid impact once a year, or one SXC will face a risk of failing once a year if there were no shielding.

The next plot shows the estimation of crater depth on the CCD due to the orbital debris impacts.

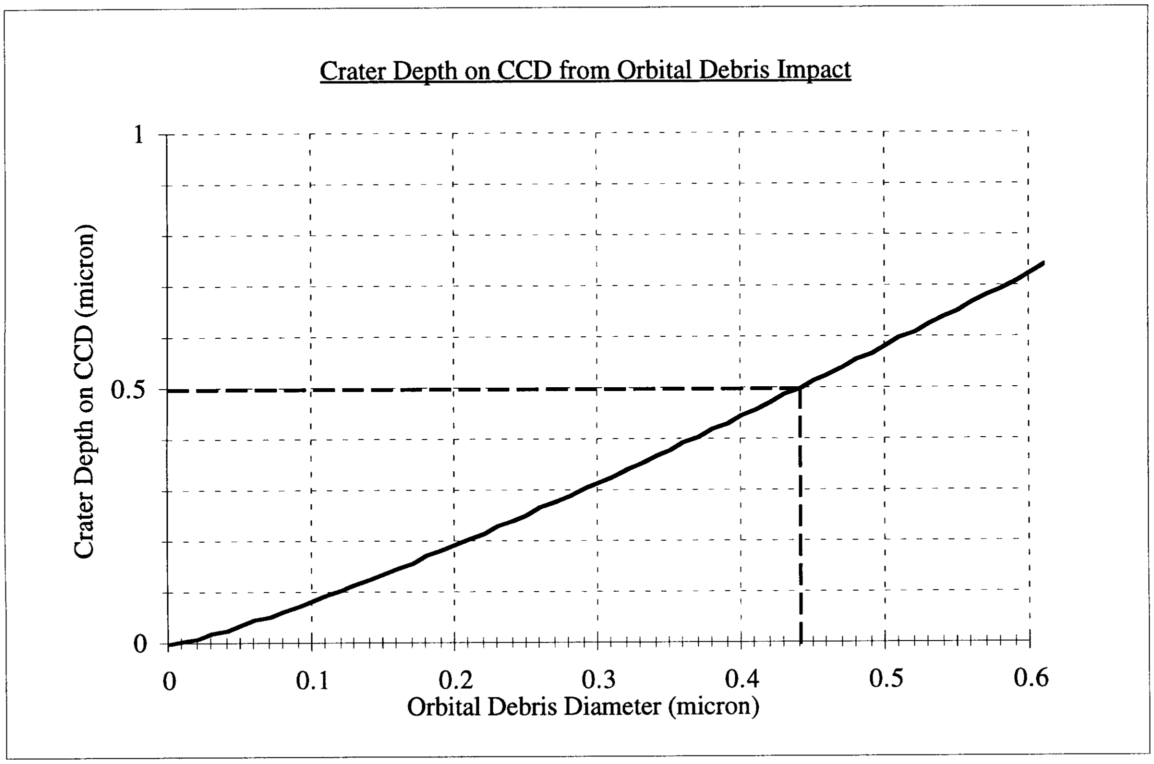

Figure 4-3. Crater Depth on CCD from Orbital Debris Impact.

To estimate crater depth on the CCD, the orbital debris is assumed to have an average velocity of 10.5 km/s and the density of aluminum. The above estimate also assumes normal impacts only. Figure 4-3 shows that a 0.5 μm deep crater on CCD is generated by an impact from orbital debris with diameter of about 0.44 μm. Therefore, orbital debris equal to or larger than about 0.44 μm has a potential to destroy the CCD if there were no shielding. Since ORDEM estimates the flux of orbital debris for diameter larger than 1 μm, the flux for 0.44 μm orbital debris was estimated using linear interpolation shown in the following figure.

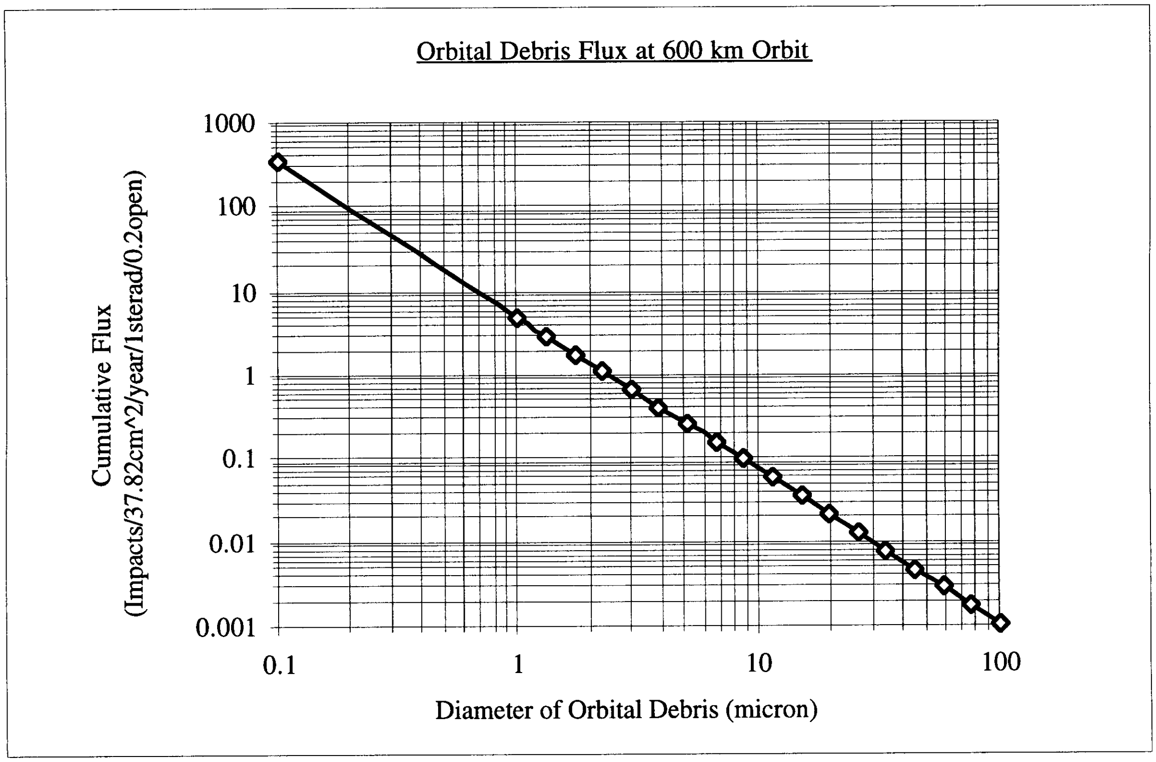

Figure 4-4. Cumulative Flux of Orbital Debris from 0.1 to 100 µm.

Using Figure 4-4, the cumulative flux of orbital debris with diameters larger than or equal to 0.44 µm is about 19 impacts per year per SXC. Therefore, the total impact rate of one SXC due to the impacts from both micrometeoroid and orbital debris is about 20 times a year (1 from micrometeoroid and 19 from orbital debris impacts) if there were no shielding. The above analysis indicates that the SXC will almost surely be destroyed in a short span of time if it were flown in space without any shielding.

Chapter 5

SHIELDING

With the rapidly increasing number of military and civilian satellites in Earth orbit, the problem of protecting these from the micrometeoroid and orbital debris environment is becoming more important. In the near future, shielding against this threat will be an essential part of almost all orbital payload designs. In Chapter 4, it is estimated that there are enough threats from the micrometeoroid and orbital debris impacts to cause failure of SXC if there were no shielding to protect CCDs. The estimated impact rate on one SXC with no shielding is about 20 times a year. As a result, it is concluded that some kind of shielding is needed. The Optical Blocking Filter and Be shielding shown in Figure 1-3 are two shields that will protect the CCD from micrometeoroid and orbital debris impacts. This chapter will explain how each shield works and analyze the effectiveness of each in decreasing the failure rate of SXC.

5.1 Optical Blocking Filter / Whipple Shield

The Optical Blocking Filter (OBF) shown in Figure 1-3 was included in the initial design of SXC even before HETE-2 science team was concerned about the threats from the micrometeoroids and orbital debris. The purpose of OBF is to block off optical and UV lights from entering the SXC. However, the OBF also works as a micrometeoroid and orbital debris shield. Until now, the most effective and popular protection against the micrometeoroid and orbital debris impacts, especially from a weight perspective, is the Whipple bumper shield. The OBF works exactly the same way as a Whipple bumper shield.

When hypervelocity particles impact a Whipple bumper shield, the resulting interaction can be one of two types. If the shielding is thick and the particle does not penetrate, a crater is formed and the particle's momentum is transferred to the shield. The other type of interaction involves shielding thin enough to be penetrated or perforated. In this case, the particle may penetrate and remain essentially intact (such as a bullet passing through a piece of paper); or it may break up or vaporize and generate a diverging cloud of vapor, liquid, and/or solid fragments. The separation between the shield and the target provides space for the debris cloud to spread into a large area, as well as time for vaporization and fragmentation. The following figure shows the concept of the Whipple bumper shield.

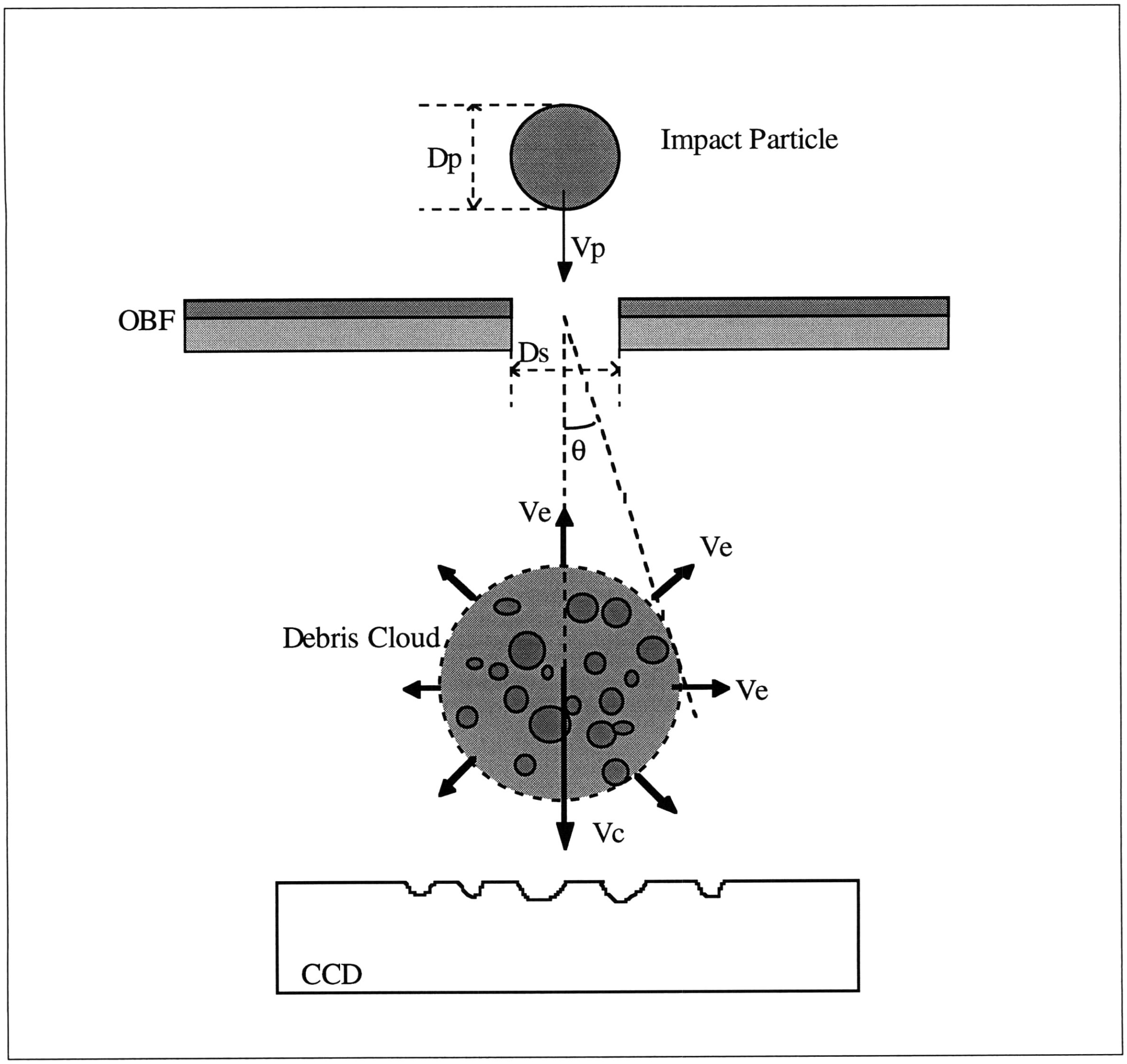

Figure 5-1. Concept of Whipple Bumper Shield using OBF.

The OBF is a layer of thin film consisting of 0.5 μm thick polyimide and 0.15 μm thick aluminum. When a micrometeoroid or a orbital debris hits and penetrates through the OBF, a debris cloud emerges from the back surface of the shield and propagates downward. This debris cloud may be comprised of solid fragments, liquid droplets, vapor, or some combination of these materials, depending on the initial impact kinetic energy. The following is a list of important parameters which will be used in shielding analysis.

m_p = *mass of impact particle*
m_s = *mass of total shielding removed*
$m_{s,Al}$ = *mass of aluminum shielding removed*
$m_{s,poly}$ = *mass of polyimide shielding removed*
D_p = *diameter of impact particle*
D_s = *diameter of shielding removed*
v_p = *velocity of impact particle*
v_c = *velocity of the center of mass of debris cloud*
v_e = *expansion velocity of debris cloud*
T_{Al} = *thickness of aluminum shielding*
T_{poly} = *thickness of polyimide shielding*
ρ_p = *density of impact particle*
ρ_{Al} = *density of aluminum shielding*
ρ_{poly} = *density of polyimide shielding*
$\varepsilon_{vap,p}$ = *vaporization energy of the impact particle*
$\varepsilon_{vap,Al}$ = *vaporization energy of the aluminum shielding*
$\varepsilon_{vap,poly}$ = *vaporization energy of the polyimide shielding*
E_e = *energy needed to vaporize and expand the debris cloud*

5.1.1 Vaporization

Depending on the initial size and the kinetic energy of impacting particles, some of them can be vaporized upon penetration through the OBF. Since a OBF was already manufactured, its thickness is not considered as a variable. This section will discuss the vaporization effect of the OBF and calculate the diameter range of micrometeoroid and orbital debris that will be vaporized upon penetration.

Converting Size to Mass

Using the diameter and density of impact particle, the mass of impact particle is calculated using:

$$m_p = \frac{\pi}{6} D_p{}^3 \rho_p \qquad \textit{Equation 5-1}$$

If D_p and D_s are assumed to be equal, the mass of material removed from shielding is calculated using:

$$m_s = m_{s,Al} + m_{s,poly} = \frac{\pi}{4} \rho_{Al} T_{Al} D_p{}^2 + \frac{\pi}{4} \rho_{poly} T_{poly} D_p{}^2 \qquad \textit{Equation 5-2}$$

Conservation of Momentum

$$m_s v_c = m_p (v_p - v_c) \qquad \textit{Equation 5-3}$$

The Equation 5-3 represents the conservation of momentum which states that the momentum of the impacting particle is transferred to the momentum of shielding removed [Lawrence, 1987]. Although there may be a small loss of momentum due to the force needed to shear off the piece of shield, Lawrence indicates that this loss is very small and ignores for the purpose of calculating the downward velocity of debris cloud. Using Equation 5-3, the downward velocity of the center of mass of debris cloud, Vc, can be calculated as:

$$v_c = \frac{v_p m_p}{(m_p + m_s)} \qquad \textit{Equation 5-4}$$

Conservation of Energy

$$\frac{1}{2}m_p v_p{}^2 = \frac{1}{2}(m_p + m_s)v_c{}^2 + E_e \qquad \text{Equation 5-5}$$

This initial kinetic energy, $\frac{1}{2}m_p v_p{}^2$, is converted to $\frac{1}{2}(m_p + m_s)v_c{}^2$ and E_e. $\frac{1}{2}(m_p + m_s)v_c{}^2$ is the downward kinetic energy of the debris cloud. E_e is the energy for vaporizing the particle and the material removed from shielding, plus the energy for expanding the debris cloud [Lawrence, 1987], and is described in the following equations:

$$E_e = E_{vap} + E_{expand} \qquad \text{Equation 5-6}$$

where $E_{vap} = \varepsilon_{vap,p} m_p + \varepsilon_{vap,Al} m_{s,Al} + \varepsilon_{vap,poly} m_{s,poly}$ *Equation 5-7*

$$E_{expand} = \frac{1}{2}(m_p + m_s)v_e{}^2 \qquad \text{Equation 5-8}$$

Equation 5-8 assumes the debris cloud is a shell, with expanding velocity, *Ve*. When hypervelocity particles impact and penetrate relatively thin material layers, most observers have noted that the resulting debris cloud takes the form of an expanding shell [Gehring, 1970]. Although it is not necessary to assume this shape, the analysis is more convenient if I assume that the debris cloud is a shell and the expanding velocities for all fragments are the same.

$$E_e = \varepsilon_{vap,p} m_p + \varepsilon_{vap,Al} m_{s,Al} + \varepsilon_{vap,poly} m_{s,poly} + \frac{1}{2}(m_p + m_s)v_e{}^2 \qquad \text{Equation 5-9}$$

Combining Equation 5-4 and Equation 5-5, E_e can be expressed in terms of the initial kinetic energy as:

$$E_e = \frac{1}{2} m_p v_p^2 \left(\frac{m_s}{m_p + m_s} \right) \qquad \textit{Equation 5-10}$$

Setting Equation 5-10 equal to Equation 5-9 generates the following relationships.

$$\frac{1}{2} m_p v_p^2 \left(\frac{m_s}{m_p + m_s} \right) = \varepsilon_{vap,p} m_p + \varepsilon_{vap,Al} m_{s,Al} + \varepsilon_{vap,poly} m_{s,poly} + \frac{1}{2} (m_p + m_s) v_e^2$$

or

$$\frac{1}{2} m_p v_p^2 \left(\frac{m_s}{m_p + m_s} \right) \geq \varepsilon_{vap,p} m_p + \varepsilon_{vap,Al} m_{s,Al} + \varepsilon_{vap,poly} m_{s,poly} \qquad \textit{Equation 5-11}$$

Equation 5-11 is the necessary condition for vaporization of the impact particle and removed shielding material. By converting Equation 5-11 to an equality and solving for v_p, the necessary minimum impact velocity required for vaporization as function of size of the impact particle can be calculated:

$$\frac{1}{2} m_p v_p^2 \left(\frac{m_s}{m_p + m_s} \right) = \varepsilon_{vap,p} m_p + \varepsilon_{vap,Al} m_{s,Al} + \varepsilon_{vap,poly} m_{s,poly}$$

Since $m_s = m_{s,Al} + m_{s,poly}$,

$$v_p = \sqrt{ \frac{2}{m_p} \left(\frac{m_p + m_{s,Al} + m_{s,poly}}{m_{s,Al} + m_{s,poly}} \right) \left(\varepsilon_{vap,p} m_p + \varepsilon_{vap,Al} m_{s,Al} + \varepsilon_{vap,poly} m_{s,poly} \right) } \qquad \textit{Equation 5-12}$$

where $m_p = \frac{\pi}{6} D_p^3 \rho_p$, $m_{s,Al} = \frac{\pi}{4} \rho_{Al} T_{Al} D_p^2$, $m_{s,poly} = \frac{\pi}{4} \rho_{poly} T_{poly} D_p^2$

Using the following data,

$T_{Al} = 1500 \times 10^{-10} (m)$ (*shielding thickness is not a variable.)

$T_{poly} = 5000 \times 10^{-10} (m)$ (*shielding thickness is not a variable.)

$\rho_{Al} = 2.7\ (g/cm^3)$

$\rho_{poly} = 1.06\ (g/cm^3)$

$\rho_{iron} = 7.87\ (g/cm^3)$

$\varepsilon_{vap,Al} = 12\ (KJ/g)$

$\varepsilon_{vap,poly} = 4.4\ (KJ/g)$

$\varepsilon_{vap,iron} = 8.7\ (KJ/g)$

v_p, the minimum required impact velocity for vaporization, is plotted as function of D_p, the size of initial particles, in the following figures.

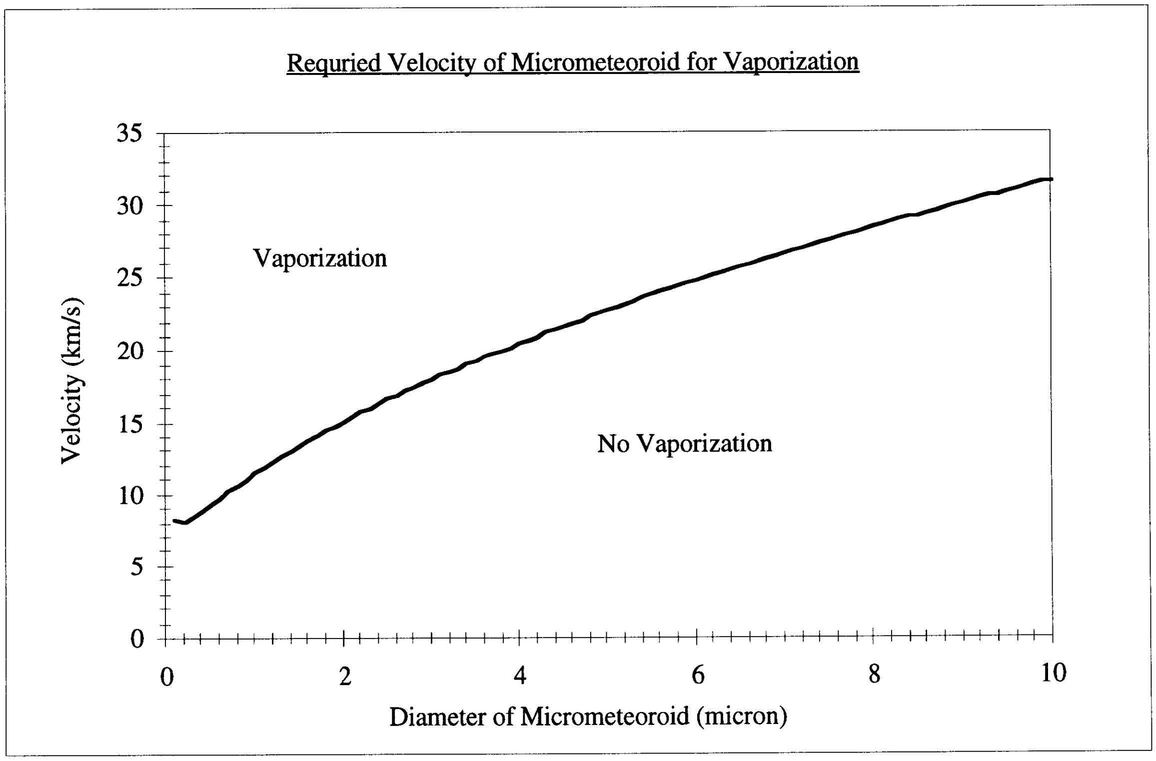

Figure 5-2. Minimum Required Velocity of Micrometeoroid for Vaporization.

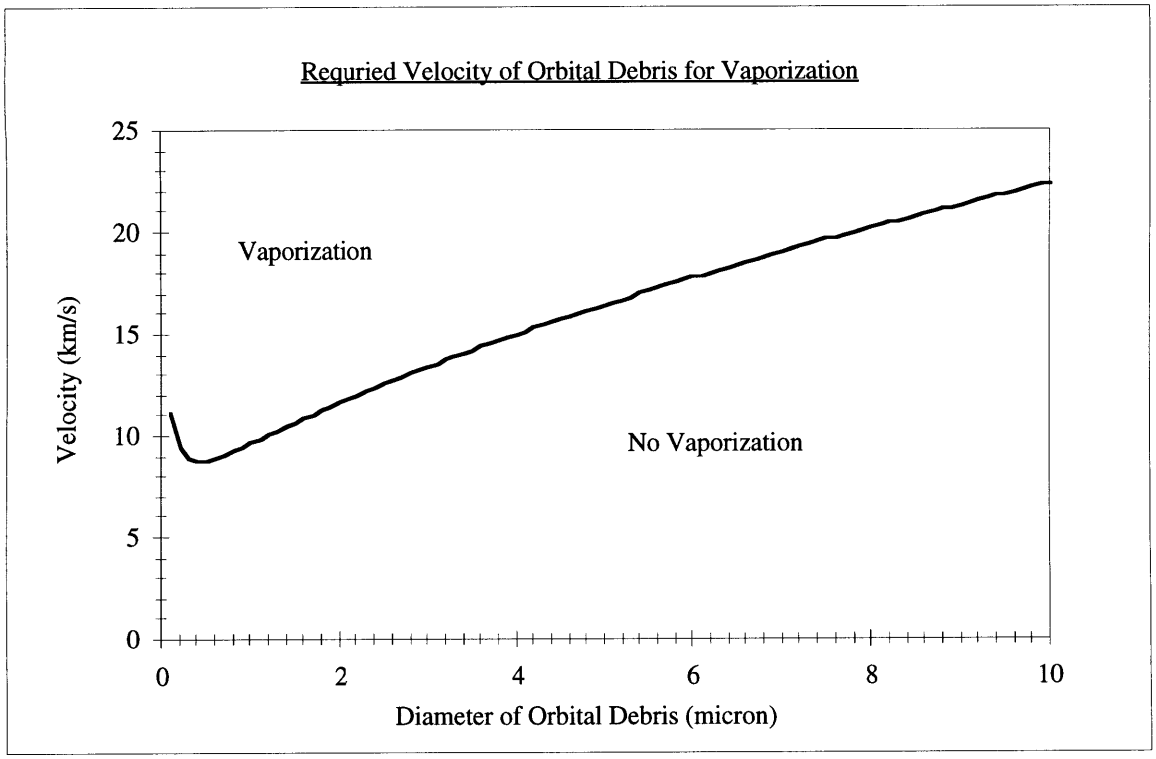

Figure 5-3. Minimum Required Velocity of Orbital Debris for Vaporization.

The plot in Figure 5-2 shows the possible region of vaporization when a micrometeoroid penetrates the OBF. The region above the limiting velocity line is where vaporization can occur; and the region below the limiting velocity line is where vaporization can not occur. Figure 5-3 shows the vaporization region for orbital debris.

In order for vaporization to occur, the impact particle has to first penetrate through the shielding. Therefore, the probable vaporization region should lie inside the penetration region where particles penetrate through the OBF. Grun's penetration equation is converted into velocity necessary to penetrate the OBF shielding as a function of diameter of the particle, as shown in following equation.

$$T = \frac{0.772}{\varepsilon^{0.06} \rho_s^{0.5}} D_p^{1.2} \rho_p^{0.73} v_p^{0.88}$$

$$v_p = \left(\frac{\varepsilon^{0.06} \rho_s^{0.5} T}{0.772 D_p^{1.2} \rho_p^{0.73}} \right)^{\frac{1}{0.88}} \qquad \textit{Equation 5 - 13}$$

where

$T = thickness(cm)$

$D_p = size\ of\ impact\ particle(cm)$

$\rho_p = density\ of\ particle(g/cm^3)$

$\rho_t = density\ of\ target(g/cm^3)$

$\varepsilon = ductility\ constant$

$V_p = velocity\ of\ particle(km/s)$

The limiting penetration velocity from Equation 5-13 is plotted along with the limiting vaporization velocity from Equation 5-12 in the following plots.

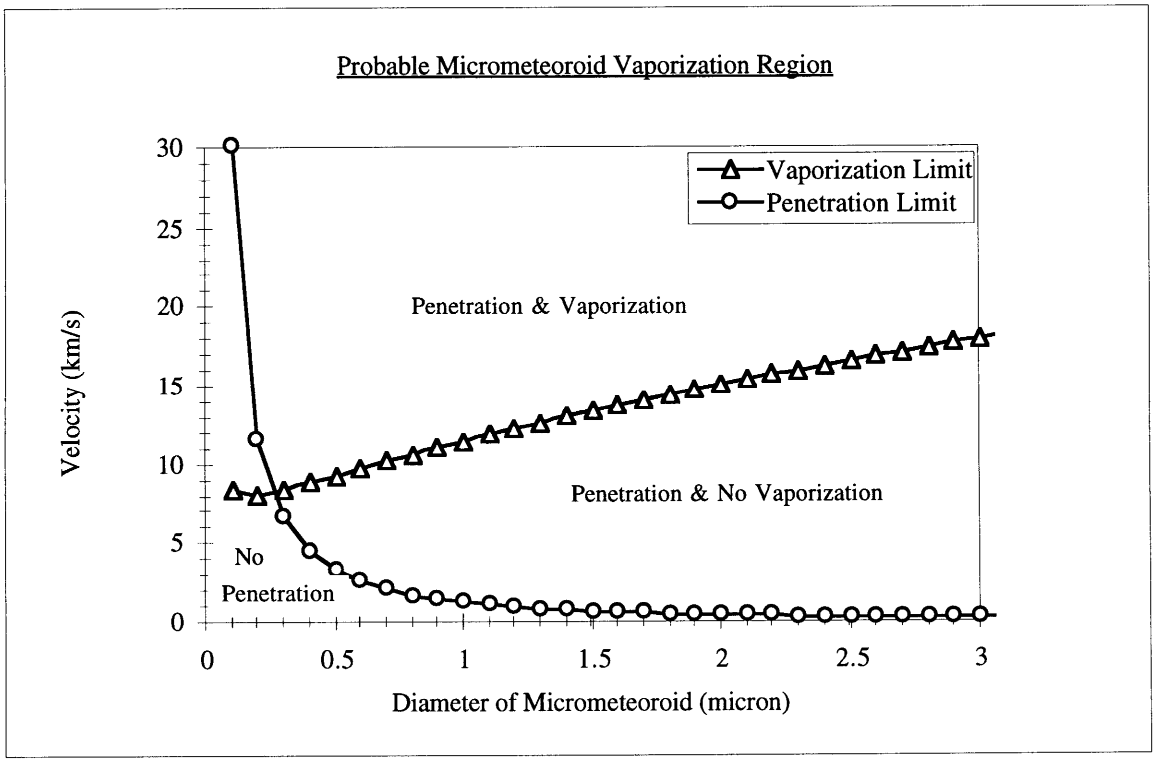

Figure 5-4. Probable Micrometeoroid Vaporization Region.

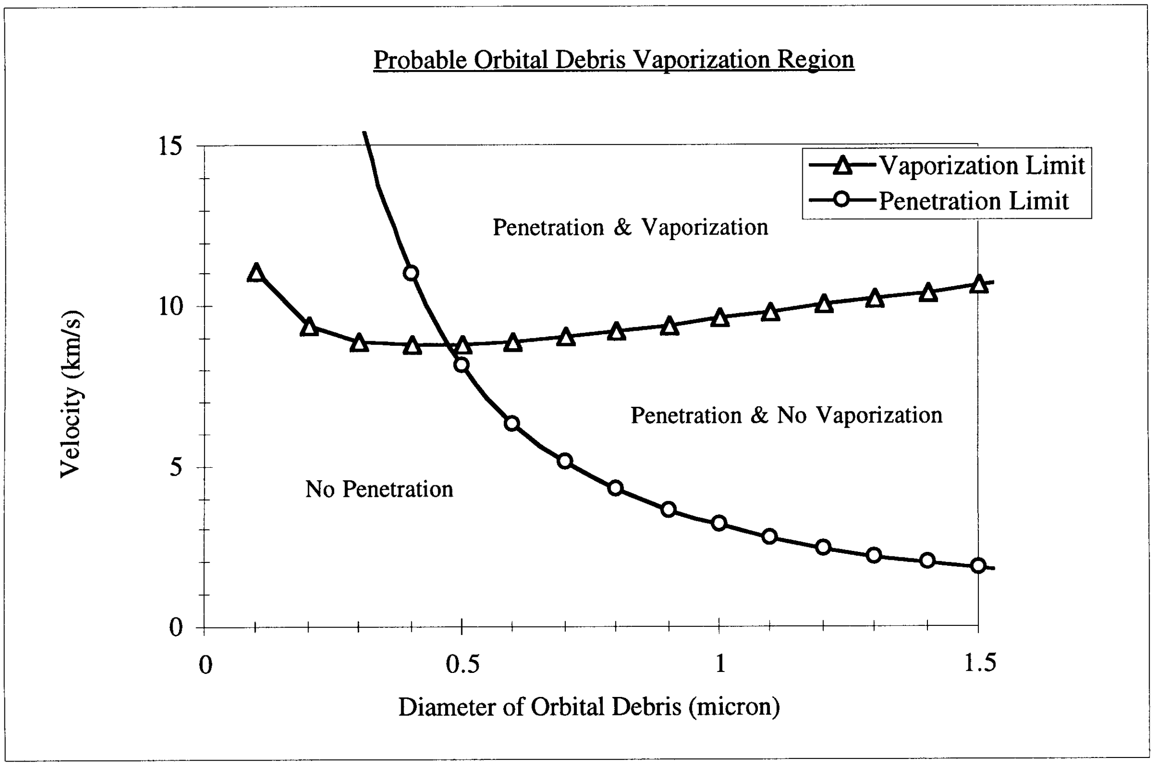

Figure 5-5. Probable Orbital Debris Vaporization Region.

The left side of the penetration limit line is the region where particles can not penetrate the OBF. If we assume initial impacting particles have an average velocities (17 km/s for micrometeoroids and 10.5 km/s for orbital debris), then the diameter range of the impacting particles that will be vaporized upon penetration through the OBF can be estimated:

States	micrometeoroid	orbital debris
no penetration	d < 0.2μm	d < 0.4 μm
vaporization	0.2μm < d < 2.5 μm	0.4μm < d < 1.4μm
no vaporization	d > 2.5μm	d > 1.4μm

Table 5-1. Range of Particles for Various States.

The above table shows that the OBF will be able to block off micrometeoroids up to 0.2 μm and orbital debris up to 0.4 μm. In other words, those particles will not be able to penetrate through OBF unless they have velocity higher than the average velocity. On the other hand, micrometeoroids between 0.2μm and 2.5μm and orbital debris between 0.4 μm and 1.4 μm have enough kinetic energy to penetrate through OBF and be vaporized after penetration if they impact the OBF with an average velocity of 17 km/s for micrometeoroids and 10.5 km/s for orbital debris. If the micrometeoroid is larger than 2.5 μm and orbital debris is larger than 1.4 μm, they will not be vaporized although they will penetrate through OBF and enter inside the SXC. The impact kinetic energy of those particles is not large enough to vaporize the impacting particle and the material removed from shielding. In conclusion, the above analysis shows that the OBF will be able to protect the CCDs from micrometeoroid smaller than 2.5 μm and orbital debris smaller than 1.4 μm by either blocking them off, so they can not penetrate through OBF or by vaporizing them after the penetration.

If the penetrated particles and the material removed from shielding are not vaporized, some of them will be fragmented into smaller particles which may not cause a critical damage to the CCDs. The next section will explain the fragmentation effects of the OBF.

5.1.2 Fragmentation

As discussed in the above section, vaporization occurs if the impacting particle hits the OBF with kinetic energy higher than the energy required to vaporize it, plus the removed portion of shielding. If the kinetic energy is less than the vaporization energy, then the penetrated materials can be fragmented or stay intact. When the impacting particle has just enough kinetic energy to penetrate through OBF, but does not have any extra energy left for breaking up or vaporizing itself, then the impacting particle will stay intact. Fragmentation occurs if there is extra energy to break up materials after penetrating through OBF. The size of fragmented particles range from small liquid droplets to large chunks of solid material. Some of the fragmented particles may be too small to cause craters that are deep enough to cause electrical shorts on CCDs. However, some of them may still be large enough to cause critical damage on a CCD. Therefore, it is important to find out the impact rate on a CCD due to the fragmented particles after the penetration. The following analysis will show how to estimate the damage caused by the fragmented particles.

5.1.2.1 Relationship Between the Average Fragmented Particle and Ee.

As shown in the Equation 5-6, Ee is the energy for breaking up particles and expanding the debris cloud. If Ee reaches Evap, the vaporization energy, then the penetrated material will start to vaporize. If Ee is smaller than Evap, then the penetrated materials will be fragmented or stay intact instead of vaporizing. If Ee is not equal to Evap but still very close to Evap, then the size of fragmented particles will be small. If Ee is much less than Evap, then it will result in larger fragmented particles. In other words, more breaking up energy will generate smaller fragmented particles. The size of fragmented particles decreases as the Ee increases. Once Ee reaches Evap, then the size of fragmented particles will become zero, which means vaporization. Therefore, once a relationship between Avg Size/Initial Size and Ee/Evap is known, the average size of fragmented particles (Avg Size) as a function of Ee can be estimated. Unfortunately, there is no single equation that describes the above relationship. An alternative way is to use the data from similar experiments which measure the average size of fragmented particles. The fragmentation experiment by M.E. Kipp et. al in 1993 measured the average size of fragments after a particle penetrates through a layer of film. They have performed a series of high-velocity experiments specifically designed to examine the fragmentation of the projectile during penetration. For all tests, high-strength and well characterized steel spheres (6.35 mm diameter) were launched with a two-stage light-gas gun to velocities in the range of 3 to 5 km/s normal to the target film. The film used is PMMA (polymethyl-methacrylate) with a thickness of 0.6 to 11 mm. Multiple flash radiography diagnostics and recovery techniques were used to assess the size of the fragments. The experimental data are summarized in the following table [Kipp et al., 1993].

Test #	Diameter of Impact Particle (m)	Thickness of Film (m)	Impact Velocity (m/s)	Average Fragment Size (m)
1	0.00635	0.00328	4460	0.00067
2	0.00635	0.00328	4460	0.00116
3	0.00635	0.00174	4450	0.0011
4	0.00635	0.00174	4700	0.00095
5	0.00635	0.00338	4570	0.00072
6	0.00635	0.00328	3460	0.00144
7	0.00635	0.00344	4160	0.00074
8	0.00635	0.00149	3950	0.0012
9	0.00635	0.00151	3460	0.00166
10	0.00635	0.00537	4430	0.00096
11	0.00635	0.00536	4060	0.00114
12	0.00635	0.00538	3310	0.00204
13	0.00635	0.00537	4080	0.001
14	0.00635	0.00325	4520	0.00097
15	0.00635	0.00471	4430	0.001
16	0.00635	0.00539	4610	0.00118
17	0.00635	0.00475	4040	0.0009
18	0.00635	0.00478	3750	0.00102
19	0.00635	0.00099	4700	0.00122
20	0.00635	0.01123	4060	0.00077
21	0.00635	0.00947	4030	0.00101

Table 5-2. Experimental Data for Average Fragmented Particles.

Above experiment is carried out using macroscopic impact particles and targets. Another impact experiment by Walsh et. al suggests that macroscopic impacts and microscopic impacts are essentially identical. Therefore, a relationship obtained using macroscopic impact data can be applied for microscopic impacts. Using the above data, Ee and Evap are calculated for each test by Equations 5-7 and 5-10. The relationship between Ee/Evap and Avg Size/Initial Size is plotted in the following figure.

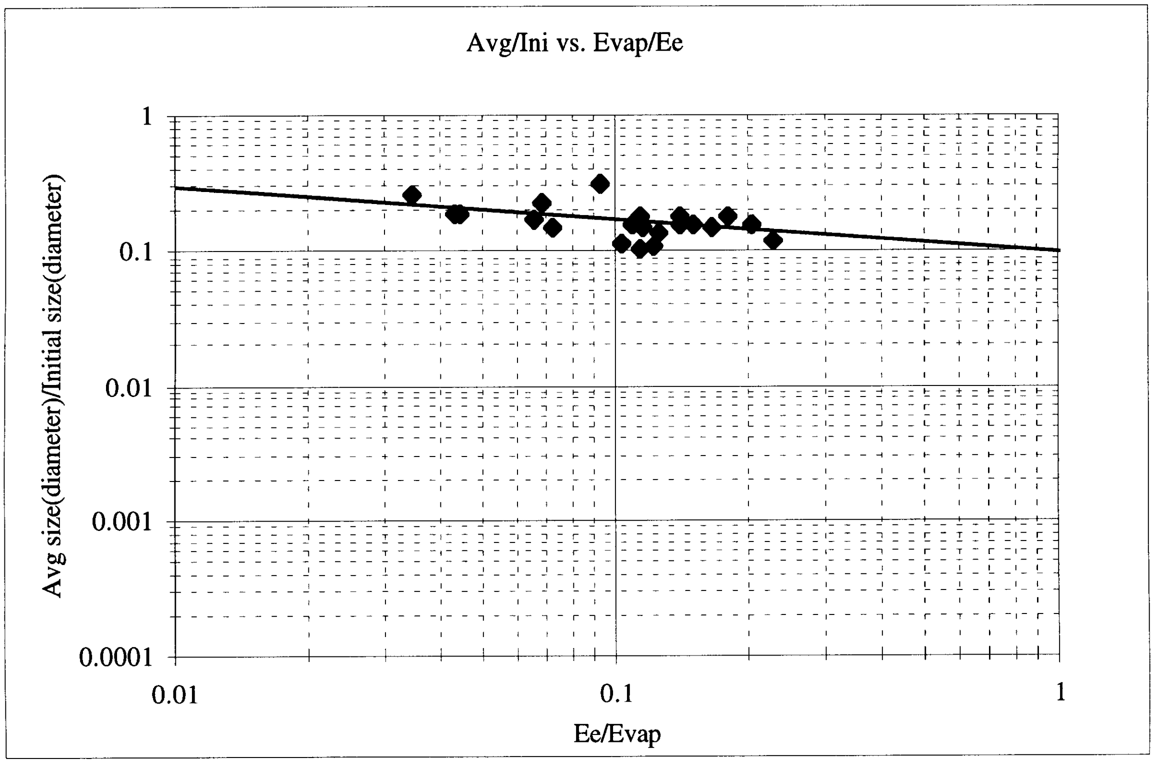

Figure 5-6. Relationship between Ee/Evap and Average Size of Fragmented Particles/Initial Size.

The above data follows a linear relationship in log-log scale, indicating it follows a power law. Using the above relationship, the average size of fragments can be estimated as a function of calculated Ee/Evap for micrometeoroid and orbital debris impacts. The average size of fragments will be used in the Poisson distribution in later section. The next section will discuss how to estimate the damage on CCD caused by the fragments.

5.1.2.2 Damage Caused by the Fragments.

Step 1: Ee/Evap vs. Initial Impact Particle Size.

If the diameter of the impacting particle and the diameter of the portion removed from shield are assumed to be equal, then the mass of the impacting particle and material removed from the shield can be calculated as a function of the diameter of the impacting particle. Then, using Equation 5-10 and Equation 5-7,

$$E_e = \frac{1}{2} m_p v_p^2 \left(\frac{m_s}{m_p + m_s} \right) \text{ and}$$

$$E_{vap} = \varepsilon_{vap,p} m_p + \varepsilon_{vap,Al} m_{s,Al} + \varepsilon_{vap,poly} m_{s,poly}$$

Ee/Evap can be calculated. The ratio Ee/Evap is plotted against the initial size of orbital debris and micrometeoroids in the following plots.

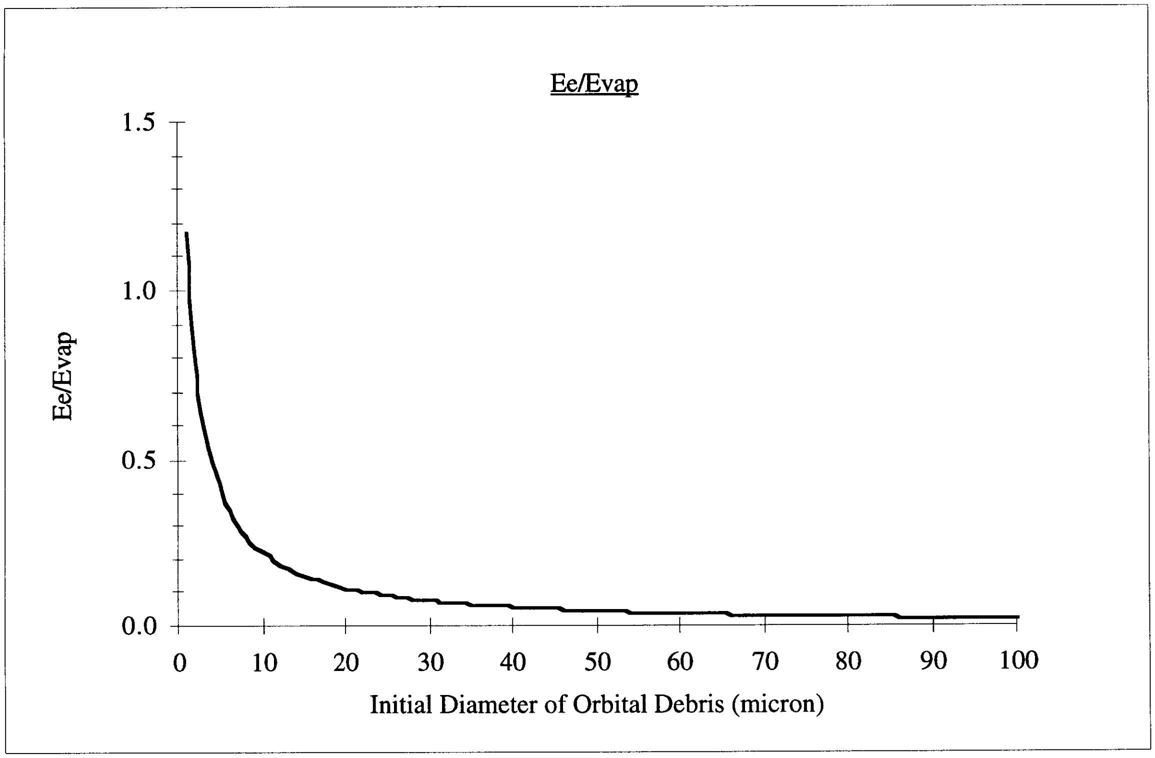

Figure 5-7. Ee/Evap vs. Diameter of Orbital Debris.

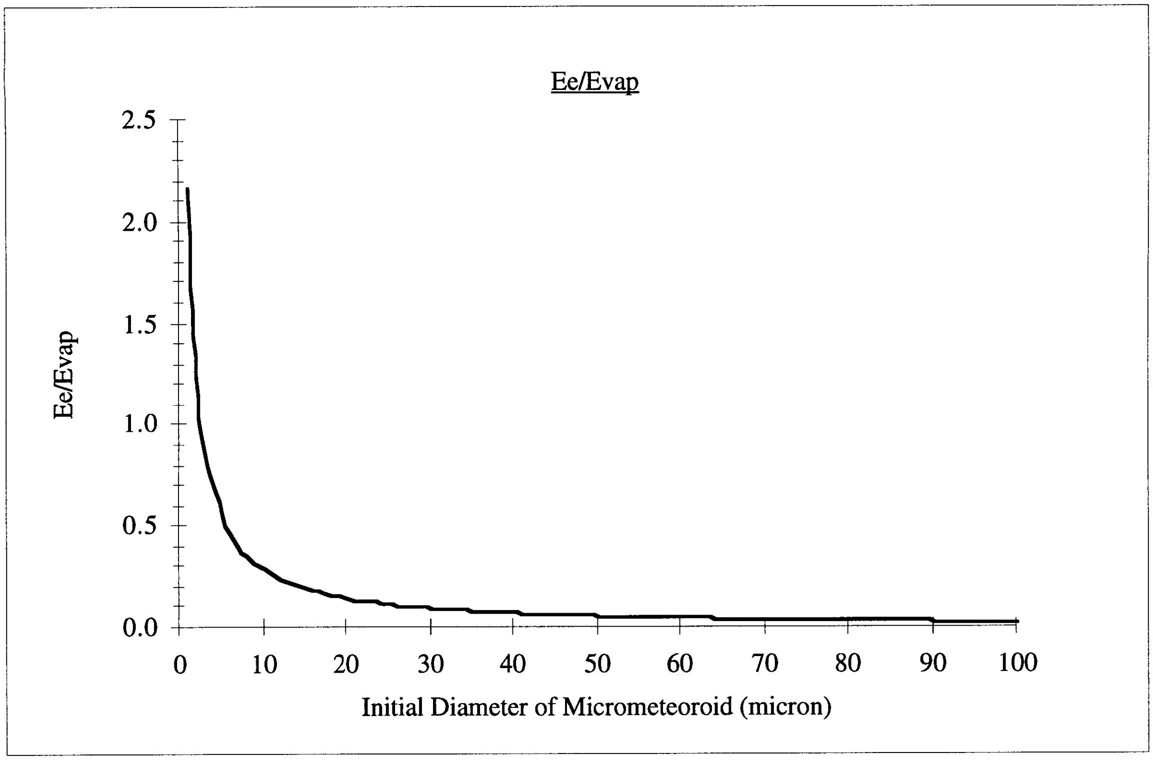

Figure 5-8. Ee/Evap Vs. Diameter of Micrometeoroid.

The above plots show that as the initial diameter of impacting particle increases, Ee/Evap decreases. When a large particle penetrates through the OBF, it will not be fragmented easily because Ee/Evap is small. When a small particle penetrates through the OBF and if Ee/Evap is greater than 1, the impacting particle will be vaporized. In Section 5.1.1, it was estimated that orbital debris smaller than 1.4 μm would be vaporized when it penetrates the OBF. The above plot in Figure 5-7 also indicates the ratio of Ee/Evap is greater than 1 which is the necessary condition for vaporization, for orbital debris size smaller than 1.4 μm. Figure 5-8 shows that micrometeoroids smaller than 2.5 μm will be vaporized.

Step 2: AvgSize/InitialSize vs. Initial Impact Particle Size.

In this step, Ee/Evap in Figure 5-7 and 5-8 are converted into a ratio of the average fragment size over the initial particle size (Avg Size/Initial Size) using the plot in Figure 5-6. The ratio of Avg Size/Initial Size is plotted against the size of initial impacting particles in the following figures.

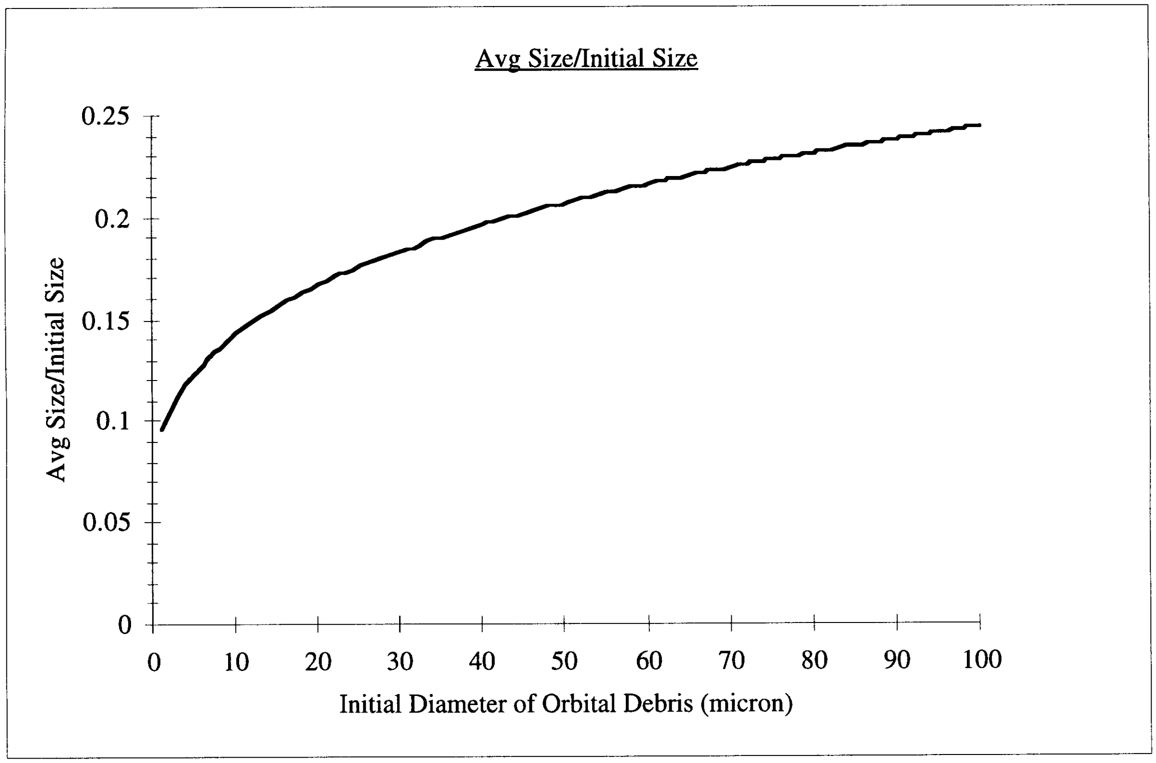

Figure 5-9. The Ratio of Avg Fragmented Size/Initial Size for Orbital Debris.

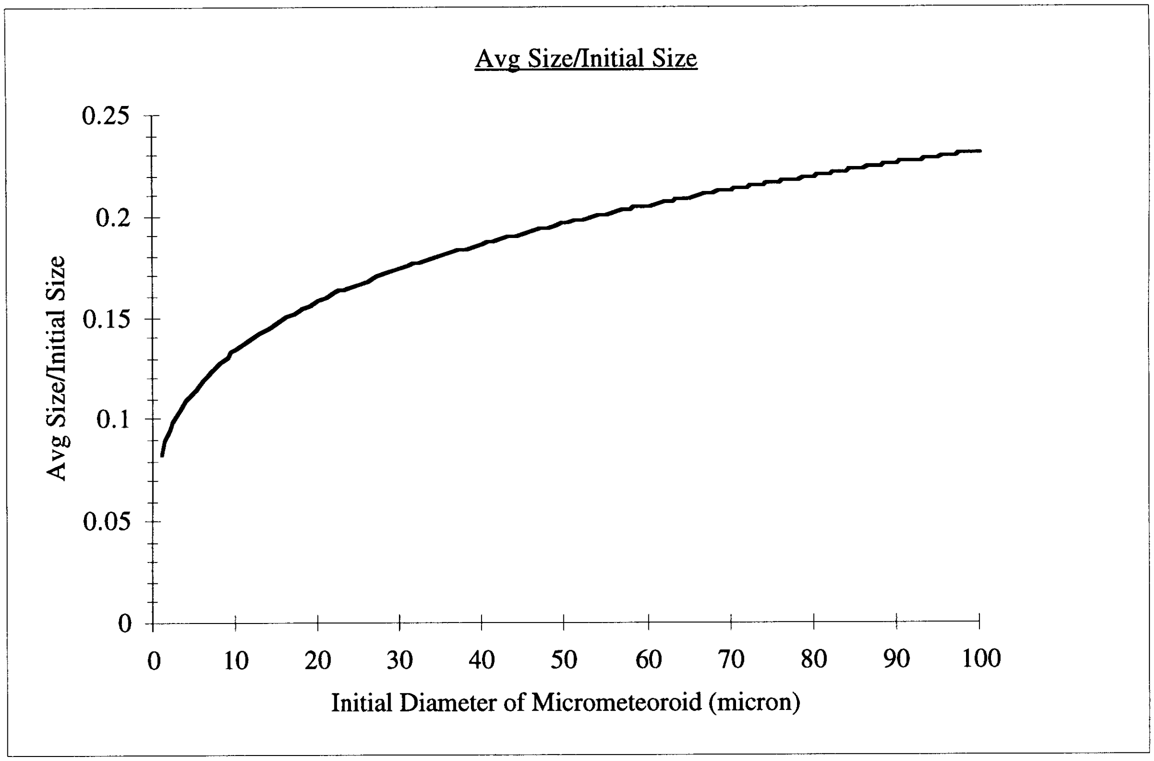

Figure 5-10. The Ratio of Avg Fragmented Size/Initial Size for Micrometeoroid..

Step 3: Average Fragmented Particle Size vs. Initial Impacting Particle Size.

The ratio of average fragment size over initial particle size is multiplied by the corresponding initial particle size to get the average fragment size:

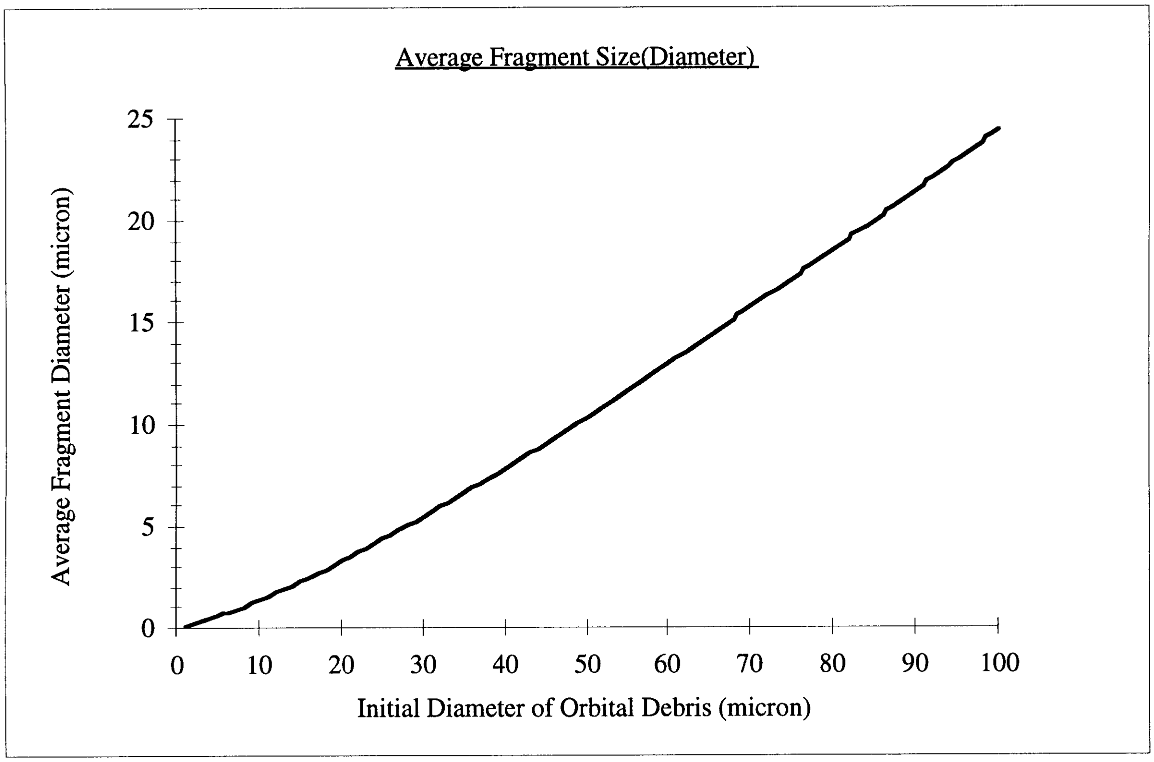

Figure 5-11. Average Fragment Diameter for Orbital Debris.

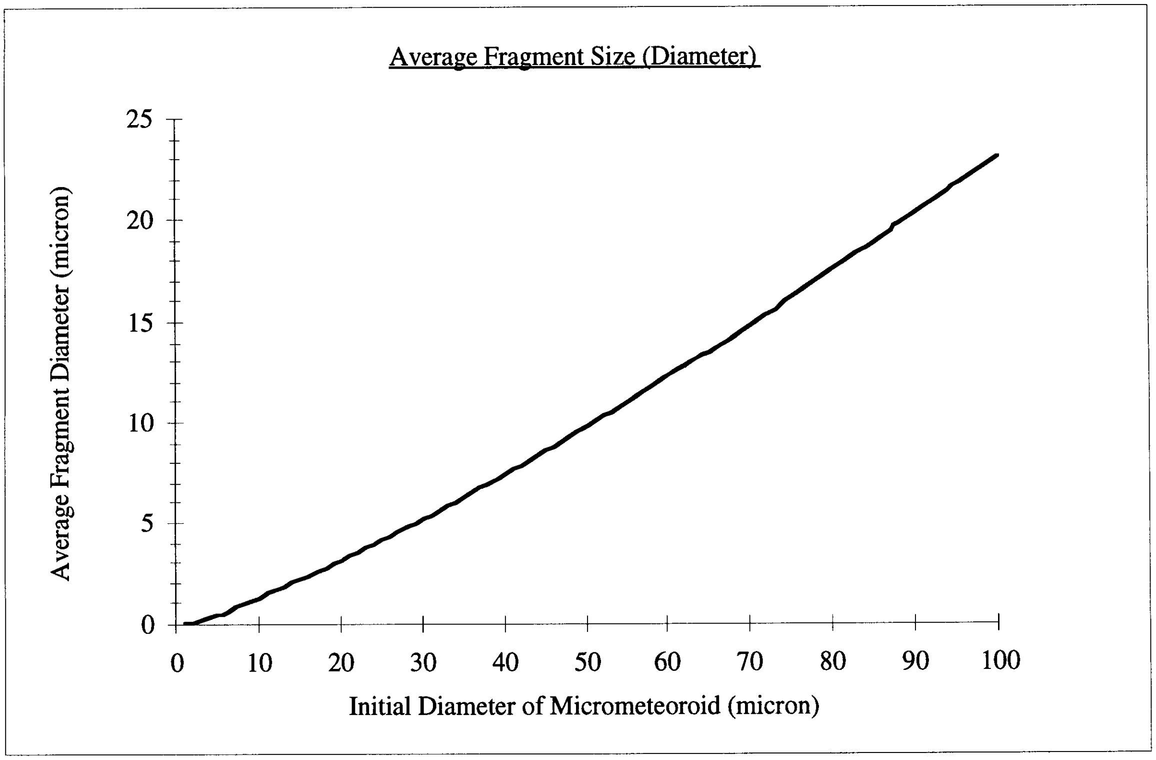

Figure 5-12. Average Fragment Diameter for Micrometeoroid.

Step 4: Velocity after Penetrating OBF.

To estimate the crater depth caused by the fragments, their new reduced velocity after penetration must be estimated. Assuming conservation of momentum, the downward velocity of fragments after penetrating through the OBF can be calculated using the Equation 5-4.

$$v_c = \frac{v_p m_p}{(m_p + m_s)}$$

The new downward velocity of fragmented particles, Vc is less than the initial impact velocity and assumed to be the same for all fragments. The initial velocity, Vp, was assumed to be 17 km/s for micrometeoroids and 10.5 km/s for orbital debris. Using the above equation, the Vc is plotted as a function of initial size of the micrometeoroids and orbital debris in the following figures.

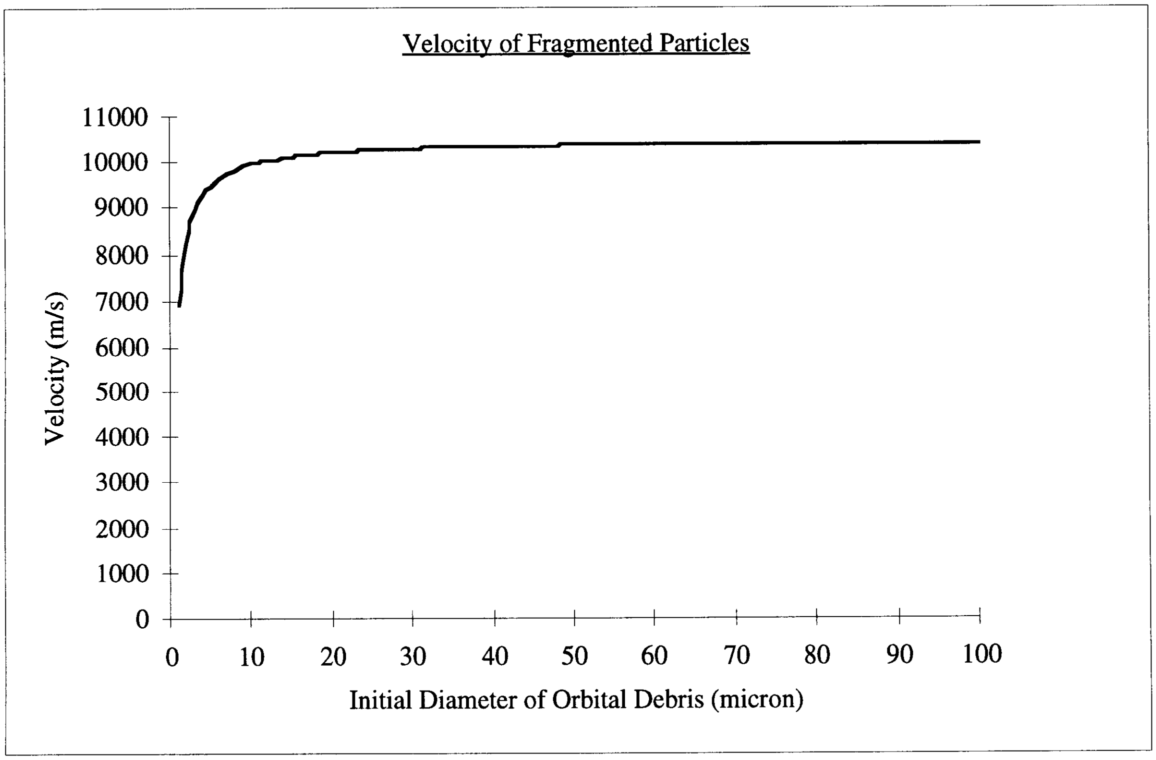

Figure 5-13. Velocity of Fragmented Particles for Orbital Debris.

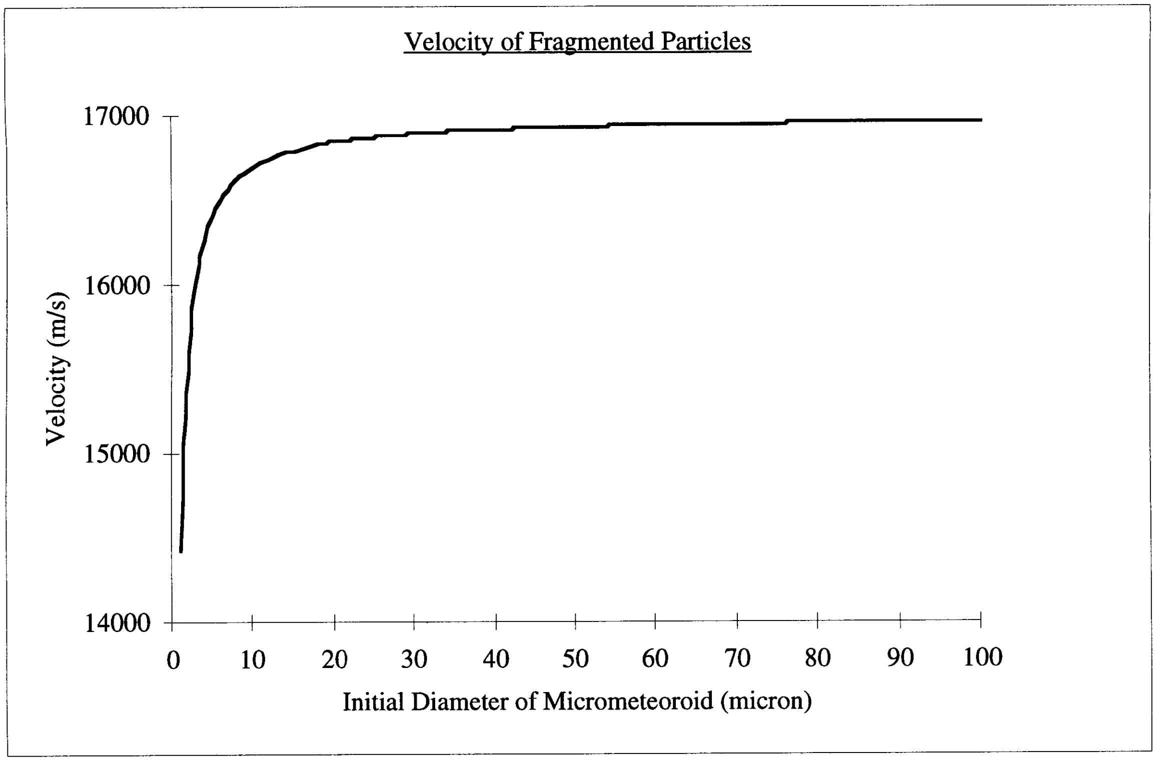

Figure 5-14. Velocity of Fragmented Particles for Micrometeoroid.

The above plots show that as the size of initial particle gets large, Vc, the new downward velocity of the fragmented particles is approaching Vp, the initial velocity of the impacting particle. This indicates that the effect of OBF shielding becomes smaller as the size of impact particle gets larger.

Step 5: Fragments Probability Distribution.

According to the statistical considerations indicated by Grady and Kipp in 1985, the fragment size distribution should be determined about the mean fragment size. The form of the distribution is obtained by assuming that fragmented particles are Poisson-distributed [Grady and Kipp, 1985]. This leads to a probability distribution of finding a fragment of mass, μ, within a tolerance, dμ, given by

$$dP(\mu) = \frac{1}{\mu_a} e^{-\frac{\mu}{\mu_a}} d\mu \qquad \textit{Equation 5-14}$$

where μ_a is the average or mean fragment mass. Converting mass into size, S, the following relationship is obtained

$$dP(S) = \frac{3S^2}{S_a^{\,3}} e^{-\left(\frac{S}{S_a}\right)^3} dS \qquad \textit{Equation 5-15}$$

where S_a is the size of average fragmented particle. For example, an initial orbital debris with 5 micron in diameter generates fragmented particles with average diameter of 0.62 micron according to Figure 5-11. The fragments size distribution for this example can be plotted using Equation 5-15:

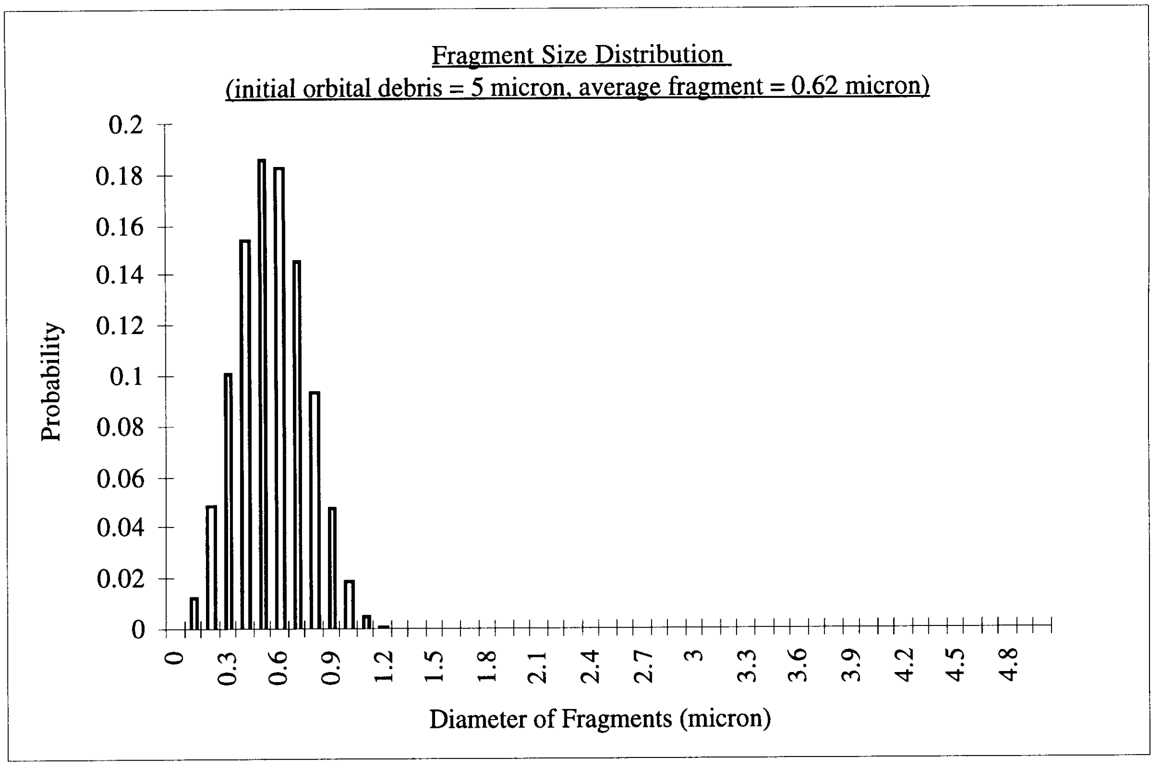

Figure 5-15. Fragment Size Distribution for Initial Orbital Debris with 5 μm in Diameter.

Integrating Equation 5-14 from 0 to μ will generate the cumulative probability distribution, $P(\mu)$

$$\int_0^{\mu} dP(\mu)d\mu = P(\mu) = 1 - e^{-\mu/\mu_a}$$

since $\frac{\mu}{\mu_a} = \left(\frac{S}{S_a}\right)^3$

$$P(S) = 1 - e^{-\left(\frac{S}{S_a}\right)^3} \qquad \textit{Equation 5-16}$$

The above equation 5-16 is the cumulative probability of fragmented particles with sizes equal to and smaller than that size. The cumulative probability of fragmented particles with sizes equal to and larger than that size, $P'(S)$:

$$P'(S) = 1 - P(S) = e^{-\left(\frac{S}{S_a}\right)^3}$$ *Equation 5-17*

Using the same example, in which a 5 micron sized initial particle generates fragmented particles with average diameter of 0.62 micron, the cumulative probability , $P'(S)$, is plotted in the following figure.

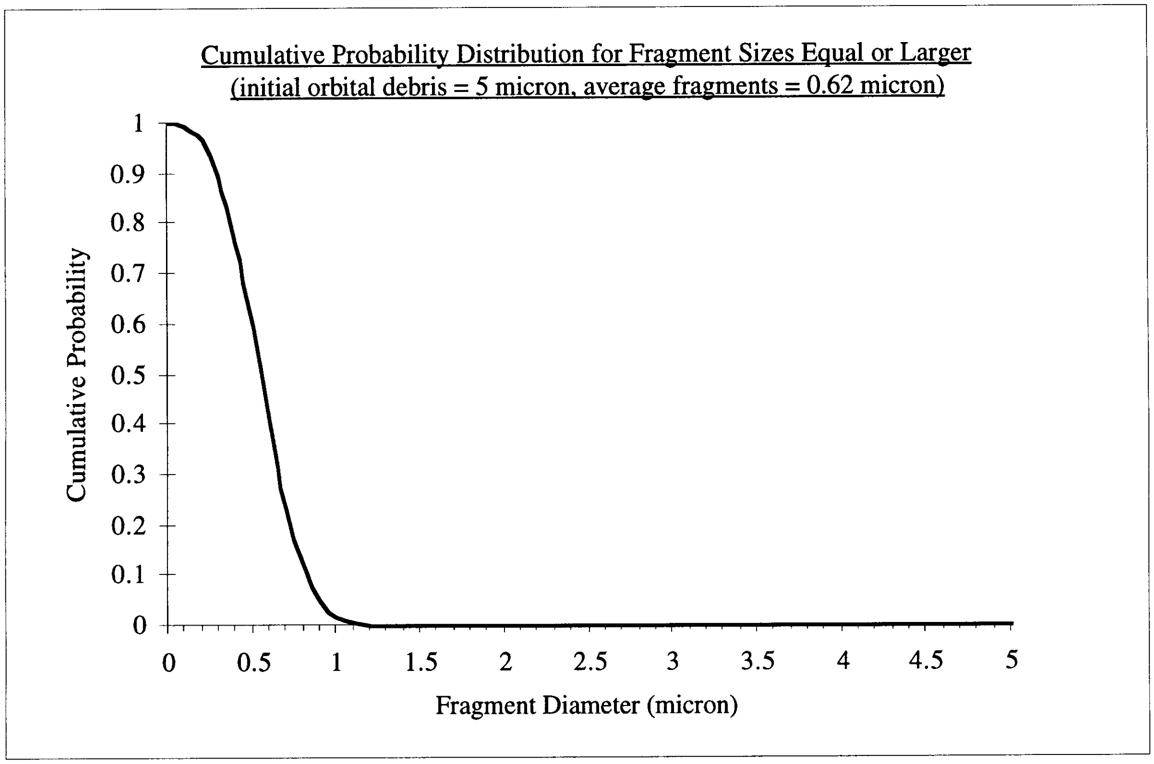

Figure 5-16. Cumulative Probability Distribution for Initial Orbital Debris with 5 μm in Diameter.

Using the downward velocity of fragments calculated in Step 4, the fragment diameter in above figure can be converted into the crater depth on CCD by Grun's equation. The following figures show the cumulative probability distribution as a function of crater depth on a CCD.

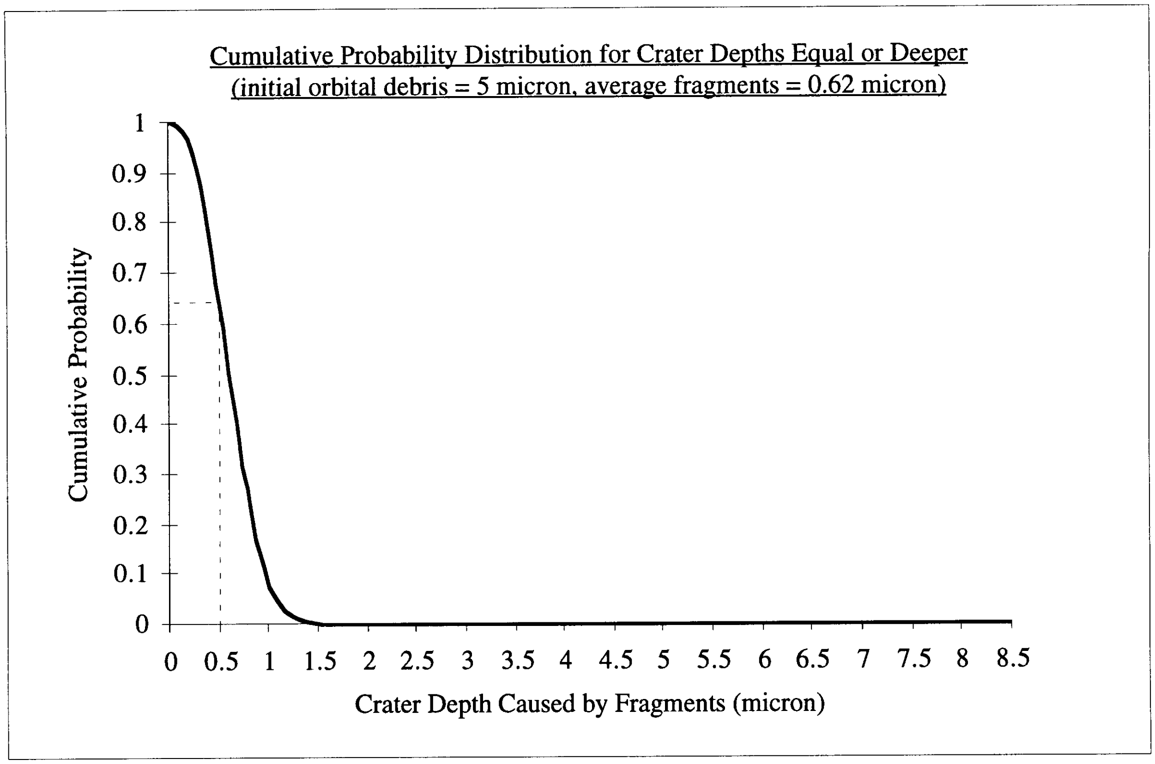

Figure 5-17. Cumulative Probability Distribution vs. Crater Depth on a CCD.

According to the dashed line in the above plot, there is about 64 % chance that the fragmented particles will cause a 0.5 micron deep or deeper crater on a CCD. In summary, an initial orbital debris with 5 micron in diameter penetrates through the OBF and generates fragments with various diameters. Out of all the fragments, 64% of them will cause 0.5 micron deep or deeper damage on a CCD. The rest of smaller fragments will cause less than 0.5 micron deep damage on a CCD. Using the above example, the cumulative probability, P(s), of each impacting particle which will cause 0.5 micron deep or deeper crater on CCD after penetrating through the OBF is plotted as a function of the initial impacting particle:

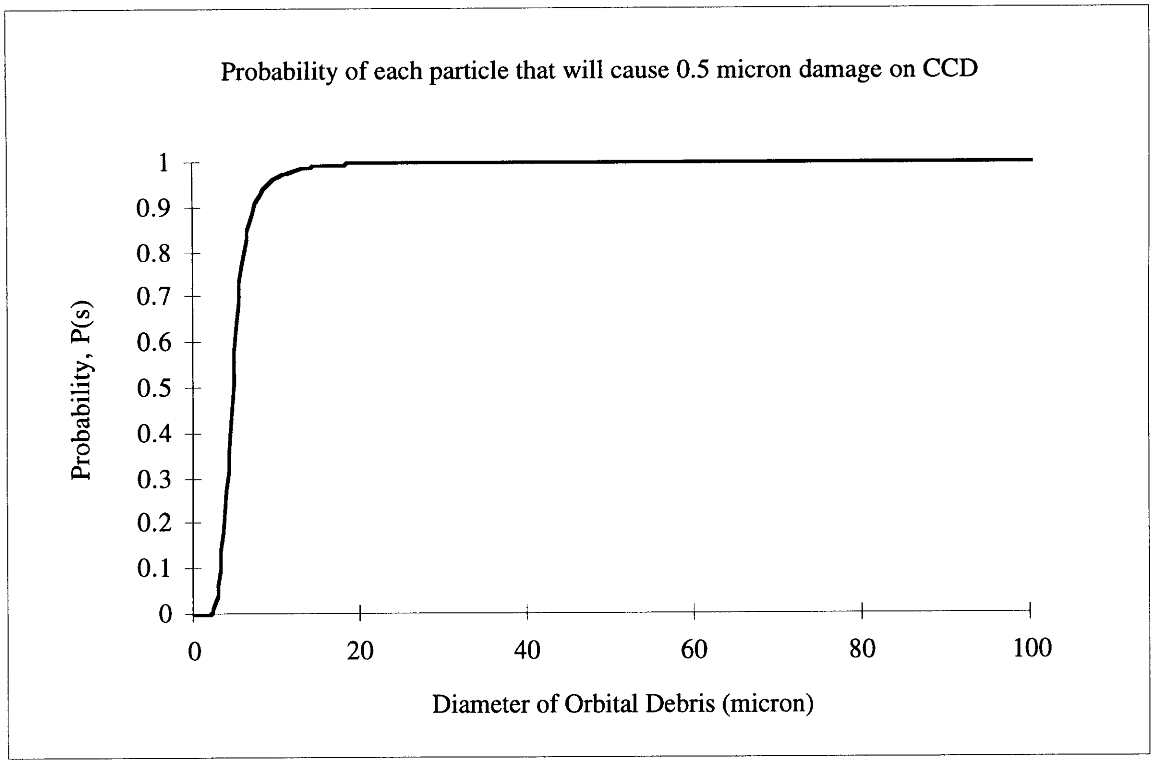

Figure 5-17. Cumulative Probability of orbital debris that will cause 0.5 micron deep or deeper damage.

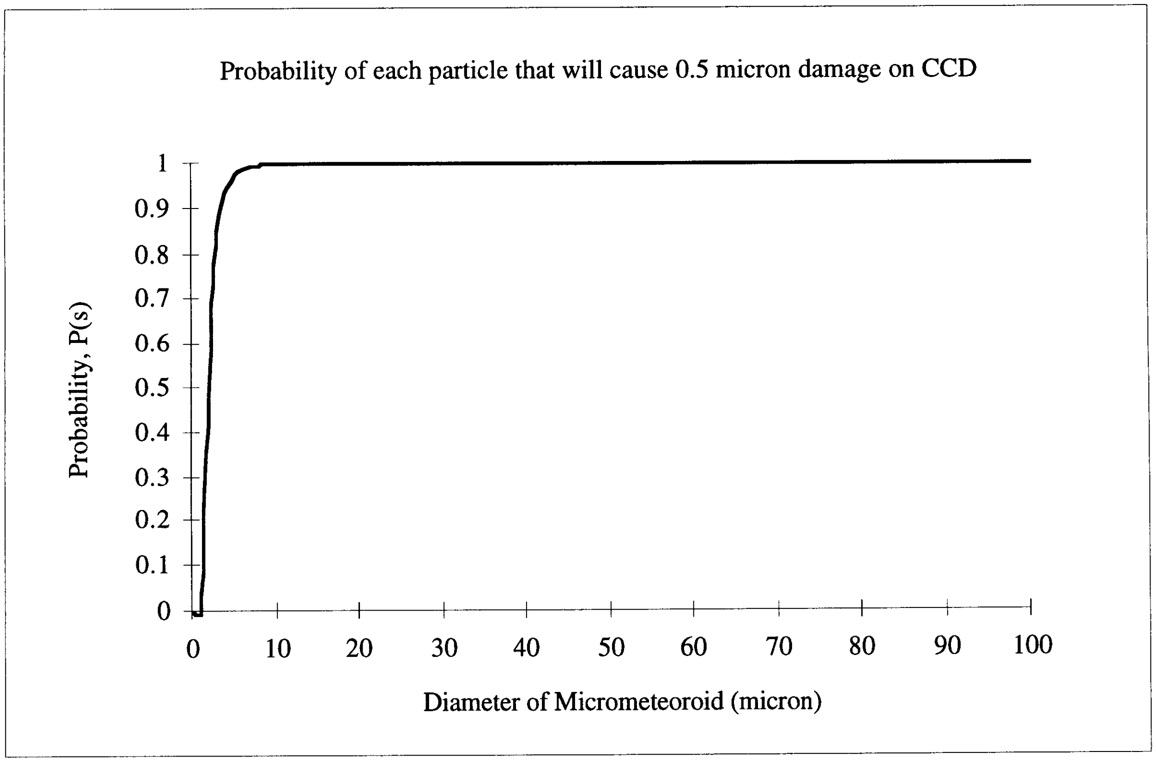

Figure 5-18. Cumulative Probability of micrometeoroid that will cause 0.5 micron deep or deeper damage.

Step 6. Impact Rate Estimation.

Using the cumulative probability of each impacting particle which will cause a crater about 0.5 micron deep or deeper on CCD and the differential flux of that particle, the impact rate for a CCD can be estimated.

$$Im\,pact\ Rate\ =\ \sum P(s)\,R(s)\,\Delta s\ =\ \int P(s)\,R(s)\,ds \qquad Equation\ 5\text{-}18$$

where

$P(s)$: *cumulative probability that an impacting particle with diameter, s, will cause 0.5 micron deep or deeper crater on a CCD.*

$R(s)$: *differential flux of the impacting particle with diameter, s.*

P(s) was calculated in Step 5. R(s) can be calculated using the cumulative flux of micrometeoroid and orbital debris. Assuming the cumulative flux has a linear relationship with the diameter of particles in log-log scale, the following equation can be used to convert the cumulative flux into differential flux:

$$Differential\ Flux,\ R(s) = \frac{dF}{ds} = m\frac{F}{s} \qquad Equation\ 5\text{-}19$$

since

$$x = log(s),\ dx = \frac{1}{s}ds$$

$$y = log(F),\ dy = \frac{1}{F}dF$$

$$m = \frac{dy}{dx}$$

F: *cumulative flux*

s: *diameter of impacting particle*

Using the above equation, the cumulative flux of micrometeoroid and orbital debris are converted into the differential flux in the following figures.

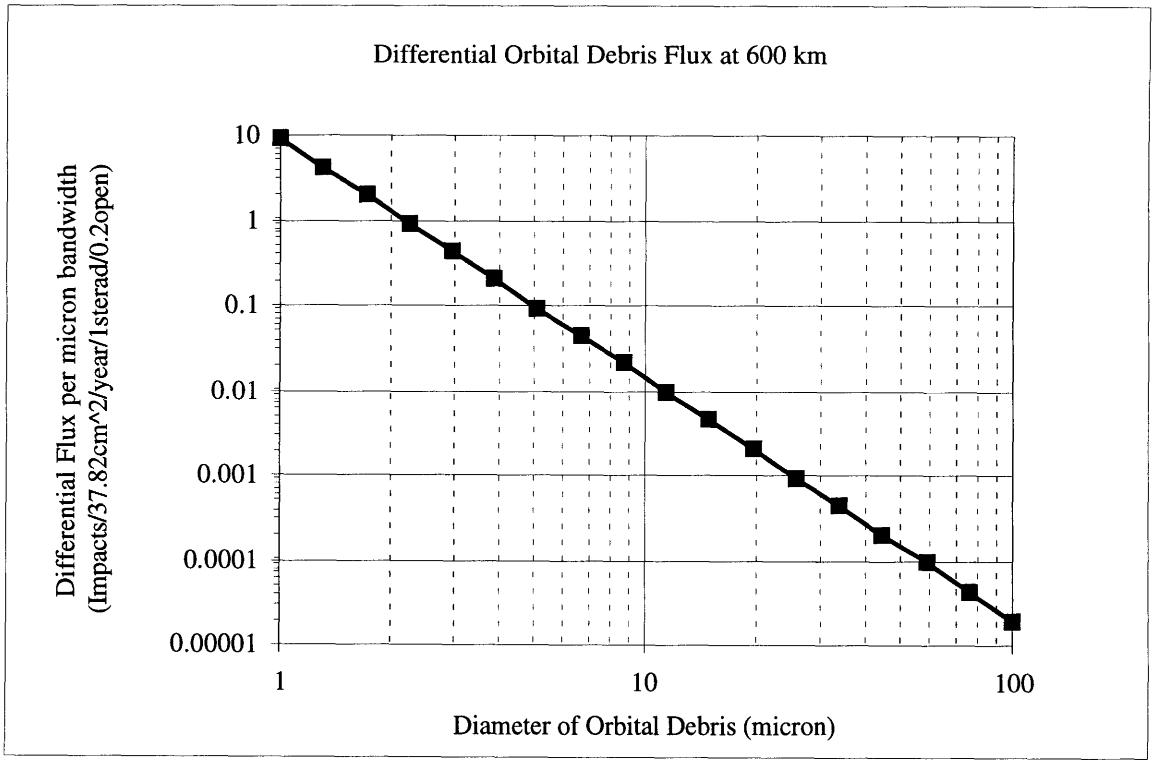

Figure 5-19. Differential Orbital Debris Flux at 600 km.

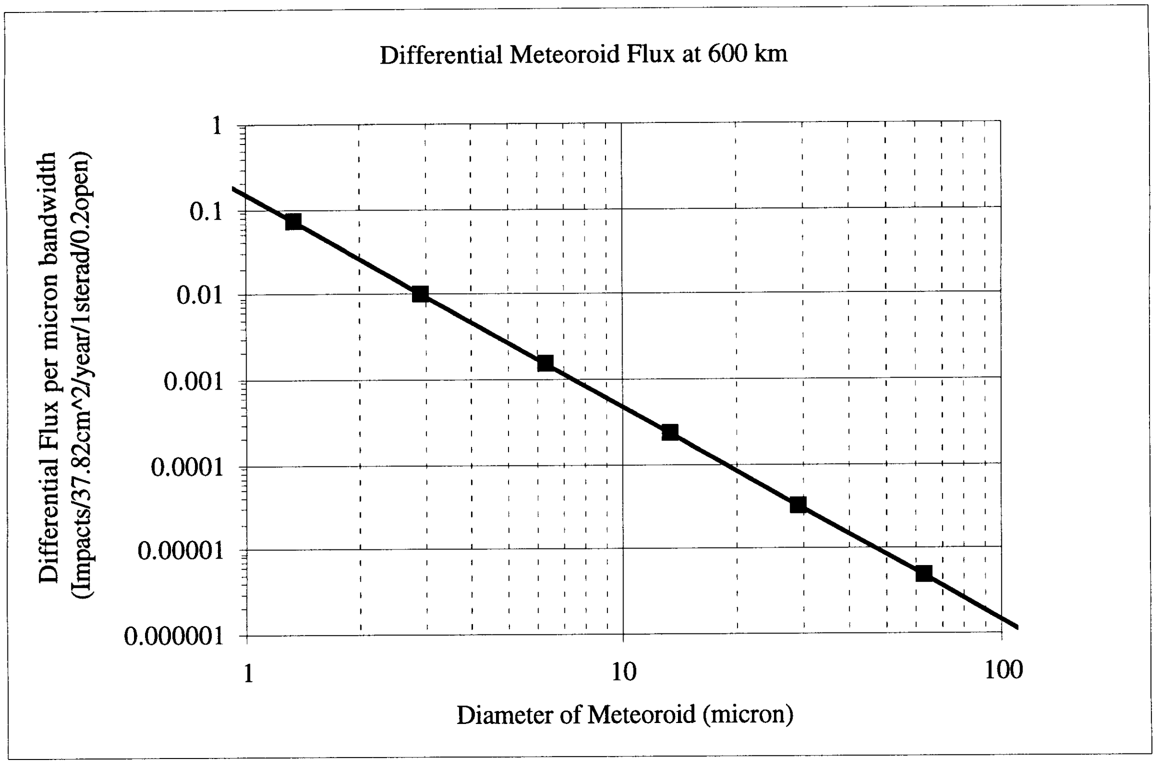

Figure 5-20. Differential Meteoroid Flux at 600 km.

Multiplying P(s) and R(s) for each impacting particle leads to the following plots.

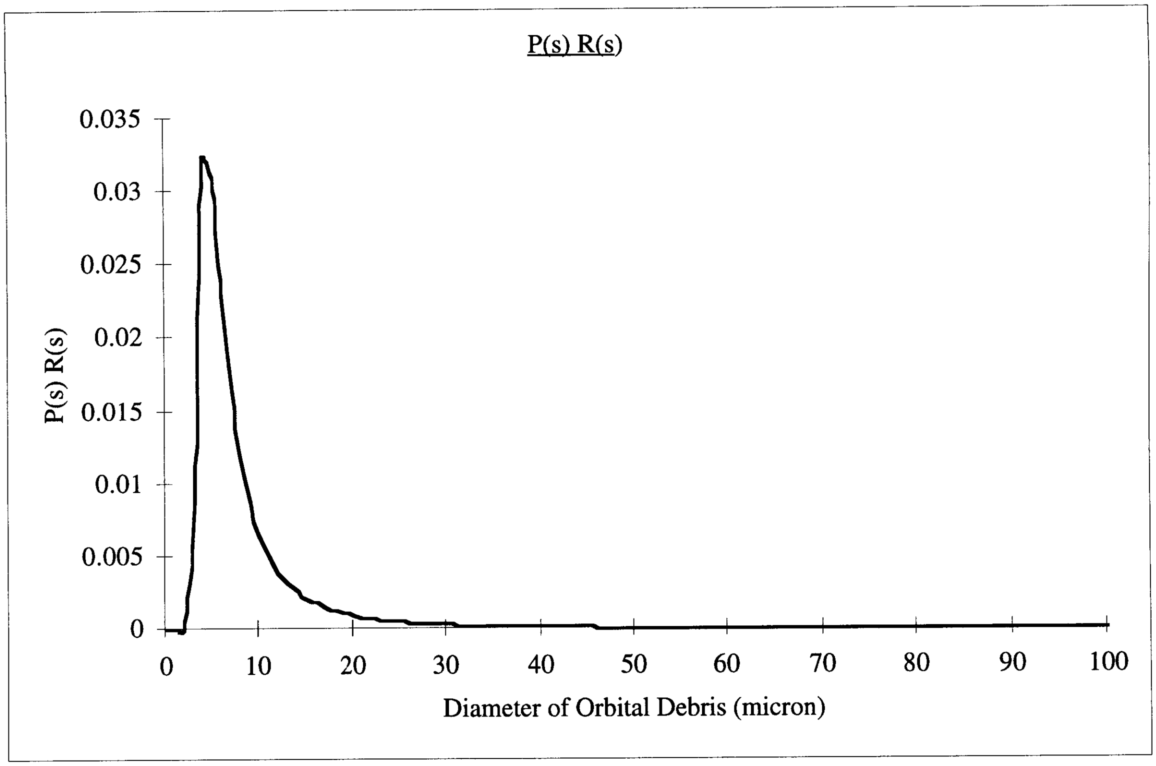

Figure 5-21. Probability, P(s) times Differential Flux, R(s) vs. Diameter of Orbital Debris.

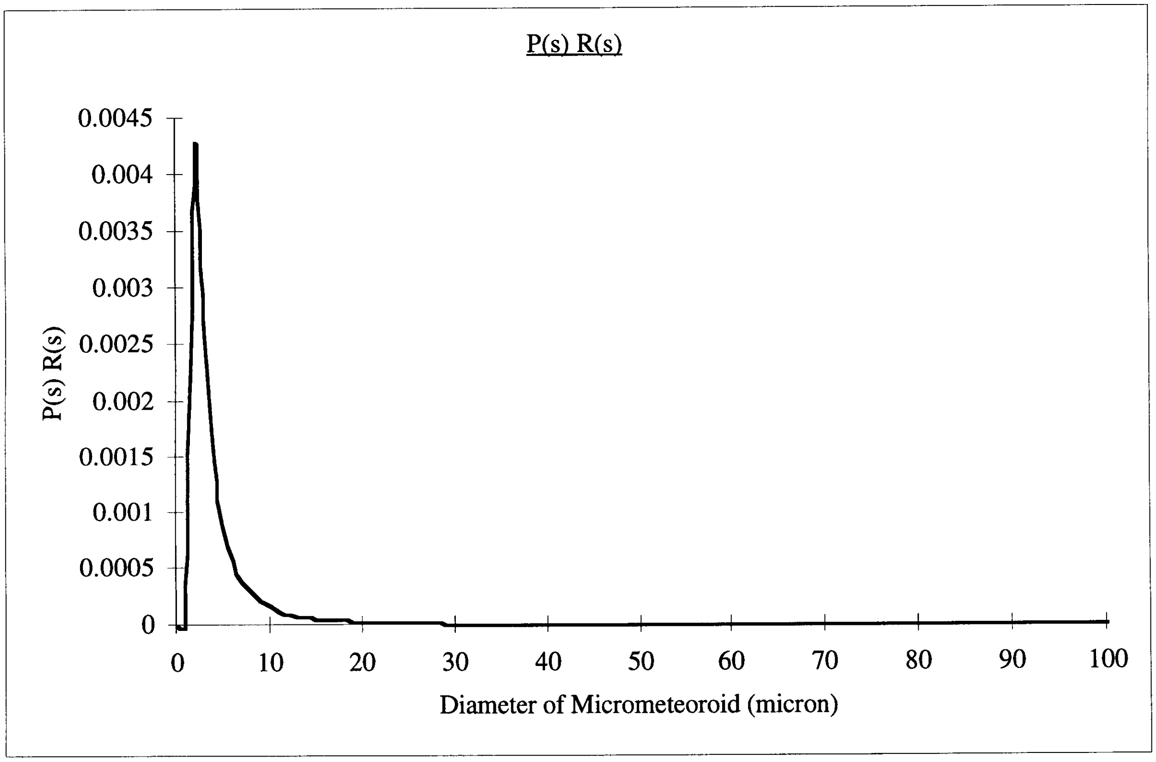

Figure 5-22. Probability, P(s) times Differential Flux, R(s) vs. Diameter of Micrometeoroid.

The impact rate on a CCD without Be shielding is the integration or the area under the curve in the above plots. The estimated impact rate on a CCD protected by only OBF but not Be shielding is shown in the following table.

	Impact Rate (impacts/year/0.2open/1sterad/1CCD)
Micrometeoroid	0.012
Orbital Debris	0.171
Total	0.183

Table 5-3. The Impact Rate Of One CCD Protected By Only OBF But Not Be Shielding.

5.2 Beryllium Shielding

As shown in the SXC diagram in Figure 1-3, a 25 μm thick Beryllium (Be) foil is added on top of only one CCD for additional protection against micrometeoroid and orbital debris impacts. The reason for adding Be shielding to only one CCD, but not on both CCDs, comes from a compromise between the quantum efficiency of the CCD and protection against micrometeoroid and orbital debris impact. Adding more material on top of the CCD means increasing protection from particle impacts. But at the same time, it will decrease its quantum efficiency because fewer photons can be transmitted through the Be shielding. The decision made by the HETE-2 science team is to add Be shielding to only one CCD to increase protection against particle impacts. By doing so, the one CCD with Be shielding will have a lower failure rate, with lower quantum efficiency. The other CCD without Be shielding will have higher quantum efficiency to detect X-rays, but will have a higher failure rate from micrometeoroid and orbital debris impact.

In the previous section, the impact rate for a CCD without Be shielding was estimated. Similarly, that for a CCD with Be shielding can be estimated. Since 0.5 micron deep crater on a CCD is relatively small compared to 25 micron deep crater on Be shielding, 25.5 micron deep crater on Be shielding will be assumed to be equal to the 25 micron deep crater on Be shielding plus 0.5 micron deep crater on a CCD. The following plots show the cumulative probability of each impacting particle that will cause 25.5 micron deep or deeper crater on Be shielding after penetrating through the OBF.

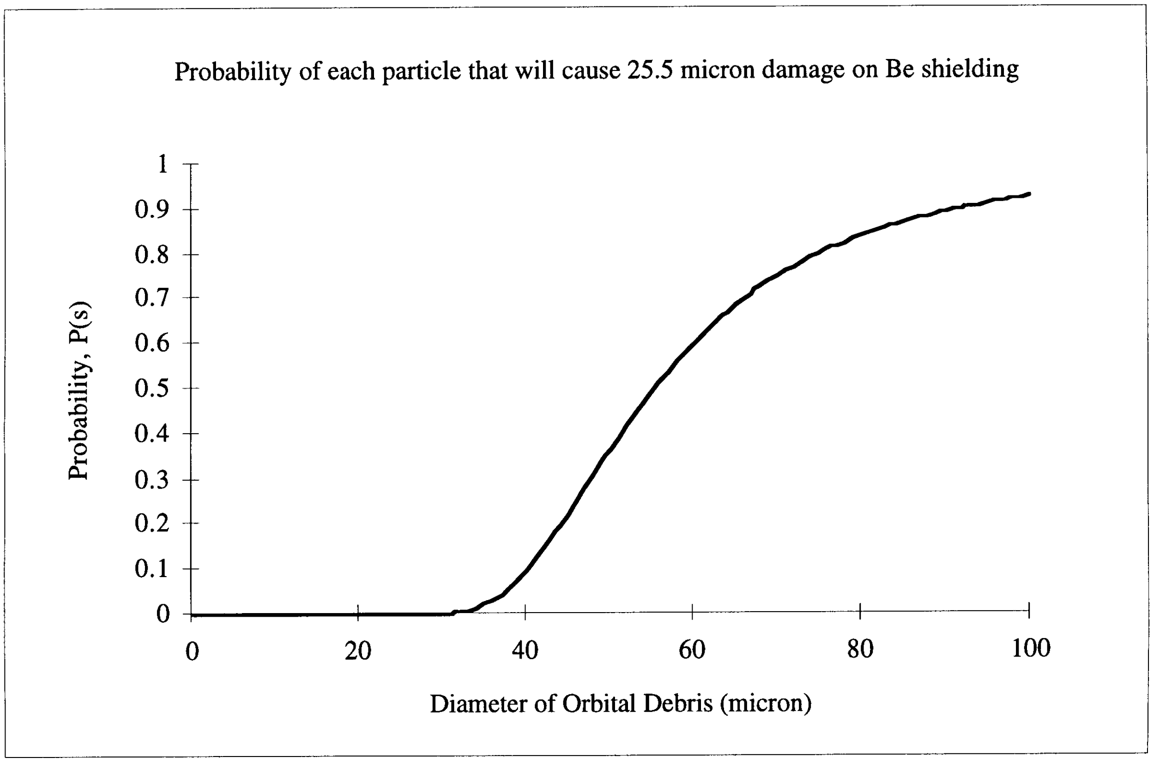

Figure 5-23. Cumulative probability of orbital debris that will cause 25.5 micron damage on Be shielding.

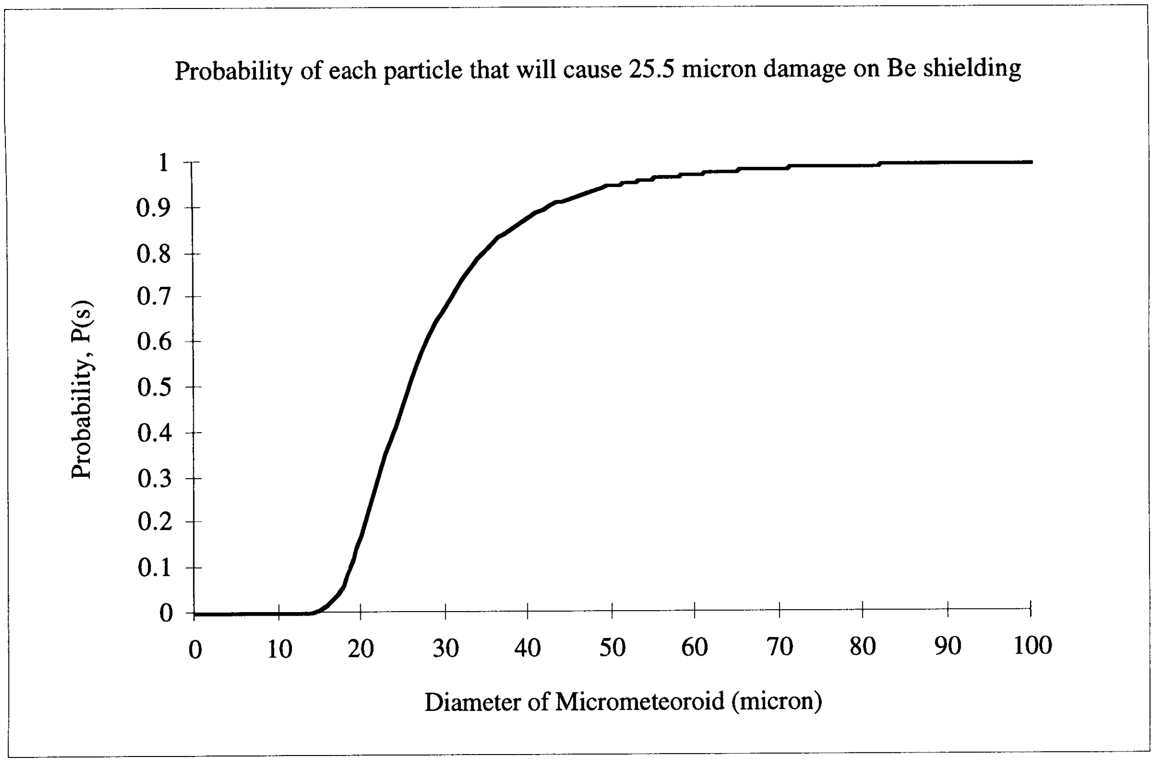

Figure 5-24. Cumulative Probability of Micrometeoroid that will cause 25.5 micron damage on Be shielding.

The above P(s) is multiplied with the differential flux, R(s), in order to estimate the impact rate on Be shielding:

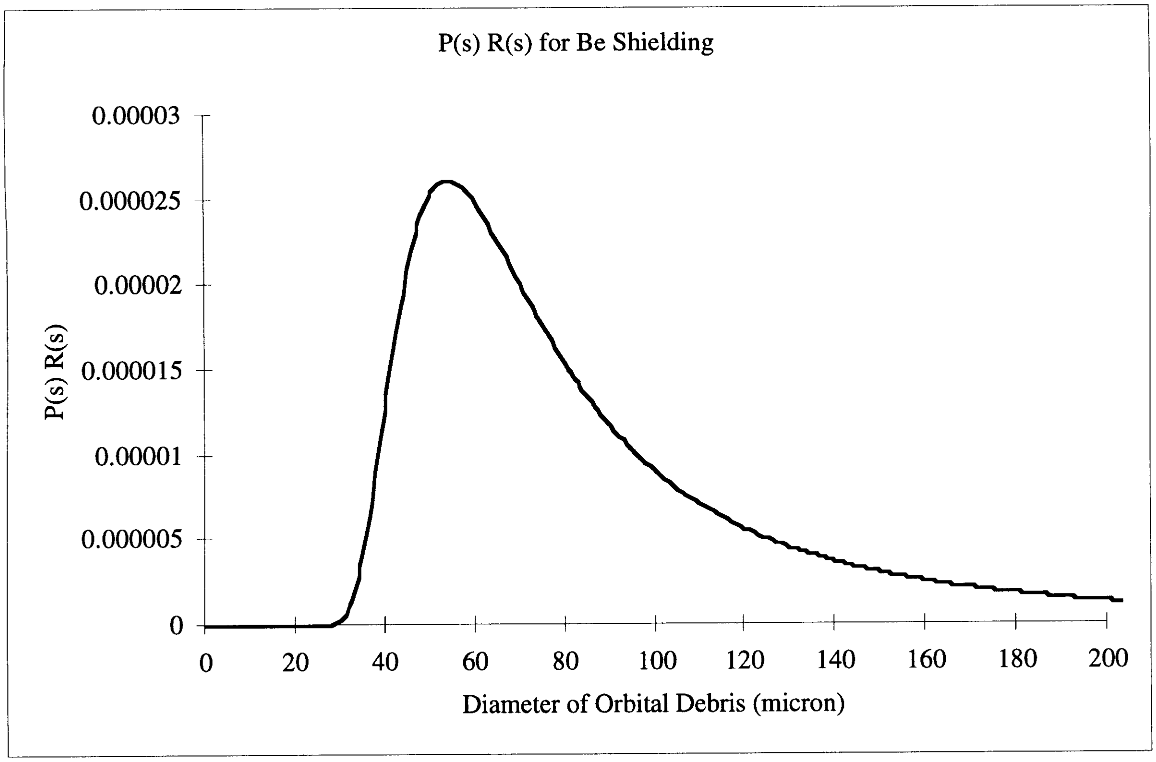

Figure 5-25. Probability, P(s) times Differential Flux, R(s) vs. Diameter of Orbital Debris.

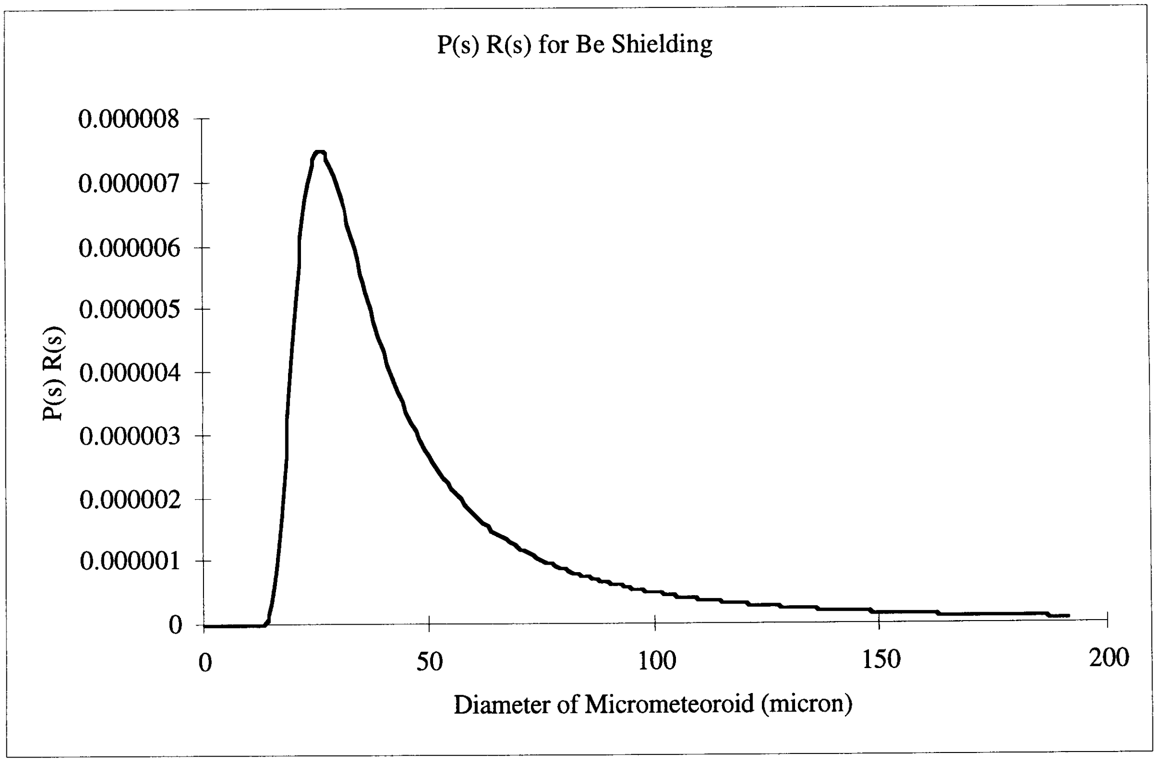

Figure 5-26. Probability, P(s) times Differential Flux, R(s) vs. Diameter of Micrometeoroid.

The impact rate on a CCD with Be shielding is the integration or the area under the curve in the above plots. The estimated impact rate on a CCD protected by both OBF and Be shielding is shown in the following table.

	Impact Rate (impacts/year/0.2open/1sterad/1CCD)
Micrometeoroid	0.00025
Orbital Debris	0.00156
Total	0.0018

Table 5-4. The Impact Rate Of One CCD Protected By Both OBF and Be Shielding.

5.3 Summary of Significant Impact Rate

A significant impact is defined by a 0.5 μm deep crater on the CCD. Although a 0.5 μm deep crater may or may not cause the entire CCD failure, it is defined as a significant impact because it has the potential to destroy the entire CCD. The significant impact rate of the CCD without Be shielding is defined by the number of impacts from micrometeoroid and orbital debris that can cause a 0.5 μm deep crater on the CCD after penetrating through the OBF. The significant rate of the CCD with Be shielding is defined by the number of impacts from micrometeoroid and orbital debris that can cause a 0.5 μm deep crater on the CCD after penetrating through both OBF and Be shielding. Since the significant impact rate of CCDs with and without Be shielding will be different, it was estimated separately for each CCD with Be shielding and without Be shielding. The significant impact rate estimation for each CCD is summarized in the following tables.

	Significant Impact Rate (impacts/year/0.2open/1sterad/1CCD)
CCD without BE shielding	**0.183**
CCD with BE shielding	**0.0018**

Table 5-4. The Significant Impact Rate Of One CCD.

In conclusion, the significant impact rate for one CCD protected by only OBF but not Be shielding is 0.183 times per year. For the other CCD protected by both OBF and Be shielding, the significant impact rate is 0.0018 times per year.

Chapter 6

LEONID METEOROID STORM

The comparison of micrometeoroid and orbital debris fluxes in Figure 3-2 showed that orbital debris comprises the major fraction of micron sized particles in low earth orbit. For example, the cumulative flux of orbital debris with size of 1 micron or larger is about 50 times greater than the flux of micrometeoroids with the same size. The previous section 5.3 also showed that the significant impact rate for a CCD due to orbital debris impacts is higher than the significant impact rate due to the micrometeoroid impacts. A single CCD without Be shielding will have an estimated significant impact rate of 0.012 times per year from micrometeoroid impacts and 0.171 times per year from orbital debris impacts. A single CCD with Be shielding will have a significant impact rate of 0.00025 times per year from micrometeoroid impacts and 0.00156 times per year from orbital debris. These impact rate estimations lead to the conclusion that the orbital debris environment is more hazardous than the micrometeoroid environment to the HETE-2 SXC in low earth orbit. But unlike the orbital debris environment, which is expected to have a constantly increasing rate due to man's space activity, the meteoroid environment can change dramatically during a meteoroid storm. One such threat that threatens the SXC is the Leonid meteoroid storm. This chapter will explain the influence of this storm on the HETE-2 SXC.

6.1 Background

The comet Tempel-Tuttle is about 4 km in diameter and orbits the Sun with a period of 33 years. On February 28, 1998, comet Tempel-Tuttle passed perihelion, the closest point to the Sun. When the comet approaches the Sun, it begins to heat up, its ice surface evaporates, and dust particles are ejected into orbit. These solid materials follow roughly the same path as the comet. Meteor showers are the result of the encounter of the Earth with the debris left behind by comets. Every year the Earth experiences about a dozen major meteor showers. For example, every August the Earth experiences the Perseids meteor shower, every December the Earth experiences the Geminids meteor shower, and every November the Earth passes through the debris trail left behind by the comet Tempel-Tuttle [Beech et al., 1995]. Since the debris appears to be coming from the direction of the constellation Leo, this November meteor shower is called the Leonid shower.

For roughly 107 days of the year, we see shower activity at a rate of 30 meteors per hour. The remaining 258 days, we see a sporadic rate of 8 meteors per hour. Therefore the average annual meteor rate is about 15 meteors per hour. These hourly rates are the actual rate of infalling meteors. In November of 1998 and 1999, because of recent passage of the comet Tempel-Tuttle, the Earth is expected to encounter an increase in the amount of meteoroids. The Earth is expected to experience what is called a meteor storm, as opposed to a meteor shower. When the meteor rate reaches more than 1000 meteors per hour, it is defined as a 'storm'. The scientists predict we will see about 200 to 5000 meteors per hour and possibly more during the Leonid storm. Historically, the Earth experiences the most intense meteor activity in November of the year following the comet passage of perihelion, rather than in the same year. For example, following perihelion of Tempel-Tuttle in 1965, the Earth experienced a major Leonid meteor storm in November of 1966. This was the most intense meteor storm on record, in which the peak meteor rate reached about 150,000 per hour [Cooke, 1996]! This is a dramatic increase compared to 15 per hour during normal times. Therefore, while we expected a storm to occur in November of 1998, there is historical precedent for a storm to also occur in November of 1999. The encounter with the debris trail from Tempel-Tuttle will last several days, but the most intense part of the encounter typically lasts only 2 to 3 hours. This meteoroid storm will be the largest such threat ever experienced by orbiting satellites.

6.2 Characteristics of Leonid Meteoroids

6.2.1 Size

According to D. K. Lynch, R.W. Russell, and M.Sitko at the Leonid Meteoroid Storm and Satellite Threat Conference in Manhattan Beach (April 27-28, 1998), the dust particles ejected by comet Tempel-Tuttle are of relatively large size. They measured the mid-Infrared spectra of the cometary dust using the Broadband Array Spectrograph System on the NASA 3-meter Infrared Telescope Facility (IRTF). They found a smooth infrared spectrum between 3 and 13.5 micron, with no sign of the Si-O stretch vibration band at 10 micron. The authors concluded that the particles had to be bigger than 30 micron to not show such features at the time of the observations on February 8 and 9, 1998 [Jenniskens, 1998]. Although Lynch et all suggest a size distribution favoring larger particles, other findings suggest that the size distribution of Leonid particle is close to the distribution of meteoroid during normal time. For example, radar observations of the 1966 Leonid storm by McIntosh and Millman indicate that the size distribution of meteoroids during the Leonid storm is close to the distribution of meteoroids during normal times [McIntosh and Millman, 1970]. Since our knowledge of the minimum size of Leonid particle is inconclusive and this size varies from year to year, the size distribution of the Leonid meteoroids will be assumed to be the same as that of meteoroids during normal times.

6.2.2 Composition

According to the Aerospace Corporation, the major composition of Leonid meteoroid is silicate and carbonaceous grains [Ailor et al., 1998].

6.2.3 Velocity

Leonid meteoroids are very fast, with average velocity of 70 km/s. Therefore, the spacecraft can be struck on the trailing edges. The reason for this high velocity is that meteoroids from Comet Tempel-Tuttle move in a retrograde orbit about the Sun, so the Earth collides with them almost "head on" as shown in the following figure. With these velocities, even a grain of sand with the size of the head of a pin has the same energy as a .22 caliber bullet.

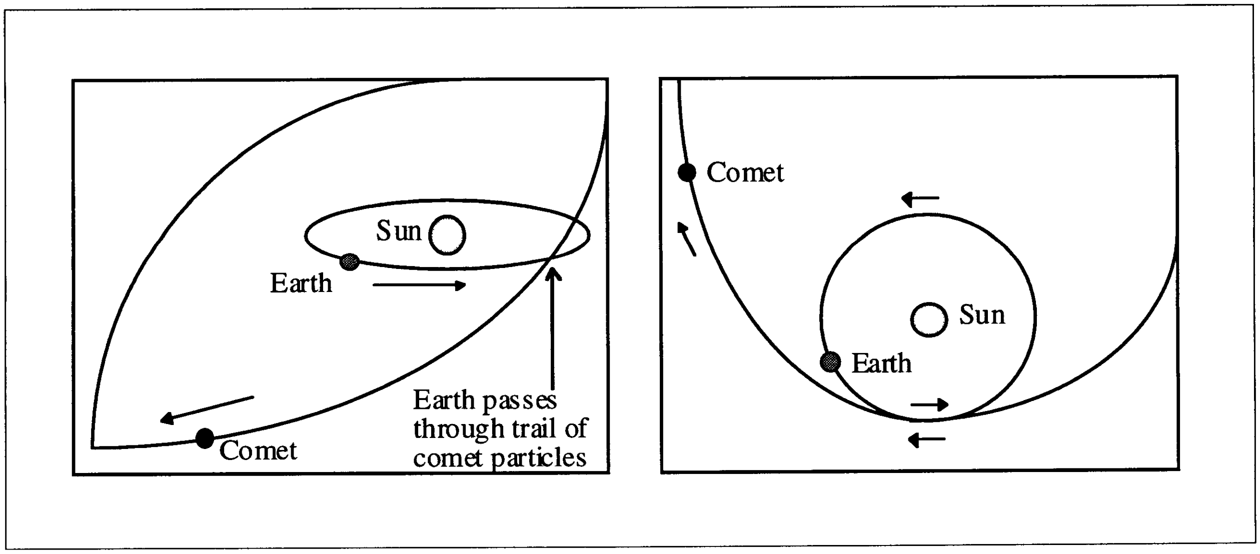

Figure 6-1. The Direction of the Comet Tempel-Tuttle's Orbit.

6.3 Probability of Storm Occurring

William Cooke calculated the probability of a Leonid storm occurring from the year 1998 to 2000 using the limited historical data collected by Mason and Yeomans. The calculated probability of a Leonid storm occurring is shown in the following table [Cooke, 1996].

Year	Probability of Storm
1998	0.78
1999	1.00
2000	0.33

Table 6-1. Probability of Storm Occurring.

Since the storm is defined by a meteor rate of greater than 1000 meteors per hour, the above probability of storm is the probability that the meteor rate will reach 1000 per hour. The numbers in the above table indicate that there is about 0.78 probability of storm occurring in 1998, almost certain chance of a storm in 1999, and a reduced chance of a storm in 2000. The launch date for HETE-2 has been scheduled for January 23, 2000. Therefore, HETE-2 will not experience the November 1999 storm. Although the probability of a storm occurring in November of 2000 is only 0.33, it is important to find out if the SXC will get hit during this storm if it really occurs.

6.4 Flux Estimation of a Leonid Storm

According to W. Cooke, the encounter circumstances for the upcoming 1998-2000 time period are predicted to be very similar to those of 1865-1866. Based on the records of that time, we may expect meteor rates of about 1000 per hour for the November of 1998 and 2000. The predicted rate for November 1999 is about 5000 meteors per hour. The worst case scenario is to assume a rate equal to the 1966 storm, about 150000 meteors per hour. In order to convert meteor rate into meteoroid flux, the normal meteoroid flux is multiplied by the ratio of predicted meteor rate to normal meteor rate [Cooke, 1996]. The average meteor rate is about 15 meteors per hour during normal times.

For example,

Predicted 1998 and 2000 Leonid meteoroid flux

= normal meteoroid flux * (predicted meteor rate / normal meteor rate)

= normal meteoroid flux * (1000 / 15)

Predicted 1999 Leonid meteoroid flux

= normal meteoroid flux * (5000 / 15)

Predicted worst case Leonid meteoroid flux

= normal meteoroid flux * (150000 / 15)

The actual meteor rate for November 1998 Leonid storm was less than predicted. According to the International Meteor Organization, this year's Leonid storm peaked at a rate of 500 per hour, instead of predicted rate of 1000 per hour [Chang, 1998].

Actual 1998 meteoroid flux

= normal meteoroid flux * (500 / 15)

Using the above relationships and the normal meteoroid flux plot in Figure 2-2, the Leonid meteoroid flux is plotted in the following figure:

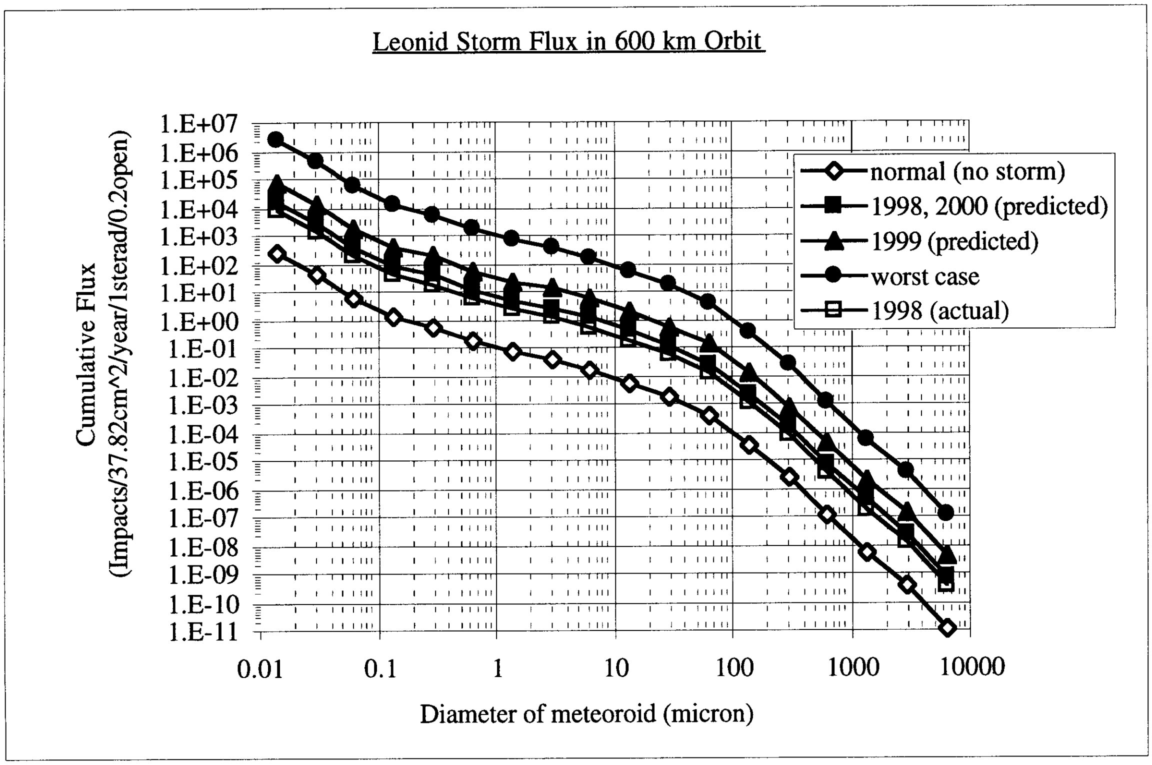

Figure 6-2. Leonid Meteoroid Storm Flux in 600 km Orbit.

The above Leonid meteoroid storm flux assumes that the size distribution of Leonid meteoroids is the same as the distribution of meteoroids during normal times.

6.5 Impact Rate Estimation during Leonid Meteoroid Storm

In Section 5.3, the significant impact rate for a CCD due to the impacts from micrometeoroid was estimated for the non-storm or the normal time. This estimate is summarized in the following table.

	Significant impact rate of one CCD from micrometeoroid impact during normal time (Impacts/year/0.2open/1sterad/1CCD)
CCD without BE shielding	0.012
CCD with BE shielding	0.00025

Table 6-2. Failure Rate of CCD From Micrometeoroid Impact During Normal Time

Using the above significant impact rate for a CCD due to the micrometeoroid impacts during the normal time, the impact rate during the Leonid meteoroid storm can be calculated. The impact rate of the CCD during the Leonid storm will be increased by the ratio of predicted meteor rate over the normal meteor rate. The impact rate during the storm, however, has to account for the duration of the storm, instead of an entire year. Although the storm increases the meteoroid flux significantly, the peak time of the storm lasts only several hours. According to the Aerospace Corporation, the duration of a Leonid meteoroid storm is about 1-2 hours. Therefore, the following equations calculate the impact rate of the CCD during the storm assuming the storm duration is 2 hours.

$$\begin{aligned}&\textit{Impact Rate of One CCD during 2 Hour Storm in Nov 2000}\\&= \textit{Normal Impact Rate per Year} \times \frac{\textit{1000 (Predicted meteor rate)}}{\textit{15 (Normal meteor rate)}} \times \frac{\text{1 year}}{\textit{8760 hr}} \times 2hr\end{aligned}$$

$$\begin{aligned}&\textit{Impact Rate of One CCD during 2 Hour Storm (worst case scenario as in 1966)}\\&= \textit{Normal Impact Rate per Year} \times \frac{\textit{150000 (worst case meteor rate)}}{\textit{15 (Normal meteor rate)}} \times \frac{\text{1 year}}{\textit{8760 hr}} \times 2hr\end{aligned}$$

The results from above equation are summarized in following table.

	Impact rate of one CCD during 2 hr Leonid meteoroid storm in Nov. 2000. (Impacts/0.2open/1sterad/ 1CCD/2hrs)	Impact rate of one CCD during 2 hr Leonid meteoroid storm for worst case scenario. (Impacts/0.2open/1sterad/ 1CCD/2hrs)
CCD without BE shielding	0.000183	0.0274
CCD with BE shielding	0.0000038	0.00057

Table 6-3. Impact Rate of CCD during 2 hour Leonid Storm.

The above table shows that there is a very small chance that the CCD will get hit even if the Leonid storm occurs in November 2000. The chance of a Leonid storm occurring in November 2000 is only about 0.33 as discussed in section 6.3. The above results indicate that although the Leonid storm increases the flux of micrometeoroids significantly, about 67 times the normal flux in November 2000 and 10000 times for the worst case scenario, the impact rate on the CCD during a storm is small, because this dramatic increase in micrometeoroid flux lasts only a few hours.

References

1. Ailor, W., Lynch, D., and Tagliaferri, E. 1998. "The Upcoming Leonid Meteoroid Storm and Its Effect on Satellites." http://www.aero.org/leonid.

2. Anderson, B. J. and Smith, R. E. 1994. "Natural Orbital Environment Guidelines for Use in Aerospace Vehicle Development." NASA TM 4527.

3. Beech, M., Brown, P. and Jones, J. 1995. "The Potential Danger to Space Platforms from Meteor Storm Activity." Q.J.R.astr.Soc., Vol. 36. pp. 127-152.

4. Berthoud, L., and Mandeville, J.C. 1997. "Low-Earth-Orbit Micrometeoroid and Debris Investigations", Int. J. Impact Engng, Vol. 34 No.1, pp. 125-132.

5. Chang, K. 1998. "Leonids Dazzled a Little", http://.abcnews.com/sections/DailyNews/leonids981124.html.

6. Christiansen, E. L. 1993. "Design and Performance Equations for Advanced Meteoroid and Debris Shields", International Journal of Impact Engineering, Vol. 14. pp.145-156.

7. Cooke, W. 1996, "Estimation of Meteoroid Flux for the Upcoming Leonid Storms." http://see.msfc.nasa.gov/see/mod/leonids.html

8. Cour-Palais, B.G. 1987. "Hypervelocity Impacts in Metals, Glass and Composites." International Journal of Impact Engineering, Vol 5. pp.681-692.

9. Fechtig, H., Grun, E., and Morfill, G. 1979. "Micrometeoroids within Ten Earth Radii", Planet. Space. Sci. Vol. 27, pp. 511-531.

10. Frost, V.C. 1970. "Meteoroid Damage Assessment." NASA SP-8042.

11. Gehring, J. W. 1970. "High-Velocity Impact Phenomena" Academic Press, New York. Chap. IV, pp. 113-117, pp. 133-147, and Chap. IX, p. 493.

12. Grady, D.E. and Kipp, M.E. 1985. "Geometric Statistics and Dynamic Fragmentation." J. Appl. Phys., Vol 58. pp. 1210-1222.

13. Grun, E. and Pailer, N. 1979. "The Penetration Limit of Thin Films." Planet. Space Sci., Vol. 28. pp. 321-331.

14. Hodgson, E.W., Cupples, S. 1992. "Micrometeoroid and Orbital Debris Hazard Considerations for Space Station-Related EVA." pp. 1373-1389.

15. Jenniskens, P.1998. "Comet 55P/Tempel-Tuttle News." http://www-space.arc.nasa.gov/~leonid/cometnews.html.

16. Jones, R. D. 1998. "Space Debris", http://www.xdiv.lanl.gov/XCM//neural/xwindows/space_debris.html

17. Kessler, D. 1988. "Orbital Debris Environment for Spacecraft Designed to Operate in Low Earth Orbit." NASA-TM-100471.

18. Kessler, D.J., Zhang, J., Matney, M.J., Eichler, P., Reynolds, R.C., Anz-Meador, P.D., and Stansbery, E.G. 1996. "A Computer-Based Orbital Debris Environment Model for Spacecraft Design and Observation in Low Earth Orbit." NASA-TM 104825.

19. Kipp, M.E., Grady, D.E., and Swegle, J. W. 1993. "Experimental and Numerical Studies of High-Velocity Impact Fragmentation." SAND93-0773.

20. Lawrence, R.J. 1987. "A Simple Model for the Optimization of stand-off Hypervelocity Particle Shields." Int. J. Impact Engng, Vol. 5. pp.451-461.

21. McIntosh, B. and Millman, P. 1970. Meteoritics, 5, 1. pp. 1-18

22. Nagel, K., Neukum, G., Fechtig, H., and Gentner, W. 1976. "Density and Composition of Interplanetary Dust Particles." Earth and Planetary Science Letters, Vol. 30, pp. 234-240.

23. Ricker, G. 1999. "Appendix MO-1. Program-Level Requirements for the HETE-2 Project." HETE-2 documents. pp. 1-7.

24. Ricker, G. 1997. "Re-flight of the International High Energy Transient Experiment (HETE): Motivation and Prospects." HETE-2 Position Paper. pp. 1-27.

25. Smith, D. and Adams, N. G. 1974. "Flux and Composition of Micrometeoroids in the Diameter Range 1-10 mm.", Nature. Vol.252, pp. 101-106.

26. Vanderspek, R. and Villasenor, J. 1997. "HETE SXC System Requirements." HETE-2 documents. pp.1-16.

27. Walsh, J.M., Stradling, G.L., and Idzorek, G.C. 1993. "Microparticle Impacts at Ultra-high Velocities: Their Relation to Macroparticle Impacts.", Int. J. Impact Engng. Vol. 14, pp.775-784.

28. Wertz, J.R., and Larson, W.J. 1992. Space Mission Analysis and Design, 2nd ed. Microcosm Inc. pp. 757-766.